공학박사 학위논문

# Studies on Oxophilic Effect in Platinum Nanocatalysts for Aqueous Electrocatalysis

수계 전기촉매 반응을 위한 백금 나노촉매의 호산소 효과 연구

2017년 8월

서울대학교 대학원

화학생물공학부

이 명 재

# Studies on Oxophilic Effect in Platinum Nanocatalysts for Aqueous Electrocatalysis

## 수계 전기촉매 반응을 위한 백금 나노촉매의 호산소 효과 연구


지도교수 성 영 은

이 논문을 공학박사학위논문으로 제출함

2017년 7월

서울대학교 대학원

화학생물공학부

이 명 재


이명재의 박사학위논문을 인준함

2017년 7월

위 원 장 현택환 (인)

부 위 원 장 성영은 (인)

위 원 김대형 (인)

위 원 최희만 (인)

위 원 유성종 (인)

# Abstract

# Studies on Oxophilic Effect in Platinum Nanocatalysts for Aqueous Electrocatalysis

Myeong Jae Lee

School of Chemical and Biological Engineering

The Graduate School

Seoul National University

Aqueous electrocatalysis occurs in electrochemical cells that generally comprise electrolyte, an external circuit, electrocatalytic anode and cathode. There are two types of the cells according to the electric flow; (i) polymer electrolyte membrane fuel cell for converting chemical energy to electric energy with spontaneous redox reaction and (ii) water electrolyzer for converting electric energy to chemical energy for fuel production. Hydrogen oxidation/evolution, oxygen reduction/evolution, and carbon monoxide oxidation in acidic and basic media are the most important reactions in the two types of electrochemical cell. In this thesis, the role of platinum nanocatalyst, metal (oxy)hydroxide and metal oxide (hydrate) for those electrocatalytic reactions were investigated.

The main issues in the development of catalysts for polymer electrolyte membrane fuel cell, which are mainly platinum-alloy catalysts, are improvements of activity and low usage of the precious metal. In addition, developments of non-platinum catalysts and enhanced activities of platinum-based catalysts have been the main objective of the research works on electrocatalysts for water electrolyzer.

Therefore, in this study, state-of-the-art platinum nanocatalysts blended with metal oxide (hydrate) or metal (oxy)hydroxide inducing oxophilic effect for more enhanced activities of carbon monoxide oxidation and hydrogen evolution, and the metal oxide (hydrate) or the metal (oxy)hydroxide for enhanced oxygen evolution were utilized as electrodes. From keen electrochemical and physicochemical observations of the blended catalysts systems, it was confirmed that oxophilic effect without electronic change of platinum surface had a crucial effect on the electrochemical reactions in acidic and basic media. In addition, it was observed that interaction between aqueous electrolytes and the catalytic system facilitated oxophilic effect, and this work could bring the better understanding of oxophilic tuning which generally arises in the platinum-alloy system.

In chapter 1, bases to electrocatalysis, polymer electrolyte membrane fuel cell, and water electrolysis cell were introduced. After a brief introduction of kinetics in electrocatalysis and two-types of electrochemical cells according to directions of electric flow, electrochemical reactions in polymer electrolyte membrane fuel cell, fundamentals of platinum alloy catalysts, and previously reported researches of oxophilic effect were introduced. In last, electrocatalysis in water electrolysis cells and possible improvements by oxophilic effect in hydrogen evolution were briefly discussed.

In chapter 2, an extended concept of oxophilic effect between platinum nanocatalysts and hydrous ruthenium oxide in acidic media was discussed. The simple model system with blended catalyst was introduced in order to investigate the electrocatalytic carbon monoxide oxidation mechanisms and oxophilic effects in negligible direct-junctions between platinum nanocatalysts and hydrous ruthenium oxide. From this approach, it could be observed the sole oxophilic effect in the electrochemical environment by the unmodified crystallinity and electronic structure of Pt nanoparticles. In addition, significantly enhanced carbon monoxide oxidation was observed in electrochemical measurements and facilitated carbon

monoxide oxidation of the blended system in real fuel cell operation conditions was confirmed by single cell experiments.

In chapter 3, based on feasibility of the blended system, using thermal annealing at various temperatures, ruthenium and iridium oxide (hydrate) catalysts with different oxygen evolution activities in acid electrolyte were obtained. By physicochemical comparisons between the hydrous oxide catalysts, it was verified that there was a new descriptor for oxygen evolution activity in acid. In addition, blended catalysts were prepared by uniformly blending carbon-supported platinum with oxide hydrate catalysts which had different activities in acidic oxygen evolution. Based on the carbon monoxide oxidation in this set of blended catalysts, a linear correlation between oxygen evolution activity of hydrous oxide catalysts and carbon monoxide oxidation performance in blended catalysts was verified in acidic electrolyte. From these observations, long-range water activation by exchanges between O-H and hydrogen bond in chains of water molecule was suggested.

In chapter 4, further studies on oxophilic effect in alkaline media were carried out. From electrochemical observations on carbon monoxide oxidation, oxygen evolution, and hydrogen evolution and physicochemical characterizations, long-range oxophilic interactions between Pt nanoparticles and various water dissociation catalysts through electrolyte were verified in the blended catalysts system. Furthermore, in-depth discussion on the effect of metal-oxygen interaction on oxophilic effects was also performed.

***Keywords:*** electrocatalysis, polymer electrolyte membrane fuel cell, water electrolysis, oxophilic effect

***Student number:*** 2011-22925

# Contents

# List of Tables

# List of Figures

# Chapter 1. Introduction

## 1.1. General introduction to electrocatalysis

Electrochemical reaction is one of the chemical reactions that cause electrons to move through the system. The movement of the electron is called electricity, which can be generated by electron transfer from one element to another in oxidation-reduction (redox) reaction. Electron transfer between electrode and reactant can be occurred by tunnelling. Since tunneling only occurs between reactant and electrode which are very close, electrochemistry has some distinguished points different from other chemistries. Figure 1.1 shows oxidation reaction and reduction reaction of reactants on an electrode. In general, an electrochemical cell is composed of electrodes (anode and cathode), electrolyte and external circuit. In this system, moved electrons can be measured and thus, electrochemical reactions can be analyzed by observing the electrons. The net flow of electrons (current) can be expressed as the sum of the reaction rates of the anode and the cathode. Kinetics of electrochemical reaction and the current are correlated by the equation as below;

$$i_{net} = i_0[(C_O(0,t)/C_O^*)e^{-\alpha F\eta/RT} - (C_R(0,t)/C_R^*)e^{(1-\alpha)F\eta/RT}]$$

where, $i_0$, $\alpha$, $\eta$, $C_O$, $C_O^*$, $C_R$, $C_R^*$ and f are exchange current, symmetric factor, over potential (applied potential subtracted by equilibrium potential), concentration and bulk concentration of oxidant and reductant, respectively. If an effect of mass transfer is very low and $i_0$ is large enough, it has small activation overpotential as shown in Figure 1.2. In the electrocatalysis, since $i_0$ is determined by an activity of a catalyst, there have been many efforts to research on the more desirable catalyst

which can bring faster kinetic of the reaction. Figure 1.3 simply shows reaction kinetics in an electrocatalytic system by catalytic effect and electric potential. Electrocatalysis has an important effect on next-two types of electrochemical cell which are a galvanic cell and an electrolytic cell. A galvanic cell is an electrochemical cell that produces electricity from spontaneous redox reactions. A typical example of the galvanic cell is a fuel cell. As one of the kinds of the fuel cell, polymer electrolyte membrane fuel cell shows high energy conversion efficiency and has been applied to a portable device, automobiles, and residential power generation. In the cell, measured potential can be stated as;

$$E = E° - \eta_{cathode} - \eta_{anode} - iR_{ohm}$$

this equation indicates that overall cell-efficiency is depended on overpotential of cathode and anode. In the polymer electrolyte membrane fuel cell, which uses polymer-type electrolytes, platinum (Pt) and Pt-based alloy catalysts have been widely used in order to reduce overpotential of the electrodes. As another type of electrochemical cell, an electrolytic cell undergoes a redox reaction when electricity is applied by an external bias (electrolysis). An important example of electrolysis is splitting of water into hydrogen and oxygen and the reaction occurs in the system comprising cathode, anode, electrolyte (water solvent) and the external circuit. Applied potential of the cell can be stated as;

$$E = E° + \eta_{cathode} + \eta_{anode} + iR_{ohm}$$

these overpotentials also have to be reduced in order to minimize applied potential and enhance overall performance. In the electrochemical water splitting, iridium oxide is widely used as an anode material due to its high activity and stability.

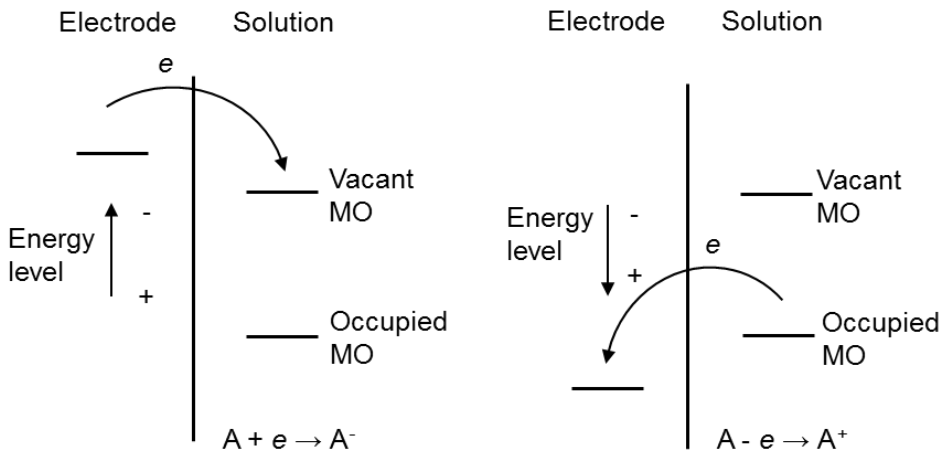


**Figure 1.1.** Oxidation and reduction reactions on electrode surface.

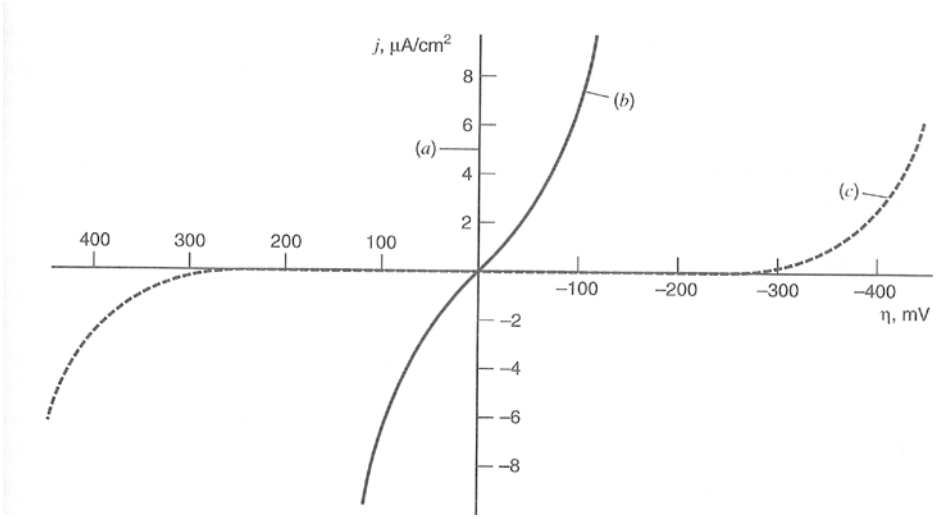


**Figure 1.2.** Effect of exchange current density on the activation overpotential required to deliver net current densities. (a) $J_0 = 10^{-3}$ A/cm$^2$ (curve is indistinguishable from the current axis), (b) $J_0 = 10^{-6}$ A/cm$^2$, (c) $J_0 = 10^{-9}$ A/cm$^2$. For all cases the reaction is O + e $\leftrightarrow$ R with $\alpha = 0.5$ and T = 298 K. (Adapted from A. J. Bard and L. R. Faulkner, *Electrochemical methods: fundamentals and applications 2nd ed.* **2001**, p101)

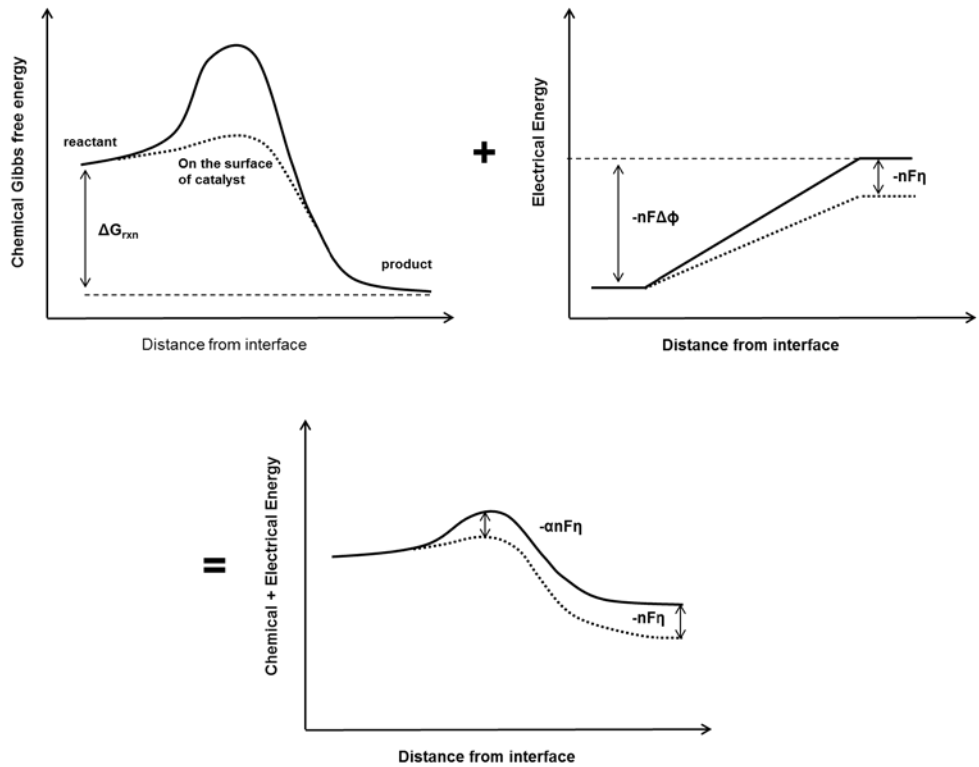


**Figure 1.3.** Electrocatalysis on the surface of a catalyst in electrochemical cell.

## 1.2. Polymer electrolyte membrane fuel cell

As a system using the energy of hydrogen, a fuel cell is expected to play a key role for future energy system. From solar energy or water electrolysis, hydrogen can be produced and thus, used as a fuel. In addition, electricity generated from the fuel cell can be used to various applications by storing in a secondary battery or ultra-capacitor.[1] As shown in Table 1.1, several types of fuel cells exist depending on the type of electrolyte; polymer electrolyte membrane fuel cell (proton exchange or hydroxyl ion exchange), phosphoric acid fuel cell (PAFCs), molten carbonate fuel cells (MCFCs), and solid oxide fuel cells (SOFCs). In particular to polymer electrolyte membrane fuel cell, since the fuel cell has a relatively low operating temperature, can be miniaturized, has high energy density and a selectivity of fuel as hydrogen or methanol, it focuses heavily on the application of portable devices, automobiles, and residential power generation.[2]

Polymer electrolyte membrane fuel cell is operated by fuel oxidation (hydrogen or alcohol) at the anode and oxygen reduction at the cathode. Hydrogen oxidation reaction (HOR) at the anode occurs following two different reaction pathways (Tafel-Volmer and Heyrovsky-Volmer) involving two electrons.[3,4,5] In general, HOR is highly facile on the surface of platinum, however, it shows significantly slow kinetics in the case of occurring adsorption of CO simultaneously (CO poisoning). Up to now, $H_2$ gas is mostly produced by hydrocarbon reforming, and it results in the formation of a significant amount of CO.[6] (~ 1%) Hydrogen oxidation occurs by the reactions in acidic media and basic media as below (S indicates a surface active site) [5];

Acidic media: $H_2$ -> S-H + S-H (Tafel)

$H_2 + H_2O \rightarrow H_3O^+ + e^- + S\text{-}H$ (Heyrovsky)

$S\text{-}H + H_2O \rightarrow H_3O^+ + e^- + S$ (Volmer)

Basic media: $H_2$ -> S-H + S-H (Tafel)

$H_2 + OH^-$ -> $H_2O + e^-$ +S-H (Heyrovsky)

S-H + $OH^-$ -> $H_2O + e^-$ (Volmer)

In the case of using inexpensive reformate ($H_2$ with CO impurity) as the fuel, CO is preferentially adsorbed on Pt surface (S), and suppress oxidation of $H_{ad}$ and dissociation of $H_2$.[7-9] Furthermore, CO poisoning is even more critical in alcohol oxidation and this causes a significant drop of cell performance.[10-12] To minimize the adverse effects of CO, there have been many attempts to facilitate the electrooxidation of CO on the catalyst's surface.[6,13-15]

The oxygen reduction reaction (ORR) is well known as the rate-determining reaction of operating a polymer electrolyte membrane fuel cell. In general, Pt exhibits the most excellent activity as a single substance, however, ORR using Pt still can not meet to facile anode reaction. In order to increase the activity of Pt catalyst and reduce a loaded weight of it, Pt-alloy catalysts have been intensively developed for some decades. ORR is an electrochemical reaction in which four electrons are involved as oxygen is converted to water (in acid) or hydroxyl ion (in base) on the electrode. Oxygen reduction occurs on the Pt surface by the reactions in acidic media and basic media as below (S indicates a surface active site)[16-18];

Acidic media: $O_{2(g)} + 4H^+_{(aq)} + 4e^-$ -> $2H_2O_{(l)}$

Basic media: $O_{2(g)} + 2H_2O_{(l)} + 4e^-$ -> $4OH^-_{(aq)}$

These reactions are composed of very complicating elementary steps and various reaction intermediates can be involved. (Figure 1.4) The rate determining step of this reaction varies slightly depending on the electrode material and there have

been many theoretical calculations and experimental approach to enhance reaction rate of the rate determining step. Basically, enhancement by Pt-alloy catalyst is explained by tuning the electronic structure of Pt. By the band theory, split-off of bonding and antibonding state of d-band metal is directly related to the strength of chemisorption of the reactant on the metal as shown in Figure 1.5. D-band center of the metal shows tendency of the chemisorption and this descriptor can be tuned by alloying with second metal species.[18-21] In chemical catalysis, Sabatier principle gives linkage between theoretical approach and experimental design. The principle states that the interactions between the catalyst and the substrate should be appropriate; neither too strong nor too week. This indicates that catalytic activity has optimum value and shows volcano-like behavior as depicted in Figure 1.6. From this view, many single substrate and Pt-alloy catalysts have been compared and positioned following volcano plot. In many experimental approaches, various effects on the surface of Pt are reported by synthesis of Pt-alloy such as ligand effect, strain effect, and geometric effect etc.[22,23] These effects are also explained by changes of adsorption energies of reaction intermediate on Pt surface consequently. Therefore, since the effects induced from metal alloy is in line with tuning the adsorption energy, these approaches are regarded as a kind of effort of moving the activity ‘along’ the ridge of the volcano.

However, there is one more effect for Pt-metal alloy, which is called as bifunctional effect generally interchanged with the term of oxophilic effect. In general, bifunctional effect indicates functions of different kinds of two sites for one reaction. More specifically, the effect is understood as an interaction between oxygen species on second metal and adsorbed species on Pt in the vicinity of the second metal[24-26] as shown in Figure 1.7. The effect of increasing oxphilicity on Pt surface is expected to bring enhanced activity escaping from volcano-like trend and has been mainly observed in methanol oxidation reaction, carbon monoxide (CO) oxidation in both acid and alkaline media and hydrogen oxidation in alkaline

electrolyte. However, bifunctional effect and the other effects usually work together in the electrocatalytic system and it is hard to obtain separated understanding on bifunctional effect in a real electrochemical system, and thus there have been a few efforts on measuring bifunctional effect experimentally.[27] In the CO oxidation described above, the oxophilic effect on Pt electrocatalyst was confirmed, however, there are controversies in which one is dominant effect between bifunctional effect and electronic effect (tuning of adsorption energy) of Pt alloy in HOR. HOR in the alkaline electrolyte is slower than that in the acidic electrolyte and Pt alloys have been often introduced to enhance the rate of the reaction. As representative catalysts for alkaline anion exchange membrane fuel cell (AEMFC, one kind of polymer electrolyte membrane fuel cell), PtRu alloy and Ni@Pt core/shell-like catalysts were characterized and it was suggested that electronic effect has the dominant portion in reason of superior activities of those catalysts.[28,29] In addition, there were reports about hydrogen oxidation which was solely depended on hydrogen binding energy on metal surface.[30-32] Nevertheless, the bifunctional effect still could exist for the catalyst based on Pt-alloy synthesis and these reports could not seem to have an understanding of electronic effect perfectly separated from bifunctional effect. Furthermore, critical reports for alkaline media still propose the importance of bifunctional effect for electrocatalysis,[33-35] and thus it is required that deeper understanding of bifunctional effect and electronic effect for more effective designs of the electrocatalysts using the effects.

| | proton exchange membrane fuel cell | alkaline anion exchange membrane fuel cell | phosphoric acid fuel cell | molten carbonate fuel cell | solid oxide fuel cell |
|---|---|---|---|---|---|
| electrolyte | polymer membrane | polymer membrane | polymer membrane | molten carbonate | ceramic |
| charge carrier | $H^+$ | $OH^-$ | $H^+$ | $CO_3^{2-}$ | $O^{2-}$ |
| operating temperature | 80℃ | 60-220 ℃ | 200 ℃ | 650 ℃ | 600-1000 ℃ |
| catalyst | platinum | platinum (carbon) | platinum | nickel | perovskites |
| cell component | carbon-based | carbon-based | carbon-based | stainless-based | ceramic-based |
| fuel compatibility | $H_2$, alcohol | $H_2$, alcohol | $H_2$ | $H_2$, $CH_4$ | $H_2$, $CH_4$, CO |

**Table 1.1.** Classification of fuel cell according to their electrolytes.

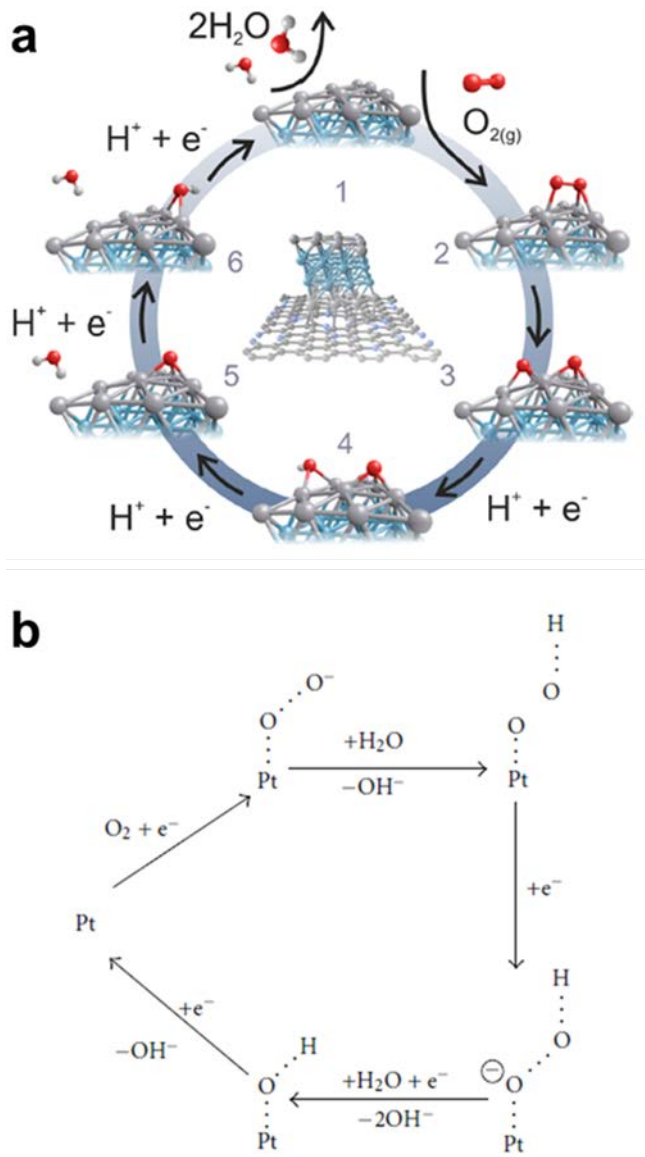


**Figure 1.4.** (a) Reaction scheme of the dissociative mechanism for oxygen reduction reaction (ORR) on $PtNi_{CS}$-N-GS in acid media and (b) electrocatalytic inner-sphere electron transfer mechanism for ORR on Pt surface in alkaline media. (Adapted from E. Gracia-Espino et al., *J. Phys. Chem. C* **2014**, *118*, 2804 and N. Ramaswamy and S. Mukerjee, *Adv. Phys. Chem.* **2012,** *2012*, 1)

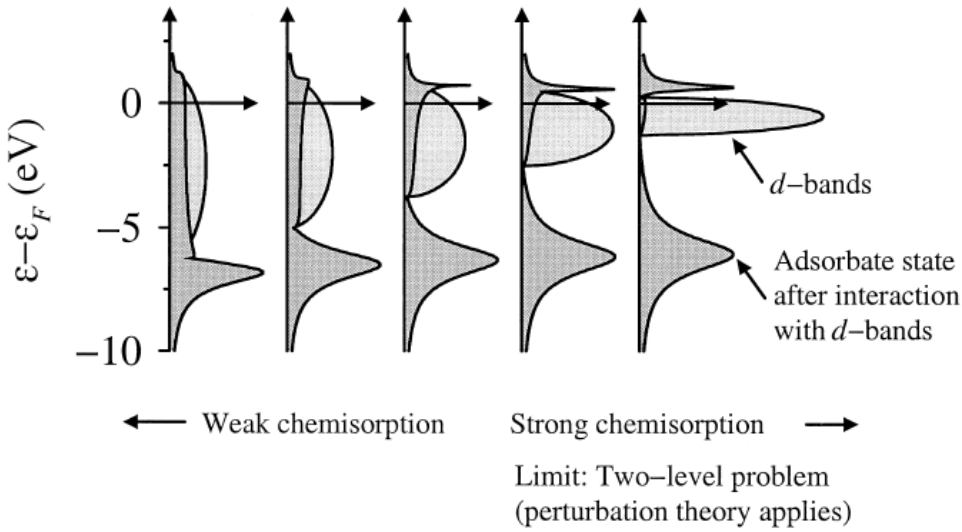


**Figure 1.5.** Density of states for adsorbate state interacted with the different orbitals (Adapted from B. Hammer and J.K. Norskov, *Adv. Catal.* **2000**, *45*, 71)

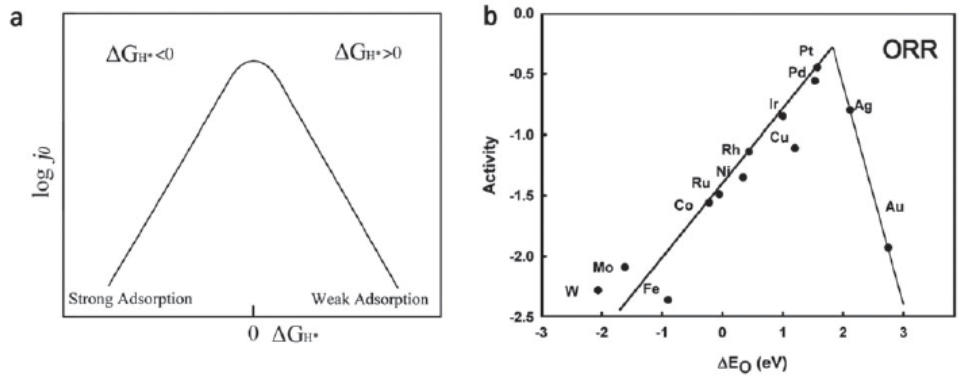


**Figure 1.6.** Volcano plots for different surfaces. (a) Relationship between $J_0$ and hydrogen adsorption free energy under the assumption of Langmuir adsorption model. (b) ORR activity for a range of pure metals plotted against O* adsorption energy. (Adapted from Y. Jiao et al., *Chem. Soc. Rev.* **2015**, *44*, 2060)

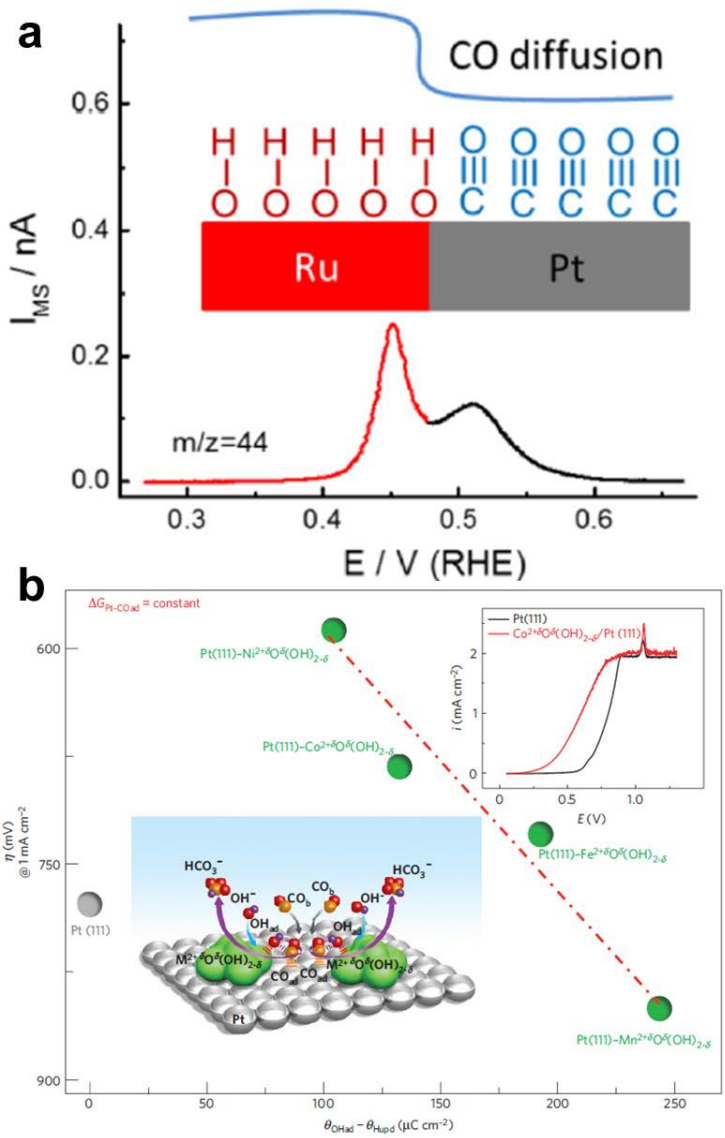


**Figure 1.7.** Bifunctional effect for CO oxidation. (a) Bifunctional effect between Pt and Ru substrate in acidic media (b) CO oxidation trend is shown as function of the 3d transition elements in alkaline media. (Adapted from H. Wang and H.D. Abruna, *J. Phys. Chem. Lett.* **2015**, *6*, 1899 and R. Subbaraman et al., *Nat. Mater.* **2012**, *11*, 550)

## 1.3. Water electrolysis cell

After the first industrial revolution and the second industrial revolution, rapidly developed technologies have brought great opportunity to us. However, since these technologies are based on the carbon-based fuels (coal and petroleum etc.), depletion of these resources begin to threaten our industry and their adverse effects on our environment are increasing. In order to solve these problems, regenerative and environmental-friendly resources become good alternatives. Electrochemical water splitting (water electrolysis) for a production of hydrogen fuel is regarded as an essential component of clean-energy technology. (Figure 1.8) Hydrogen has demonstrated its possibility as an ideal energy carrier for a sustainable energy economy due to its high energy density and environmental-friendly production. In the water electrolysis, catalytic activities of electrodes are still insufficient to commercial production and oxygen evolution reaction (OER) in both acidic and alkaline media is concerned as a rate determining reaction for operating water electrolysis cell. OER which is four-electron involved reaction requires high overpotential to overcome the kinetic barrier. Researches on electrochemical OER have been actively conducted in recent decades and various catalysts have been proposed to improve the reaction rate and stability during the cell operation.

Oxygen evolution in acidic media occurs by the reaction (A) and its elementary steps (a-c) as below (S indicates a surface active site)[36];

$$\text{(A) } 2H_2O_{(l)} \rightarrow O_{2(g)} + 4H^+_{(aq)} + 4e^-$$

$$\text{(a) } S + H_2O \rightarrow S\text{-}OH^* + H^+ + e^-$$

$$\text{(a') } S\text{-}OH^* \rightarrow S\text{-}OH$$

$$\text{(b) } S\text{-}OH \rightarrow S\text{-}O + H^+ + e^-$$

$$\text{(b') } S\text{-}OH + S\text{-}OH \rightarrow S\text{-}O + H_2O$$

$$\text{(c) } S\text{-}O + S\text{-}O \rightarrow 2S + O_2$$

(a) is water-dissociation step on surface active site. (a') is a rearrangement of intermediate OH via surface reaction. (b) and (b') are steps of oxygen formation on the surface and in parallel, depending on the adsorption strength of the intermediate. (c) is recombination step for the evolution of oxygen gas. From these reaction step, it is indicated that dissociation of water has to occur for the entire process of oxygen evolution in acidic media, and thus this step can have significant overpotential for various catalysts. $RuO_2$ exhibits great OER activity in both acidic and alkaline media, but this material has been considered unsuitable due to its low stability in highly oxidative potential. $IrO_2$ also exhibits good OER activiy and higher stability than that of $RuO_2$, however, $IrO_2$ has often suffered from dissolution as a similar problem of $RuO_2$. Nevertheless, $IrO_2$, $RuO_2$, and alloy-type oxide between Ru, Ir, Ce, Ti, and Sr were extensively studied in order to enhance OER kinetics and stabilities,[36-41] and it seems that there is no alternative to these materials due to harsh anodic condition in acidic OER.

However, oxygen evolution in alkaline media is faster than that in acidic media and it occurs in the range of lower potential (vs. standard hydrogen electrode), and thus numerous kinds of catalysts have been reported for this reaction. For instance, various kinds of perovskite, spinel, the layered double hydroxides, metal chalcogenide, pnictides, organometallics and non-metal electrocatalysts have been applied to this reaction and it has been extensively proposed that structural, compositional and physicochemical optimization of these materials.[42-44] Oxygen evolution in basic media occurs by the reaction (B) and its elementary steps (a-c) as below (S indicates a surface active site)[16,44-46];

$$(B)\ 4OH^-_{(aq)} \rightarrow 2O_{2(g)} + 2H_2O_{(l)} + 4e^-$$

$$(a)\ S + OH^- \rightarrow SOH$$

$$(b)\ SOH + OH^- \rightarrow SO + H_2O$$

(b') $SO + OH^- \rightarrow SOOH + e^-$

(c) $2SO \rightarrow 2S + O_2$

(c') $SOOH + OH^- \rightarrow S + O_2 + H_2O$

In the OER mechanism in alkaline media, SOOH (peroxide intermediate) can be involved in reaction steps. In some case of previous reports, it was suggested that peroxide intermediate could be also involved in acidic OER, and Figure 1.9 shows related OER mechanisms in both media.

As a counter reaction of OER, hydrogen evolution reaction (HER) has been also studied and highly active and stable catalysts have been reported. In the hydrogen evolution reaction, Pt-based catalysts show negligible overpotentials and excellent kinetics in acidic electrolyte and also show the best performance in alkaline electrolyte. In addition, due to high price and scarcity of Pt, there have been many reports about non-Pt catalysts with Pt-like catalytic behaviors. Metal nitrides, chalcogenides, borides, carbides, and phosphides were developed for HER application. However, there are still challenges with durability and activity problem in acidic media.[47-49] More importantly, low HER activities of catalyst in alkaline media is observed as matched with the case of HOR. Hydrogen evolution occurs by the reactions in acidic media and basic media as below (S indicates a surface active site)[5,47];

Acidic media: $H_3O^+ + e^- + S \rightarrow S\text{-}H + H_2O$ (Volmer)

$H_3O^+ + e^- + S\text{-}H \rightarrow H_2 + H_2O$ (Heyrovsky)

$S\text{-}H + S\text{-}H \rightarrow H_2$ (Tafel)

Basic media: $H_2O + e^- \rightarrow S\text{-}H + OH^-$ (Volmer)

$H_2O + e^- + S\text{-}H \rightarrow H_2 + OH^-$ (Heyrovsky)

$S\text{-}H + S\text{-}H \rightarrow H_2$ (Tafel)

In general, HER occurs following Volmer-Heyrovsky or Volmer Tafel step in both media. In these HER mechanisms, it is noteworthy that Volmer step in basic media is dissociation step of water and the step generally reduce the activities of HER catalysts including Pt catalyst. Pt catalyst is good catalysts for the adsorption and recombination of the $H_{ad}$, however, it is inefficient in the water dissociation step.[50]

For HER in alkaline media, water dissociation activity of $Ni(OH)_2$ when it is together with Pt catalyst recently attracts the attention. In 2011, N. Markovic group reported that oxophilicities of metal hydroxides and substrates critically influenced on HER activity in alkaline media.[50] (Figure 1.10) Furthermore, it was suggested that electrochemically deposited $Ni(OH)_2$ on Pt (111) substrate have excellent activity. In this system, bifunctionality could be observed of which $Ni(OH)_2$ promoted water dissociation and formation of $OH_{ad}$ and Pt provided adsorption site of $H_{ad}$ followed by recombination step. Together with this report, some cases of researching additional cationic effect, bifunctionality of $Ni(OH)_2$/other metal substrate, and practical approach by controlling the morphology of $Ni(OH)_2$ and Pt substrate were reported.[50-54] Therefore, it is concluded that oxophilicity and bifunctional effect also have a crucial role in HER alkaline media.

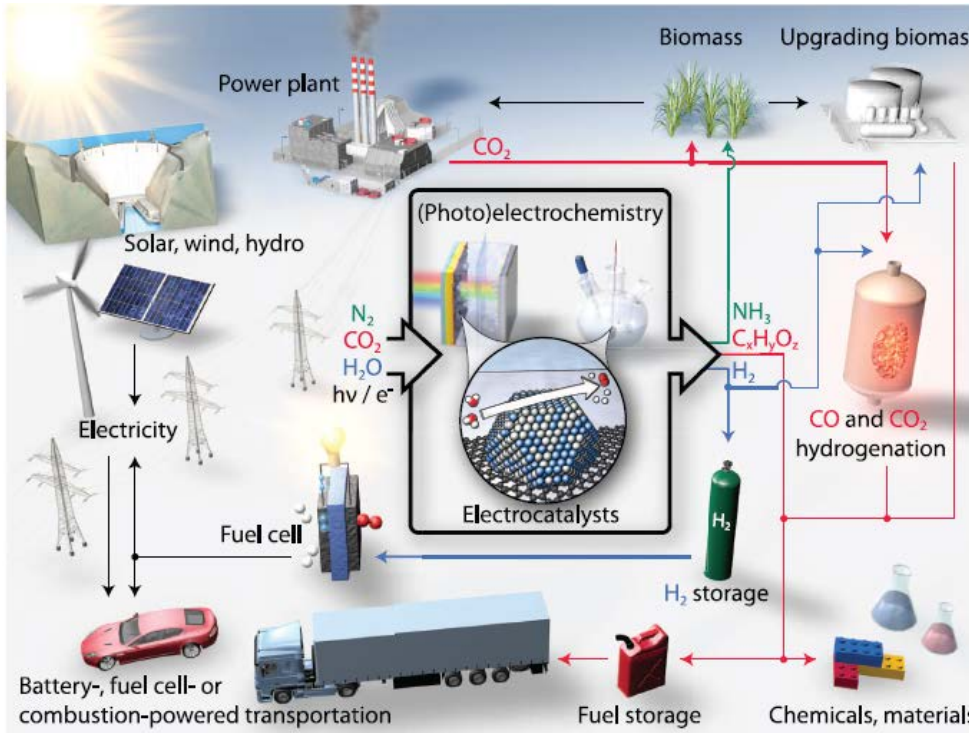


**Figure 1.8.** Sustainable energy future. Schematic of a sustainable energy landscape based on electrocatalysis. (Adapted from Z.W. Seh et al., *Science* **2017**, *355*, 146)

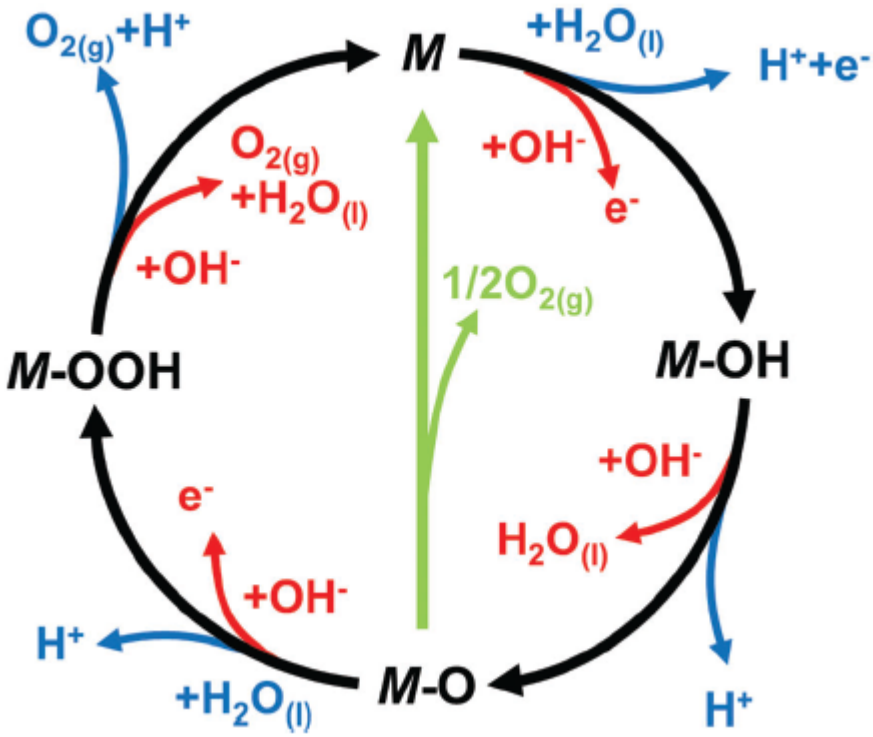


**Figure 1.9.** The OER mechanism for acid (blue line) and alkaline (red line) conditions. The black line indicates that the oxygen evolution involved the formation of a peroxide (M-OOH) intermediate (black line) while another route for direct reaction of two adjacent oxo (M-O) intermediates (green) to produce oxygen is possible as well. (Adapted from N.-T. Suen et al., *Chem. Soc. Rev.* **2017**, *46*, 337)

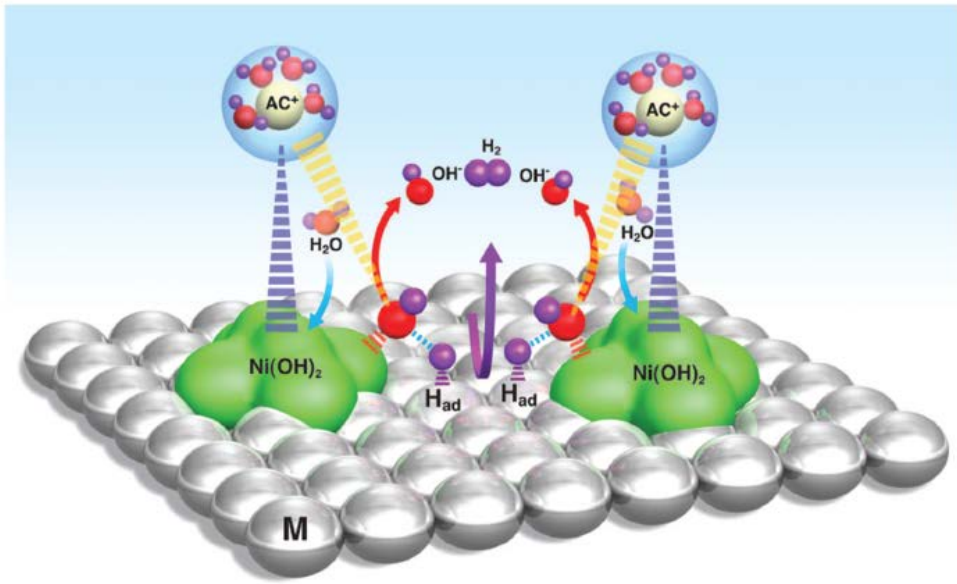


**Figure 1.10.** Schematic representation of water dissociation, formation of M-$H_{ad}$ intermediates, and subsequent recombination of two $H_{ad}$ atoms to form $H_2$ (magenta arrow) as well as $OH^-$ desorption from the $Ni(OH)_2$ domains (red arrows) followed by adsorption of another water molecule on the same site (blue arrows). Water adsorption requires concerted interaction of O atoms with $Ni(OH)_2$ (broken orange spikes) and H atoms with Pt (broken magenta spikes) at the boundary between $Ni(OH)_2$ and Pt domains. The $Ni(OH)_2$-induced stabilization of hydrated cations ($AC^+$) (broken dark blue spikes) likely occurs through noncovalent (van der Waals–type) interactions. Hydrated $AC^+$ can further interact with water molecules (broken yellow spikes), altering the orientation of water as well as the nature and strength of interaction of the oxide with water. (Adapted from R. Subbaraman et al., *Science* **2011**, *334*, 1256)

## 1.4. References


[1] Grimes, C. A.; Varghese, O. K.; Ranjan, S. *Light, Water, Hydrogen: The Solar Generation of Hydrogen by Water Photoelectrolysis*, Springer: New York, **2008**.

[2] Kordesch, K.; Simander, G. *Fuel Cells and their Applications*, VCH: Weinheim, **1996**.

[3] Sheng, W.; Gasteiger, H. A.; Shao-Horn, Y. *J. Electrochem. Soc.* **2010**, *157*, B1529-B1536.

[4] Rheinländer, P. J.; Herranz, J.; Durst, J.; Gasteiger, H. A. *J. Electrochem. Soc.* **2014**, *161*, F1448-F1457.

[5] Durst, J.; Siebel, A.; Hasché, F.; Herranz, J.; Gasteiger, H. A. *Energy Environ. Sci*. **2014**, *7*, 2255-2260.

[6] Hsieh, Y.-C.; Zhang, Y.; Su, D.; Volkov, V.; Si, R.; Wu, L; Zhu, Y.; An, W.; Liy, P.; He, P.; Ye, S.; Adzic, R. R.; Wang, J. X. *Nat. Commun.* **2013**, *4*, 2466.

[7] Urchaga, P.; Baranton, S.; Coutanceau, C.; Jerkiewicz, G. *Langmuir* **2012**, *28*, 3658−3663.

[8] Urchaga, P.; Baranton, S.; Coutanceau, C.; Jerkiewicz, G. *Langmuir* **2012**, *28*, 13094−13104.

[9] Baschuk, J. J.; Li, X. *Int. J. Energy Res.* **2001**, *25*, 695−713.

[10] Kowal, A.; Li, M.; Shao, M.; Sasaki, K.; Vukmirovic, M. B.; Zhang, J.; Marinkovic, N. S.; Liu, P.; Frenkel, A. I.; Adzic, R. R. *Nat. Mater.* **2009**, *8*, 325−330.

[11] García-Rodríguez, S.; Somodi, F.; Borbáth, I.; Margitfalvi, J. L.; Peña, M. A.; Fierro, J. L. G.; Rojas, S. *Appl. Catal., B* **2009**, *91*, 83−91.

[12] Gómez de la Fuente, J. L.; Martínez-Huerta, M. V.; Rojas, S.; Hernández-Fernández, P.; Terreros, P.; Fierro, J. L. G.; Peña, M. A. *Appl. Catal., B* **2009**, *88*, 505−514.

[13] Chung, D. Y.; Kim, H.-i.; Chung, Y.-H.; Lee, M. J.; Yoo, S. J.; Bokare, A. D.;

Choi, W.; Sung, Y.-E. *Sci. Rep.* **2014**, *4*, 7450.

[14] Alayoglu, S.; Nilekar, A. U.; Mavrikakis, M.; Eichhorn, B. *Nat. Mater.* **2008**, *7*, 333−338.

[15] Mukerjee, S.; Lee, S. J.; Ticianelli, E. A.; McBreen, J.; Grgur, B. N.; Markovic, N. M.; Ross, P. N.; Giallombardo, J. R.; De Castro, E. S. *Electrochem. Solid-State Lett.* **1999**, *2*, 12−15.

[16] Jiao, Y.; Zheng, Y.; Jaroniec, M.; Qiao, S. Z. *Chem. Soc. Rev.* **2015**, *44*, 2060-2086.

[17] Nørskov, J. K.; Rossmeisl, J.; Logadottir, A.; Lindqvist, L.; Kitchin, J. R.; Bligaard, T.; Jónsson, H. *J. Phys. Chem. B*, **2004**, *108*, 17886–17892.

[18] Hammer, B; Norskov, J. K. *Adv. Catal.* **2000**, *45*, 71-129.

[19] Greeley, J.; Stephens, I. E. L.; Bondarenko, A. S.; Johansson, T. P.; Hansen, H. A.; Jaramillo, T. F.; Rossmeisl, J.; Chorkendorff, I.; Nørskov, J. K. *Nat. Chem.* **2009**, *1*, 552−556.

[20] Stamenkovic, V. R.; Mun, B. S.; Arenz, M.; Mayrhofer, J. J.; Lucas, C. A.; Wang, G.; Ross, P. N.; Marković N. M. *Nat. Mater.* **2007**, *6*, 241-247.

[21] Stamenkovic, V. R.; Fowler, B.; Mun, B. S.; Wang, G.; Ross, P. N.; Lucas, C. A.; Marković, N. M. *Science* **2007**, *315*, 493−497.

[22] Kitchin, J. R.; Nørskov, J. K.; Barteau, M. A.; Chen, J. G. *Phy. Rev. Lett.* **2004**, *93*, 156801.

[23] Strasser, P.; Koh, S.; Anniyev, T.; Greeley, J.; More, K.; Yu, C.; Liu, Z.; Kaya, S.; Nordlund, D.; Ogasawara, H.; Toney, M. F.; Nilsson, A. *Nat. Chem.* **2010**, *2*, 454-460.

[24] Wang, H.; Abruña, H. D. *J. Phys. Chem. Lett.* **2015**, *6*, 1899−1906.

[25] Gasteiger, H. A.; Marković, N. M.; Ross, P. N.; Cairns, E. J. *J. Phys. Chem.* **1994**, *98*, 617−625.

[26] Mukerjee, S.; Urian, R. C. *Electrochim. Acta.* **2002**, *47*, 3219-3231.

[27] Lu, C.; Rice, C.; Masel, R. I.; Babu, P. K.; Waszczuk, P.; Kim, H. S.; Oldfield,

E.; Wieckowski, A. *J. Phys. Chem. B* **2002**, *106*, 9581−9589.

[28] Wang, Y.; Wang, G.; Li, G.; Huang, B.; Pan, J.; Liu, Q.; Han, J.; Xiao, L.; Lu, J.; Zhuang, L. *Energy Environ. Sci.* **2015**, *8*, 177−181.

[29] Lu, S.; Zhuang, Z. *J. Am. Chem. Soc.* **2017**, *ASAP*.

[30] Zheng, J.; Sheng, W.; Zhuang, Z.; Xu, B.; Yan, Y., *Sci. Adv.* **2016**, *2*, e1501602.

[31] Sheng, W.; Myint, M.; Chen, J. G.; Yan, Y. *Energy Environ. Sci.* **2013**, *6*, 1509–1512.

[32] Sheng, W.; Zhuang, Z.; Gao, M.; Zheng, J.; Chen, J. G.; Yan, Y. *Nat. Commun.* **2015**, *6*, 5848.

[33] Koper, M. T. M. *Nat. Chem.* **2013**, *5*, 255-256.

[34] Strmcnik, D.; Uchimura, M.; Wang, C.; Subbaraman, R.; Danilovic, N.; van der Vliet, D.; Paulikas, A. P.; Stamenkovic, V. R.; Markovic, N. M. *Nat. Chem.* **2013**, *5*, 300–306.

[35] Stamenkovic, V. R.; Strmcnik, D.; Lopes, P. P.; Markovic, N. M. *Nat. Mater.* **2017**, *16*, 57-69.

[36] de Faria, L. A.; Boodts, J. F. C.; Trasatti, S. *J. Appl. Electrochem.* **1996**, *26*, 1195-1199.

[37] Lee, Y.; Suntivich, J.; May, K. J.; Perry, E. E.; Shao-Horn, Y. *J. Phys. Chem. Lett.* **2012**, *3*, 399-404.

[38] Antolini, E. *ACS Catal.* **2014**, *4*, 1426-1440.

[39] Audichon, T.; Morisset, S.; Napporn, T. W.; Kokoh, K. B.; Comminges, C.; Morais, C. *ChemElectroChem* **2015**, *2*, 1128-1137.

[40] Audichon, T.; Napporn, T. W.; Canaff, C.; Morais, C.; Comminges, C.; Kokoh, K. B.; *J. Phys. Chem. C* **2016**, *120*, 2562-2573.

[41] Seitz, L. C.; Dickens, C. F.; Nishio, K.; Hikita, Y.; Montoya, J.; Doyle, A.; Kirk, C.; Vojvodic, A.; Hwang, H. Y.; Norskov, J. K.; Jaramillo, T. F. *Science*, **2016**, *353*, 1011-1014.

[42] Fabbri, E.; Habereder, A.; Waltar, K.; Kötz, R.; Schmidt, T. J. *Catal. Sci.*

*Technol.* **2014**, *4*, 3800-3821.

[43] Burke, M. S.; Enman, L. J.; Batchellor, A. S.; Zou, S.; Boettcher, S. W. *Chem. Mater.* **2015**, *27*, 7549-7558.

[44] Suen, N.-T.; Hung, S.-F.; Quan, Q.; Zhang, N.; Xu, Y.-J.; Chen. H. M. *Chem. Soc. Rev.* **2017**, *46*, 337-365.

[45] Wu, G.; Li, N.; Zhou, D.-R.; Mitsuo, K.; Xu, B.-Q. *J. Solid State Electrochem*. **2004**, *177*, 3682-3692.

[46] Zhuang, L.; Ge, L.; Yang, Y.; Li, M.; Jia, Y.; Yao, X.; Zhu, Z. *Adv. Mater.* **2017**, 1606793.

[47] Wang, J.; Xu, F.; Jin, H.; Chen, Y.; Wang. Y. *Adv. Mater.* **2017**, 1605838.

[48] Zeng, M.; Li. Y. *J. Mater. Chem. A* **2015**, *3*, 14942-14962.

[49] Zou, X.; Zhang, Y. *Chem. Soc. Rev.* **2015**, *44*, 5148-5180.

[50] Subbaraman, R.; Tripkovic, D.; Strmcnik, D.; Chang, K.-C.; Uchimura, M.; Paulikas, A. P.; Stamenkovic, V.; Markovic, N. M. *Science*, **2011**, *334*, 1256-1260.

[51] Subbaraman, R.; Tripkovic, D.; Chang, K.-C.; Strmcnik, D.; Paulikas, A. P.; Hirunsit, P.; Chan, M.; Greely, J.; Stamenkovic, V.; Markovic, N. M. *Nat. Mater.* **2012**, *11*, 550-557.

[52] Danilovic, N.; Subbaraman, R.; Strmcnik, D.; Chang, K.-C.; Paulikas, A. P.; Stamenkovic, V.; Markovic, N. M. *Angew, Chem. Int. Ed.* **2012**, *51*, 12495-12498.

[53] Wang, L.; Lin, C.; Huang, D.; Chen, J.; Jiang, L.; Wang, M.; Chi, L.; Shi, L.; Jin, J. *ACS Catal.* **2015**, *5*, 3801-3806.

[54] Yin, H.; Zhao, S.; Zhao, K.; Muqsit, A.; Tang, H.; Chang, L.; Zhao, H.; Gao, Y.; Tang, Z. *Nat. Commun.* **2015**, *6*. 6430.

# Chapter 2. Understanding the oxophilic effect for removal of CO poisoning in polymer electrolyte membrane fuel cell

## 2.1. Introduction

Proton exchange membrane fuel cells (PEMFCs) and direct alcohol fuel cells (DAFCs) are kinds of polymer electrolyte membrane fuel cell which convert chemical fuels into electrical energy in efficient and environmentally favorable means.[1-6] In PEMFCs and DAFCs, wherein hydrogen and alcohol are employed as fuels, respectively, Pt or Pt-transition metal alloys have shown unrivaled performances as electrocatalysts.[7-13] In general, $H_2$ gas production is mostly done by hydrocarbon reforming, and this process results in the formation of significant amount of CO. These CO gases adsorb on the Pt or Pt-alloy surface during the operation of PEMFCs, and there are considerable drop in the overall cell performance due to the suppression of $H_{ad}$ oxidation and $H_2$ dissociation.[14-16] The CO poisoning is even more critical in DAFCs, wherein CO is generated as a reaction intermediate during the decomposition of alcohol, and this causes decline of performance to a great extent.[1,17,18] In order to minimize the adverse influence of CO poisoning, there have been numerous attempts to facilitate the electrooxidation of CO adsorbed on the catalyst surface.[2,19-24]

Until now, research works on CO electrooxidation were focused on mechanism studies,[14,15,25-39] mainly on numerous factors which have influences on CO removal such as various electrochemical environments, diffusion coefficient of adsorbed CO ($CO_{ad}$), and origin of multiple CO oxidation peak potentials.

Marković and co-workers addressed the effects of temperature and particle size of Pt catalysts.[31,36,37] Wieckowski group investigated diffusion coefficient of CO on Pt surface by introduction of electrochemical-nuclear magnetic resonance (EC-NMR) technique.[33,34] Jerkiewicz and collaborators suggested that the origin of voltammetric features in CO electrooxidation is various surface domain of Pt nanoparticles,[14,15] and Abruña group recently proposed that the OH adsorbed on the Pt or Ru surface suppresses CO repopulation, resulting in multiple peaks during CO electrooxidation.[38] Moreover, mechanism studies of CO electrooxidation on Ru-modified Pt were also performed.[19,20,26,27,29,32,40] Above all, PtRu bimetallic catalysts are most outstanding in performance for electrooxidation of CO compared to other candidate Pt alloy catalysts, and this is mainly attributed to the electronic tuning of Pt d-band structure (electronic effect) and/or facilitation of CO oxidation by supplying oxygen species to $CO_{ad}$ on Pt surface (bifunctional effect or oxophilic effect).[19,23,25-27] On the other hand, there have been a few reports on utilization of metal oxide as support materials or mixing them with Pt based catalysts in order to enhance electrochemical activity and stability by increasing CO tolerance, and certain improvements were observed, though detailed mechanisms are still not clear and under investigations.[41-47]

Since both electronic and bifunctional mechanisms are known to contribute to the improvement of electrocatalytic CO oxidation, there have been efforts to address the influences of these effects.[28-30,48] In 2002, Masel, Wieckowski, and their colleagues verified that bifunctional effect is 4 times larger than electronic effect for CO removal on Ru decorated Pt surface by using temperature programmed desorption (TPD) method.[27] Also, Jeon et al. reported further enhancement in methanol oxidation reaction performance of PtRu/C catalysts induced by segregation of Pt and bifunctional effect.[49] These studies suggest the possibilities for the design of high-performance electrocatalyst by maximizing the bifunctional effect, implying the importance of bifunctional mechanism in CO

management. Therefore, understandings on the modification of electrocatalytic activities of state-of-the-art nanocatalysts by bifunctional effect are anticipated to provide some important clues for the design of high-performance electrocatalysts with excellent CO tolerance. However, to the best of my knowledge, there hasn't been a report on investigations on bimetallic catalyst system without electronic effect in real operation conditions.

In this study, a simple model system comprising blend of hydrous ruthenium oxide ($RuO_xH_y$) and Pt/C catalyst was introduced in order to investigate the electrocatalytic CO oxidation mechanisms and extended understanding of bifunctional effects. Contrary to conventional PtRu alloy catalyst, my catalyst system was expected to be feasible for the discussion of bifunctional effect separately, because of the unmodified crystallinity and electronic structure of Pt nanoparticles. Though the portion of Pt in direct contacts with $RuO_xH_y$ was inconsiderably small, significantly enhanced CO oxidation was observed by electrochemical measurements. Furthermore, facilitated CO oxidation in the blended catalyst of Pt/C and $RuO_xH_y$ in real fuel cell operation conditions were also confirmed by single cell experiments.

## 2.2. Experimental section

### 2.2.1. Preparation of electrocatalysts

Oxide blended catalyst ink was prepared by mixing 60 wt% Pt/C (Johnson Matthey), ruthenium (IV) oxide hydrate (99.9% $RuO_xH_y$, Sigma-Aldrich), 5 wt% Nafion® ionomer (Sigma-Aldrich, added as a binder) and isopropanol (Sigma-Aldrich). As a control sample, conventional catalyst ink composed of Pt/C, Nafion® ionomer and IPA was also prepared. After vigorous stirring and sonication, 3 μL of catalyst ink was dropped onto a glassy carbon substrate (geometric surface area: 0.196 $cm^2$). PtRu/C (75 wt%, Johnson Matthey) catalysts

were employed for comparison in the form of an ink with the same binder and solvent composition as described above.

### 2.2.2. Physical characterizations

The morphologies of $RuO_xH_y$ were characterized by transmission electron microscopy (TEM; JEOL JEM 2100 used) equipped with an energy dispersive spectroscopy (EDS) accessary, and X-ray diffraction (XRD) patterns were obtained by Rigaku D/MAX 2500 with Cu Kα radiation source. X-ray absorption near edge structure (XANES) measurements were performed in transmission mode at 8C beamline of Pohang Accelerator Laboratory (PAL). During the measurement, the beam was monochromatized with Si (111) monochromator, and the intensity was detuned by 20% in order to inhibit undesirable higher harmonics. X-ray photoelectron spectroscopy (XPS) spectra were recorded by KRATOS AXIS-HSi (Al Kα radiation source), and the results were analyzed by using XPSPEAK41 software. Scanning electron microscopy (SEM) and energy dispersive spectroscopy (EDS) analyses were carried out by using Carl Zeiss MERLIN and JEOL JSM 6701F in order to characterize the electrode structure and the presence of certain elements, respectively.

### 2.2.3. Electrochemical measurements

Electrochemical measurements were carried out by using a potentiostat (PGSTAT101, Autolab) based on a conventional three-electrode electrochemical cell comprising a glassy carbon (working electrode), a platinum wire (counter electrode), and a saturated calomel reference electrode. Cyclic voltammetry (CV) was performed in an electrochemical cell within the potential range of 0.05−1.05 V vs. reversible hydrogen electrode (RHE) with the scan rate of 20 mV/s. 0.5 M $H_2SO_4$ was used as an electrolyte, and Ar was continuously purged into the solution during the measurement. For the CO stripping analyses, CO molecules

were pre-adsorbed (chemisorption) on the surface of catalysts at 0.05 V vs. RHE by injecting 99% CO gas for 15 min followed by the removal of CO gas dissolved in the electrolyte by 30 min of Ar purging. CO stripping voltammetry was performed in 0.5 M $H_2SO_4$ in potential range of 0.05−1.05 V vs. RHE at various scan rates. For CO bulk oxidation testing, same measurement condition was applied with exceptions of scan rate which varied (5 mV/s, 20 mV/s, and 50 mV/s) and continuous CO gas feeds. Time-transient CO oxidation tests were also performed at 0.5 V, 0.6 V, 0.7 V, and 0.8 V (vs. RHE) after CO adsorption. Oxygen reduction reaction (ORR) polarization curves were obtained by using a rotating disk electrode (RDE) operated at 1600 rpm at the potential range from 0.05 to 1.05 V vs. RHE. The scan rate was 5 mV/s, and for the measurement, $O_2$ was continuously injected into the 0.5 M $H_2SO_4$ electrolyte. Forward sweeps of the ORR polarization cycle are shown in this study. In order to measure the hydrogen oxidation, RDE measurement was conducted in the range of -0.05 V to 0.8 V vs. RHE with a scan rate of 2 mV/s in 0.5 M $H_2SO_4$, under the presence of inbound flow of ultrapure $H_2$ or 100 ppm $CO/H_2$. All electrochemical measurements were performed at 20 °C which was controlled by a thermostat and a circulating jacket.

### 2.2.4. PEMFC analyses

Nafion® 212 membrane (Dupont) and carbon papers (SGL 35 BC) were used for the membrane electrode assembly (MEA). For PEMFC analyses, catalyst ink was prepared by mixing deionized water, Nafion® ionomer, and IPA with the catalysts. 60 wt% Pt/C were used for the anode and cathode catalyst layer of conventional MEA. Besides, to prepare modified anode, catalyst ink containing $RuO_xH_y$ (50% of Pt/C in weight) blended with Pt/C, Nafion® ionomer, and IPA was prepared. Dispersion of the inks was conducted by ultrasonic treatment, and catalyst layers were fabricated by spraying the ink on Nafion 212 membrane. Both of the total loadings of Pt in two MEAs were 0.2 $mg/cm^2$. For the single cell assembly, the

catalyst layers were sandwiched between the anode and cathode GDL (SGL 35 BC) without any thermal pressing. For measuring PEMFC performance, $H_2$ or 100 ppm $CO/H_2$ was injected into the anode with flow rate of 150 ml/min, and $O_2$ flow into the cathode with 200 ml/min was made. All the single cell analyses were performed at 70 °C.

### 2.2.5. Preparation and analyses of DMFCs

Nafion® 115 membrane (Dupont) and carbon papers (SGL 35 BC, Toray TGPH-060) were used for the membrane electrode assembly (MEA). For DMFC analyses, catalyst ink was prepared by mixing deionized water, Nafion® ionomer, and IPA with the catalysts. 75 wt% PtRu/C and 60 wt% Pt/C were used for the anode and cathode catalyst layer of conventional MEA, respectively. Besides, to prepare the modified cathode, catalyst ink containing $RuO_xH_y$ (50% of Pt/C in weight) blended with Pt/C, Nafion® ionomer, and IPA was prepared. Dispersion of the inks was conducted by ultrasonic treatment, and catalyst layers were fabricated by spraying the ink on Nafion 115 membrane. Total loadings of PtRu and Pt in both MEAs were 2.0 $mg/cm^2$. For the single cell assembly, the catalyst layers were sandwiched between the anode gas diffusion layer (GDL) (Toray TGPH-060) and cathode GDL (SGL 35 BC) without any thermal pressing. DMFCs were operated by supplying 3.0 M methanol solution and non-humidified air gas into anode and cathode. Flow rates of methanol solution and air were 0.5 ml/min and 200 ml/min, respectively. Electrochemical impedance spectroscopy (EIS) analyses of the single cells were conducted by using Zahner IM6 electrochemical workstation at 0.40 V, 0.45 V, 0.50 V, and 0.55 V with sinusoidal amplitude of 10 mV in the frequency range of 0.1 Hz to 10 kHz.

## 2.3. Results and discussion

### 2.3.1. Characterization of electrocatalysts and $RuO_xH_y$

Figure 2.1a shows the low-magnification scanning transmission electron microscope (STEM) image of blended electrocatalysts prepared by the same composition and method for the electrochemical measurements as described in the experimental section. Pt/C and bulky $RuO_xH_y$ were uniformly mixed with each other, and it was further verified by elemental EDS mapping results displayed in Figure 2.1b-2e. Figure 2f shows TEM image of a contact region between Pt/C and $RuO_xH_y$, and their detailed interfaces are imaged in Figure 2.1g. It was notable that a very small portion of Pt nanoparticles are in direct contact with $RuO_xH_y$, indicating that the number of Pt nanoparticles in touch with $RuO_xH_y$ in the whole region is negligible. The boundaries between Pt/C and $RuO_xH_y$ were observed by high resolution TEM, and the images are shown in Figure 2.1h and 2.1i. The lattice spacings of the Pt nanoparticles and $RuO_xH_y$ were 0.23 nm and 0.20 nm, which match with the d-spacings of Pt (111) and $RuO_2$ (210), respectively.

Figure 2.2a and 2.2b shows X-ray diffraction (XRD) and synchrotron X-ray absorption near edge structure (XANES) analyses results, respectively, which were performed in order to investigate the interactions between Pt and Ru. In the XRD patterns shown in Figure 2.2a, there are no evident crystalline peaks for $RuO_xH_y$, which manifests low crystallinity of $RuO_xH_y$ particles as in the case of TEM analysis and other previous reports.[18,50-52] In order to obtain XRD data of Pt/C and mixture of Pt/C and $RuO_xH_y$ (designated as Pt/C_ $RuO_xH_y$), the Pt/C and Pt/C_ $RuO_xH_y$ inks were deposited on a slide glass and dried in vacuum. The comparison between the patterns of these two samples reveals that there is no alteration in crystal structure nor indication of alloying by addition of $RuO_xH_y$. Pt $L_3$ edge XANES spectra of Pt/C and Pt/C_ $RuO_xH_y$ displayed in Figure 3b were obtained for the verification of possible electronic modification. In general, the white line

peak intensity indicates Pt d-band population, and increased peak intensity of the white line implies increased number of d-band vacancy and vice versa. As can be seen in Figure 2.2b, the Pt $L_3$ edge XANES spectra are the same for both samples, indicating that the d-band structure of Pt is not altered by the physical mixing of Pt and $RuO_xH_y$. It was additionally performed in situ XANES analyses in 0.5 M $H_2SO_4$ solution (Figure 2.3), and verified that there is still no electronic modification even in practical operation conditions.

In order to further address the chemical states of the Pt surfaces in Pt/C and Pt/C_$RuO_xH_y$, X-ray photoelectron spectroscopy (XPS) analysis was performed. Since XPS provides information of the surface, where the electrocatalytic reactions take place, XPS results may complement the XANES data which give the information of bulk properties. Pt 4f XPS spectra of Pt/C and Pt/C_$RuO_xH_y$ are displayed in Figure 2.2c and 2.2d, respectively, and the results were fitted into two sets of doublets (see Table 2.1 for detailed fitting results).[53-56] The differences in peak positions and ratio of $Pt^0$ and $Pt^{2+}$ states of the two samples were negligible, and this reveals that the surface chemical state of nano-sized Pt is not affected by $RuO_xH_y$.

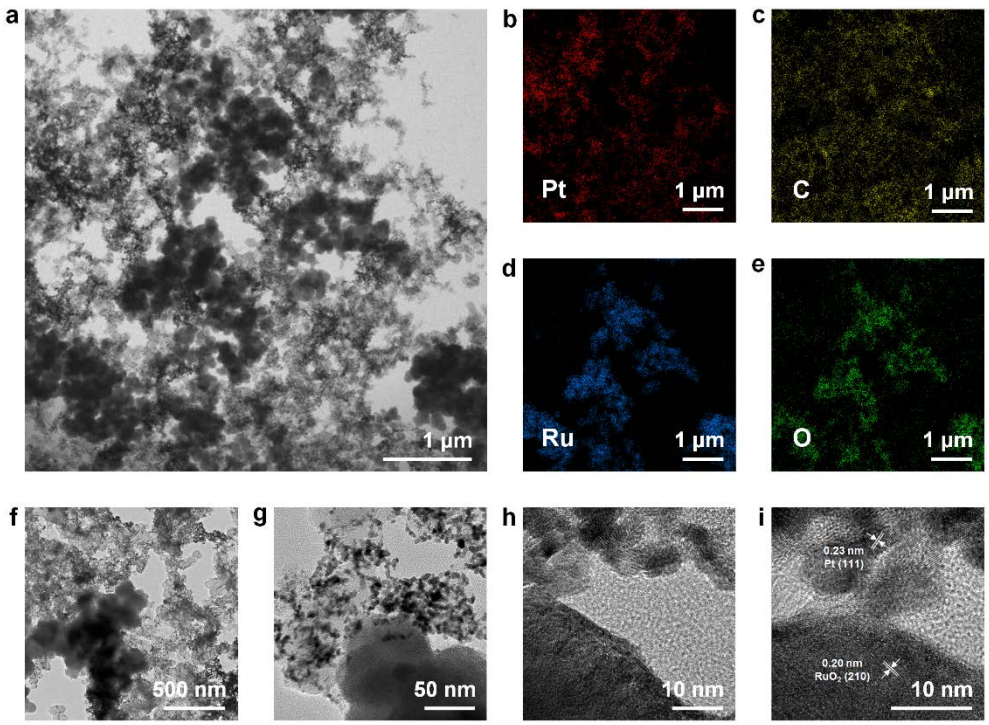


**Figure 2.1.** (a) STEM image of blended Pt/C catalysts and $RuO_xH_y$ particles, and the corresponding elemental EDS maps of (b) Pt, (c) C, (d) Ru, and (e) O. TEM images showing (f) the mixed catalysts and (g) the interface between Pt/C and $RuO_xH_y$. (h,i) HR-TEM images of blended Pt/C and $RuO_xH_y$ and their lattice spacing (i).

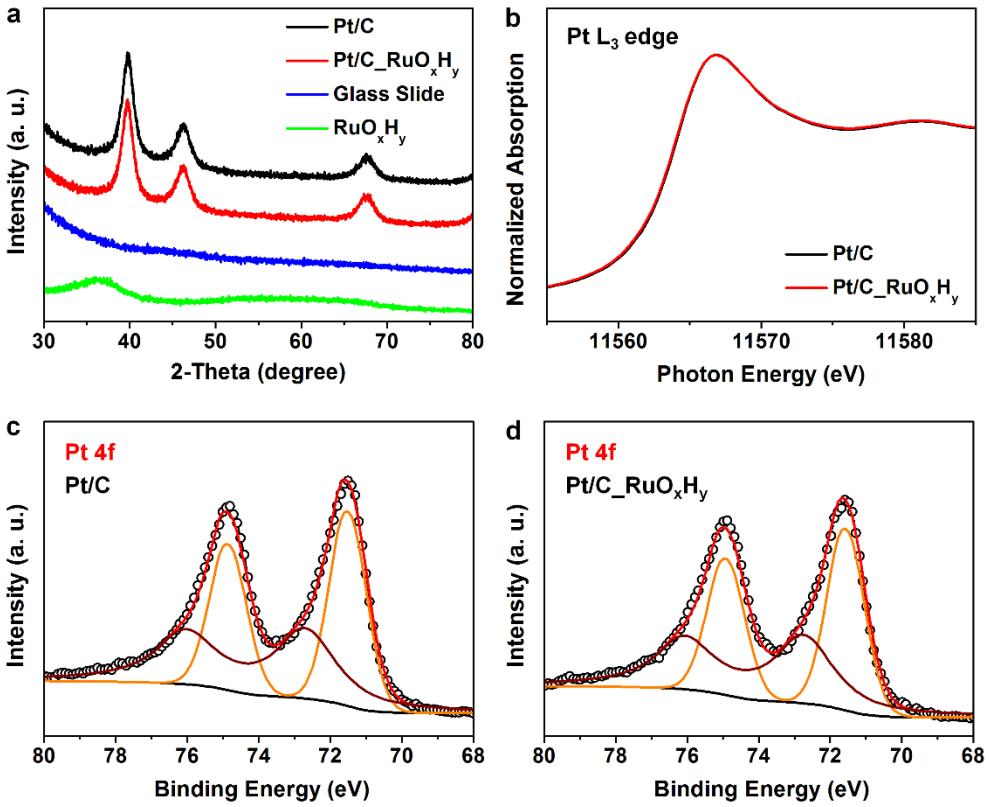


**Figure 2.2.** (a) XRD patterns of Pt/C, Pt/C_ $RuO_xH_y$, and $RuO_xH_y$. (b) XANES spectra of Pt/C and Pt/C_$RuO_xH_y$ at Pt $L_3$ edge. (c,d) Pt 4f XPS spectra of (c) Pt/C and (d) Pt/C_$RuO_xH_y$ with fitting results of $Pt^0$ (orange lines) and $Pt^{2+}$ (brown lines) states. The red lines show overall fitting results based on Shirly background (black lines). Bare and blended Pt catalysts were deposited on glass slides in ink form for the XRD and XPS measurements, and the XANES spectra were obtained by the inks deposited on carbon papers.

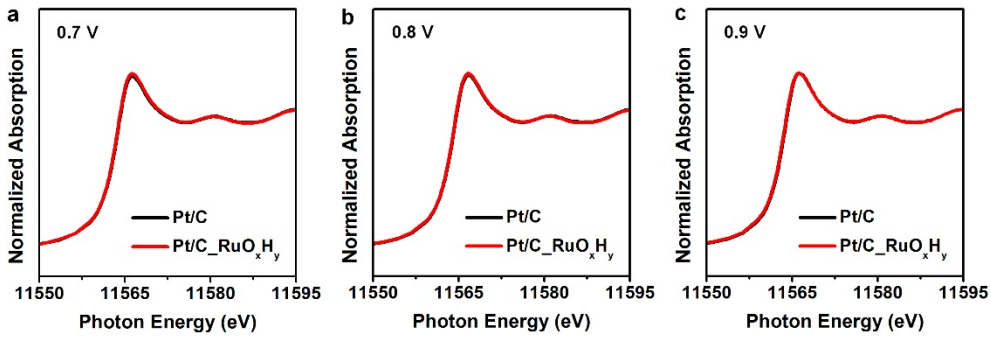


**Figure 2.3.** *in situ* XANES spectra of Pt/C and Pt/C_$RuO_xH_y$ deposited on carbon paper at Pt $L_3$ edge in 0.5 M $H_2SO_4$ solution at (a) 0.7 V, (b) 0.8 V, and (c) 0.9 V. All of the measurements were performed after 600 s for current saturation in order to allow the surface of Pt catalysts to reach at equilibrium state (e.g. equilibrated $OH_{ad}$ coverage on Pt surface).

| | Pt $4f_{7/2}$ Binding Energy (eV) | | Area Ratio (%) | |
|---|---|---|---|---|
| | $Pt^0$ | $Pt^{2+}$ | $Pt^0$ | $Pt^{2+}$ |
| Pt/C | 71.51 | 72.69 | 55.05 | 44.95 |
| Pt/C_$RuO_xH_y$ | 71.57 | 72.73 | 54.92 | 45.08 |

**Table 2.1.** Fitted results of the Pt 4f XPS spectra of Pt/C and Pt/C_$RuO_xH_y$.

### 2.3.2. Electrochemical measurements

In order to confirm the effect of $RuO_xH_y$ on electrocatalytic activities, cyclic voltammetry (CV) analysis based on a three electrode system were performed in 0.5 M $H_2SO_4$ electrolyte. As shown in the cyclic voltammogram displayed in Figure 2.4a, the peak potentials of Pt/C_ $RuO_xH_y$ in OH adsorption/desorption region is located between those of Pt/C and $RuO_xH_y$, indicating that the Pt and $RuO_xH_y$ in Pt/C_$RuO_xH_y$ do not behave independently in the electrochemical environment. Meanwhile, since the large current density due to the capacitive properties of $RuO_xH_y$ might affect the results of the other electrochemical analyses, background correction by subtraction of CV data were conducted in all of the voltammetric measurements.

Adsorption and oxidation characteristics of CO on Pt surface in Pt/C and Pt/C_$RuO_xH_y$ were investigated to address the interaction between Pt nanoparticles and $RuO_xH_y$ more clearly. Figure 2.4b shows the CO adsorption (replacement of adsorbed H by CO) current on the surface of the Pt/C, Pt/C_ $RuO_xH_y$, PtRu/C, and $RuO_xH_y$.[57] Any different CO adsorption behaviors of Pt/C and Pt/C_ $RuO_xH_y$ were hardly noticeable. In contrast, PtRu/C displayed a moderate CO adsorption behavior due to the alteration of CO adsorption energy on Pt surface (electronic effect by alloying) and, possibly, CO adsorption on the surface of Ru atoms. Meanwhile, there was no indication of CO adsorption on the surface of $RuO_xH_y$, implying that $RuO_xH_y$ itself is inert for COad oxidation reaction, probably due to the OH-rich $RuO_xH_y$ surface. Therefore, it could be neglected that the CO adsorption on the $RuO_xH_y$ surface in the blended sample (Pt/C_ $RuO_xH_y$).

Figure 2.4c shows the CO stripping currents exhibiting oxidative detachment of the monolayer-chemisorbed CO on the catalyst surface. In general, hydroxyl group promotes the oxidation of CO to $CO_2$, resulting in rapid removal of $CO_{ad}$.[23,28,53] Pt/C and Pt/C_ $RuO_xH_y$ displayed multiple peaks during the oxidation

of $CO_{ad}$ on the Pt surface as shown in Figure 2.4c. The appearance of the multiple peaks is mainly attributed to the surface heterogeneity and oxophilicity difference.[14] The onset potential of Pt/C_$RuO_xH_y$ is found to be much lower than that of Pt/C (0.55 V and 0.65 V for Pt/C_$RuO_xH_y$ and Pt/C, respectively). The entire oxidation current of Pt/C_$RuO_xH_y$ looks as if the oxidation curve of Pt/C is squeezed down to the negative potential. The onset potential of PtRu/C is even lower than that of Pt/C_$RuO_xH_y$, mainly due to the presence of both electronic modification and bifunctional effect within sub-nanometer distance. A significantly larger area under the CO oxidation current in the case of PtRu/C, which indicates a larger active surface area of PtRu/C compared to Pt nanocatalysts, can be attributed to CO adsorption on metallic Ru located at the surface (see Figure 2.5). $RuO_xH_y$ without neighboring Pt showed small current in potential regions larger than 0.6 V vs. RHE, but this current is expected to be irrelevant to CO oxidation due to the lack of adsorption as displayed in Figure 2.4b. It seems that this current is ascribed to the bulk-oxidation of $RuO_xH_y$ materials. Additionally, in order to confirm that the presence of $RuO_xH_y$ did not induce any change to the crystallinity nor chemical states of Pt nanocatalysts during the reaction, XRD (Figure 2.6) and XPS (Figure 2.7) measurements on the catalysts before and after CO oxidation were performed, and it could not be observed that any notable differences. Absence of electronic modification in Ru species in Pt/C_$RuO_xH_y$ during the electrochemical measurements was also confirmed (Figure 2.8).

For a more detailed investigation on CO oxidation based on the peak potential positions, first derivative of CO stripping current was obtained, as displayed in Figure 2.4d. It shows that the CO oxidation potential peaks are apparent in lower potentials, forming an “early CO stripping region” at 0.55 – 0.7 V (see also Figure 2.4c). In the case of Pt catalysts, there have been many suggestions for the origin of the CO oxidation current at low potential.[58-60] Though there are still controversies on the detailed mechanism, it is generally accepted that

it is resulted from the weakly bound CO on the Pt nanocatalysts due to the repulsions between CO molecules. Oxygen species prefer to form at low-coordination site, displacing COad and forcing them to diffuse toward terraces. Therefore, CO populations on (111) and (100) planes increase, causing stronger repulsions between CO adsorbed on terraces and increased portion of weakly bound CO on Pt surface.[39] However, the defect sites at Pt surfaces are known to be fully covered by OH even at low potentials (~0.5 V).[38] In the case of Pt/C_ $RuO_xH_y$, wherein oxygen species are supplied from $RuO_xH_y$ to Pt, the early CO stripping region appears from 0.55 V. Therefore, the CO removal at low potentials is not resulted from the modifications of Pt defect sites by the presence of $RuO_xH_y$. The emergence of this region, together with the decreases in current at higher potentials, indicates that the introduction of $RuO_xH_y$ did enhance the CO oxidation properties, but in a way other than that originated from the increment of OH coverage at defect sites of Pt catalysts. It is even clearer in the CO stripping results at various scan rates (Figure 2.9a and 2.9b), wherein the signals from defect sites (at around 0.5 V) and the early CO stripping region (at > 0.55 V) are both observable.

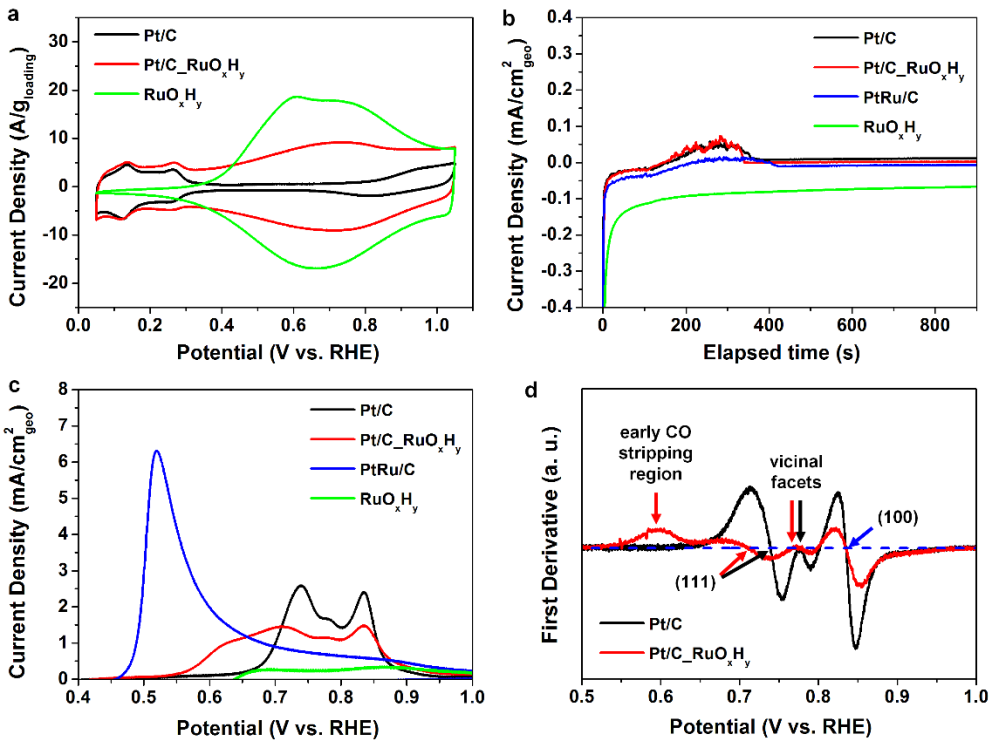


**Figure 2.4.** (a) Cyclic voltammograms of Pt/C, Pt/C_$RuO_xH_y$, and $RuO_xH_y$. (b) Time-transient CO adsorption currents with the onset of CO purging at 100 s after beginning the measurement. (c) Background-corrected CO stripping results measured at the scan rate of 20 mV/s after monolayer CO adsorption. (d) First derivative of the CO stripping currents displayed in (c).

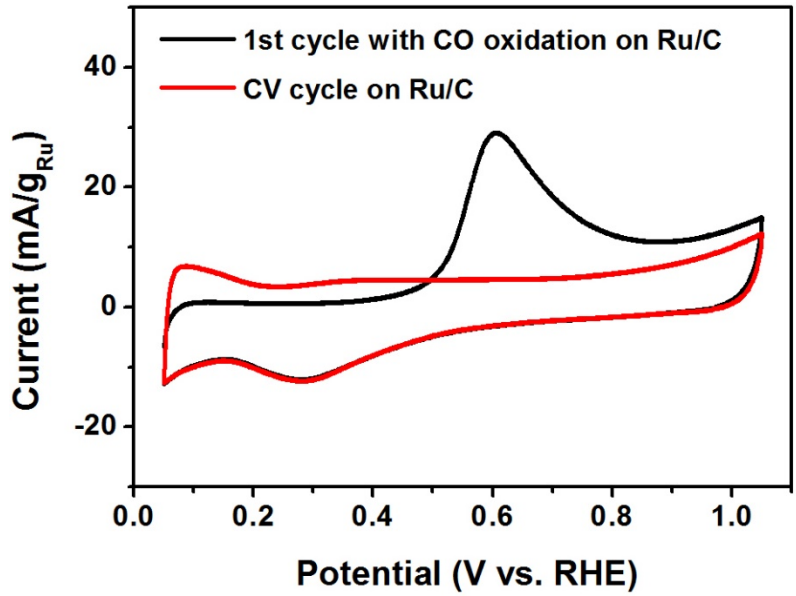


**Figure 2.5.** CV diagram of Ru/C (E-TEK, 60 wt%) in 0.5 M $H_2SO_4$ measured after monolayer adsorption of CO (black line) and without the presence of CO (red line) by Ar purging.

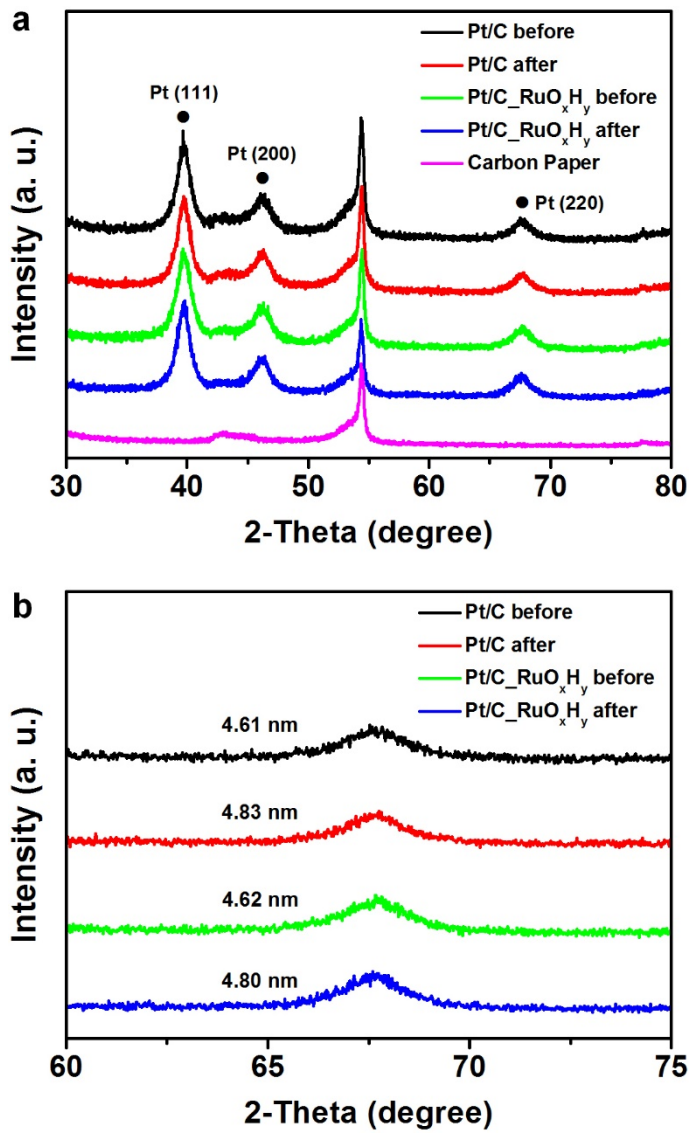


**Figure 2.6.** (a) XRD patterns of Pt/C and Pt/C_$RuO_xH_y$ deposited on carbon paper measured before and after the 40 cycles of CV and CO stripping (scan rate: 20 mV/s). (b) Enlarged XRD patterns of Pt (220) peaks displayed in (a) and the average crystallite sizes calculated by using Scherrer's equation.

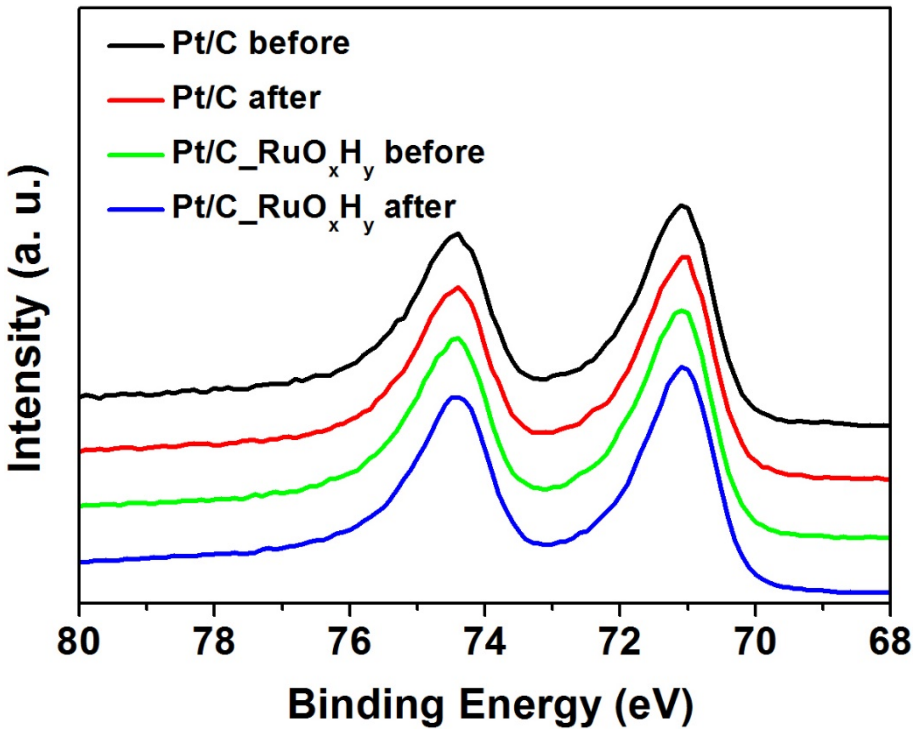


**Figure 2.7.** Pt 4f XPS spectra of Pt/C and Pt/C_RuOxHy deposited on carbon paper, before and after the 40 cycles of CV and CO stripping measurements (scan rate: 20 mV/s).

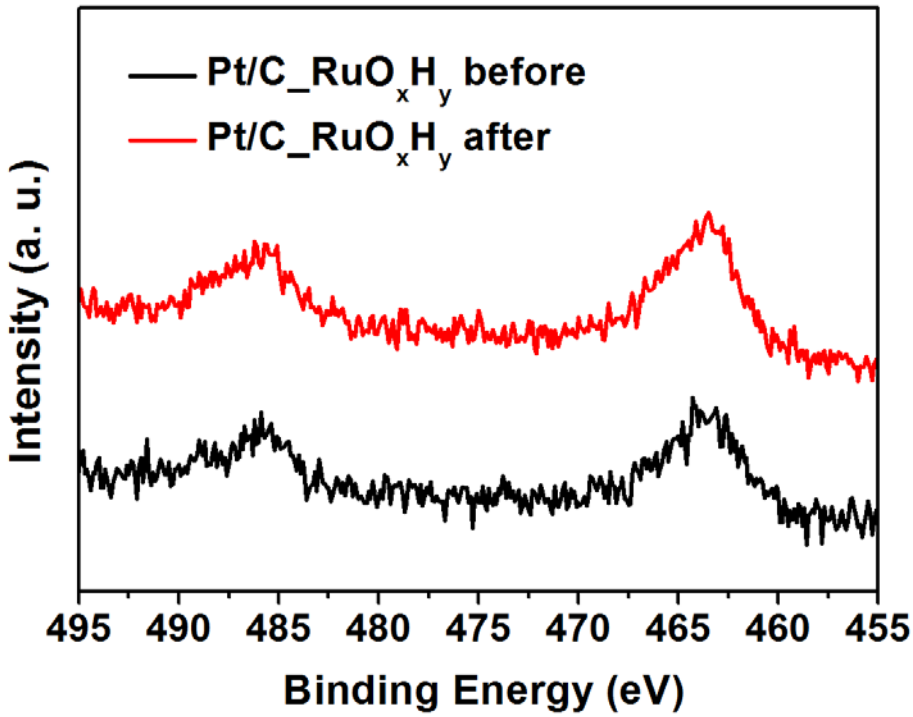


**Figure 2.8.** Ru 3p XPS spectra of Pt/C_$RuO_xH_y$ deposited on carbon paper measured before and after the 40 cycles of CV and CO stripping (scan rate: 20 mV/s).

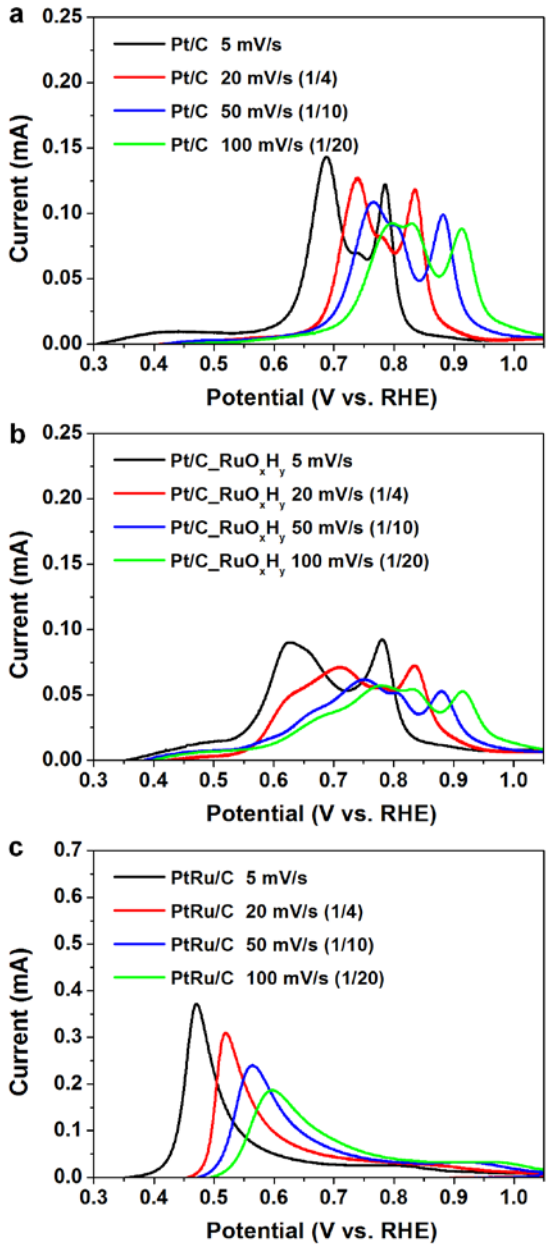


**Figure 2.9.** Background-corrected CO stripping results measured at various scan rates after monolayer CO adsorption on (a) Pt/C, (b) Pt/C_$RuO_xH_y$, and (c) PtRu/C. The CO oxidation currents obtained by measurements at 20 mV/s, 50 mV/s, and 100 mV/s were divided by 4, 10, and 20, respectively, for convenient comparisons.

For the investigation of CO oxidation in dynamic conditions and for the direct observation of modified oxophilicity, CO bulk oxidation analyses were performed in CO saturated 0.5 M $H_2SO_4$ solution. Figure 2.10a shows CO bulk oxidation currents which were obtained by backward sweeps of potential cycles.[61] Above certain high positive potentials, CO oxidation is sufficiently fast, and current reaches a limiting value that is controlled by rotation speed of RDE. As potential is swept in negative direction, coverage of oxygen species on the surface of Pt gradually decrease, resulting in a reduction of the oxidation currents. Since the oxygen species play a key-role in CO oxidation, maintenance of high current to lower potentials indicates superior CO oxidation property. The trend of the oxophilicities of Pt/C, Pt/C_$RuO_xH_y$, and PtRu/C in dynamic condition is consistent with the results of CO oxidation results displayed in Figure 2.4c. PtRu/C exhibited the best oxophilic characteristic, and this can be explained by electronic effect in addition to the bifunctional effect between the $OH_{ad}$ on Ru atoms that are adjacent to Pt. Nevertheless, Pt/C_$RuO_xH_y$ with negligible electronic interactions, displayed obvious enhancement in oxophilicity compared to the case of Pt/C, indicating that the phenomenon discussed above is still valid in dynamic conditions.

Figure 2.10b-10d show CO bulk oxidation currents measured by potential sweep in forward direction at three different scan rates; 5 mV/s, 20 mV/s, and 50 mV/s. In Figure 2.10b, two peaks are apparent at 0.64 V (near the CO oxidation potential of PtRu/C) and 0.81 V (vicinal region to the peak of Pt/C) in the case of Pt/C_$RuO_xH_y$. These two peaks were converged as the scan rate was increased, approaching the high CO oxidation potential of Pt/C.[38] Nevertheless, even after complete merging of the two peaks at the scan rate of 50 mV/s, CO oxidation potential was still lower in Pt/C_$RuO_xH_y$ compared to Pt/C. This result also coincides with the trend in CO stripping currents displayed in Figure 2.4c and Figure 2.10a. In addition to the confirmation on the increased oxophilicity, two distinct peaks of Pt/C_$RuO_xH_y$ (in the case of 5 mV/s scan) and the dependence of

their positions on the scan rate are noteworthy. The peak that appears in the lower potential is more sensitive to the increment of the scan rate, being shifted to a larger extent (0.63 V at 5 mV/s and 0.80 at 20 mV/s) and converged to the other peak at 50 mV/s. In contrast, the peak located at the higher potential moves within the range of 0.07 V (0.81 V at 5 mV/s and 0.88 V at 20 mV/s). This behavior was also observed in the monolayer CO stripping at various scan rates, as displayed in Figure 2.9. The difference between the degrees of peak potential shifts implies that there are at least two different origins of increased oxophilicity by the introduction of $RuO_xH_y$.

In 2012, Jerkiewicz and his colleagues investigated the time-transient CO stripping at various potentials and observed the CO oxidation by Eley-Rideal mechanism in time-transient CO stripping measurements and electrochemical quartz crystal nanobalance analyses.[15] They suggested formation of $COOH_{ad}$ on Pt surface by direct reaction between $CO_{ad}$ and $H_2O$, and showed that this type of CO oxidation is present when the CO coverage is high. In order to address the CO removal mechanism in the Pt/C_$RuO_xH_y$, time-transient analyses were performed. Figure 2.11a-11d display the CO bulk oxidation results at 0.5 V, 0.6 V, 0.7 V, and 0.8 V, respectively, and it is clear that Pt/C_ $RuO_xH_y$ exhibit superior CO oxidation property to Pt/C in all potentials. At sufficiently high potential ($\geq$ 0.8 V) for the formation $OH_{ad}$ on Pt surface, CO oxidation currents of Pt/C and Pt/C_$RuO_xH_y$ are comparable. This implies that Langmuir-Hinshelwood mechanism, which is strongly dependent on the $OH_{ad}$ coverage, is dominant for the CO removal in high potential range. As the potential decreases, the gap between the oxidation currents increases. At 0.5 V, there is no signal of CO oxidation from Pt/C, but Pt/C_$RuO_xH_y$ manifest substantial CO oxidation behavior even at this low potential. As mentioned above, low coordination sites of Pt surface is known to be completely filled with $OH_{ad}$ at 0.5 V during the CO oxidation measurement. Since there is no indication of CO removal in time-transient bulk CO oxidation at 0.5 V (Figure

2.11a), time-transient monolayer adsorbed CO oxidation was performed at 0.5 - 0.8 V in order to verify the difference between the monolayer and bulk CO oxidation, and the results are shown in Figure 2.12. It is clearly observable from the monolayer CO stripping at 0.5 V (shown in Figure 2.12a) that the CO removal takes place even on Pt/C at this potential. These different results indicate that in dynamic condition, where large amount of CO is continuously supplied to the Pt surface, the $OH_{ad}$ formation on the defect sites of Pt is not favored in low potential such as 0.5 V. In acidic environment, lifetime of $OH^-$ is very short because of the rapid reaction between $OH^-$ and $H^+$, which exists in the solution in large amount.[62,63] Therefore, it seems that $OH_{ad}$ on Pt surface results from the water dissociation at the Pt surface. However, when Pt surface is fully covered with CO, $OH_{ad}$ formation is unlikely to occur, because water dissociation cannot be catalyzed by Pt surface. Recalling that the portion of Pt nanoparticles in direct contact with $RuO_xH_y$ in Pt/C_$RuO_xH_y$ is negligible, and thus the probability of encounter between OH-rich $RuO_xH_y$ and poisoning CO adsorbed on the Pt surface is very small in amount, bulk CO removal at 0.5 V in the case of Pt/C_ $RuO_xH_y$ is unlikely to be attributed to the CO oxidation by Langmuir-Hinshelwood mechanism. Therefore, it could be concluded that the CO oxidation by direct reaction between COad and oxygen species that are not adsorbed on the Pt surface is present in the case of high CO coverage, following the Eley-Rideal mechanism. Considering that the difference between the Pt/C and Pt/C_$RuO_xH_y$ is the existence of $RuO_xH_y$ and that almost all of the Pt nanoparticles and $RuO_xH_y$ are not adjacent in general, it can be expected that the $RuO_xH_y$ affects the reaction between $H_2O$ and $CO_{ad}$ in a long distance. Ruthenium oxide is a well-known catalyst for water dissociation, and therefore it can alter the bond strength between O and H atoms in $H_2O$ molecules. It is well known that the switching between the covalent bond and hydrogen bond frequently occurs in chains of adjacent water molecules for proton conduction.[64,65] Thus it could be expected that the O-H bond strength of $H_2O$

molecule located in a certainly long distance can be tuned, though the distance limit for the valid activation is unclear. Significantly enhanced CO oxidation on Pt surface fully covered with CO at Pt/C_$RuO_xH_y$ seems to be originated from the changes in O-H bond strength in $H_2O$, enabling the formation of reaction intermediate ($COOH_{ad}$) more effectively.

In short, in the case of high CO coverage, large amount of oxygen species containing activated water molecule supplied to Pt catalysts can remove $CO_{ad}$ effectively without adsorbing on the Pt surface. This phenomenon is especially favorable for CO management, because reducing the CO population on the catalyst surface to a certain level (low coverage) would give rise to the CO oxidation by providing seats for the oxygen species to be adsorbed on Pt, enabling further CO removal by the Langmuir-Hinshelwood mechanism. From these observations on enhanced CO oxidation properties, It is proposed here that the meaning of bifunctional effect should not be confined to the hydroxyl group forming behavior of alloy metal (typically Ru), but rather include any type of promotion on CO oxidation by supplying oxygen species in catalyst system design other than preparation of atomic mixture. (Figure 2.13)

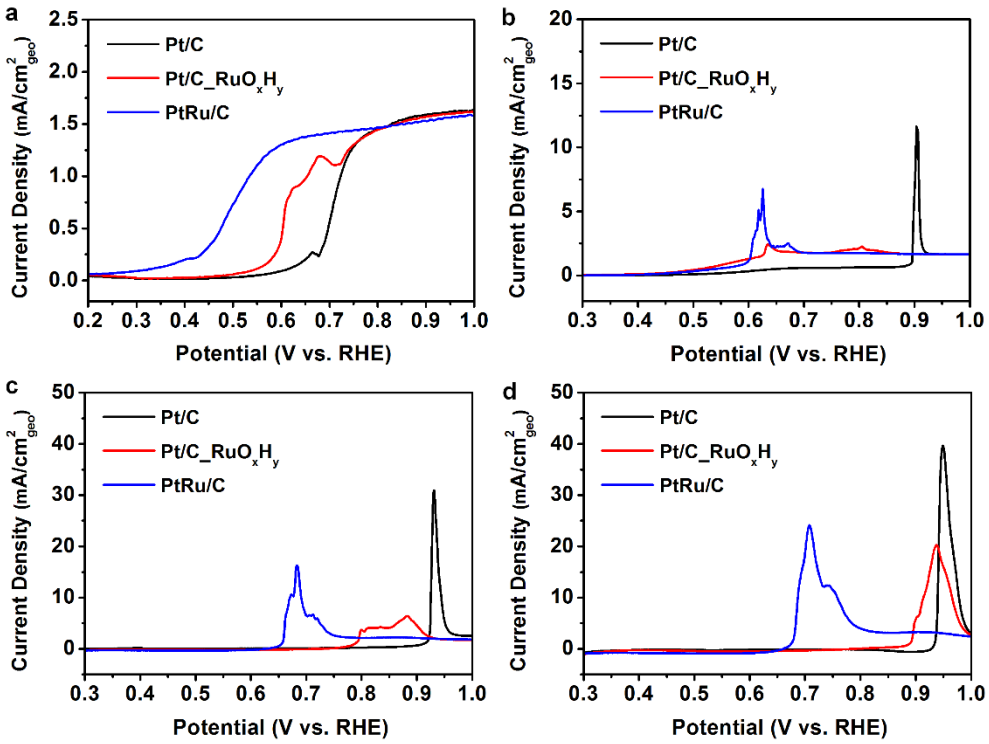


**Figure 2.10.** Background-corrected bulk CO oxidation results measured in CO saturated 0.5 M $H_2SO_4$ by (a) backward and (b-d) forward sweeps. The scan rates for the measurements were (a,b) 5 mV/s, (c) 20 mV/s, and (d) 50 mV/s.

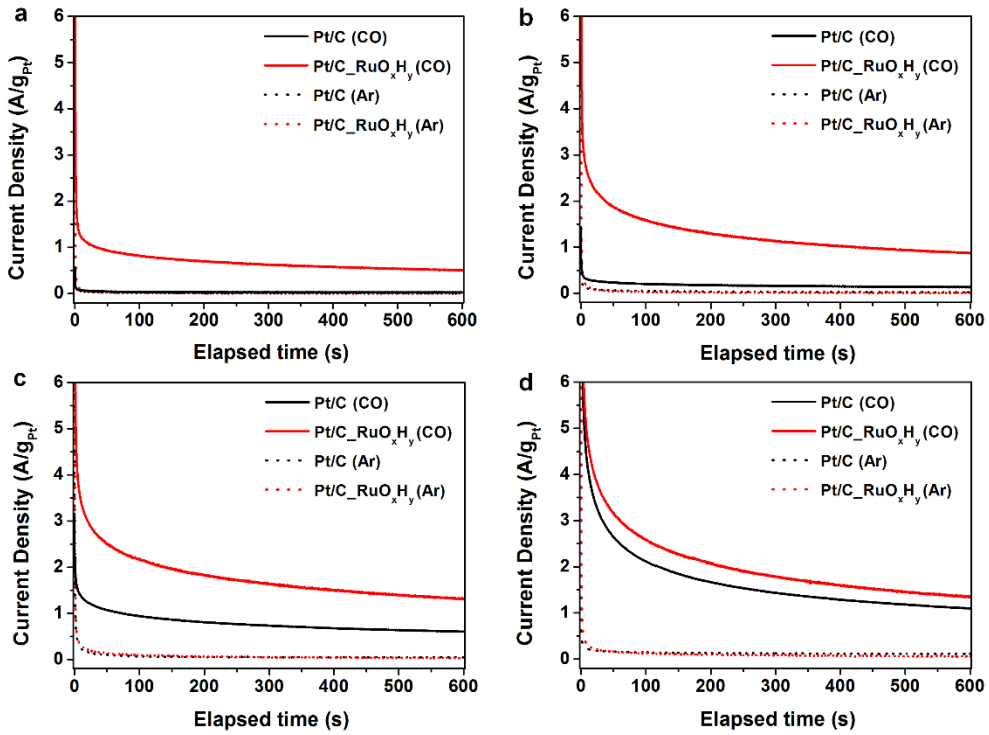


**Figure 2.11.** Time-transient bulk CO oxidation results measured at (a) 0.5 V, (b) 0.6 V, (c) 0.7 V, and (d) 0.8 V in CO saturated 0.5 M $H_2SO_4$ by using a RDE with rotation speed of 1600 rpm.

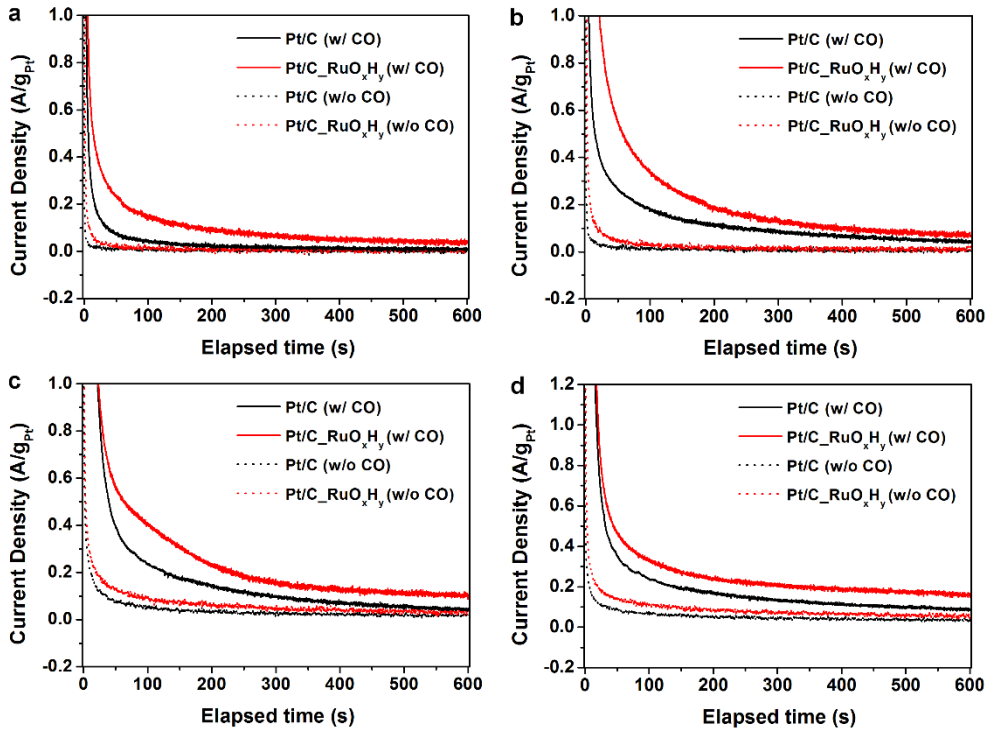


**Figure 2.12.** Time-transient CO oxidation results in the presence (solid line) / absence (dotted line) of adsorbed CO on the Pt surface. The measurements were performed at (a) 0.5 V, (b) 0.6 V, (c) 0.7 V, and (d) 0.8 V in Ar saturated 0.5 M $H_2SO_4$.

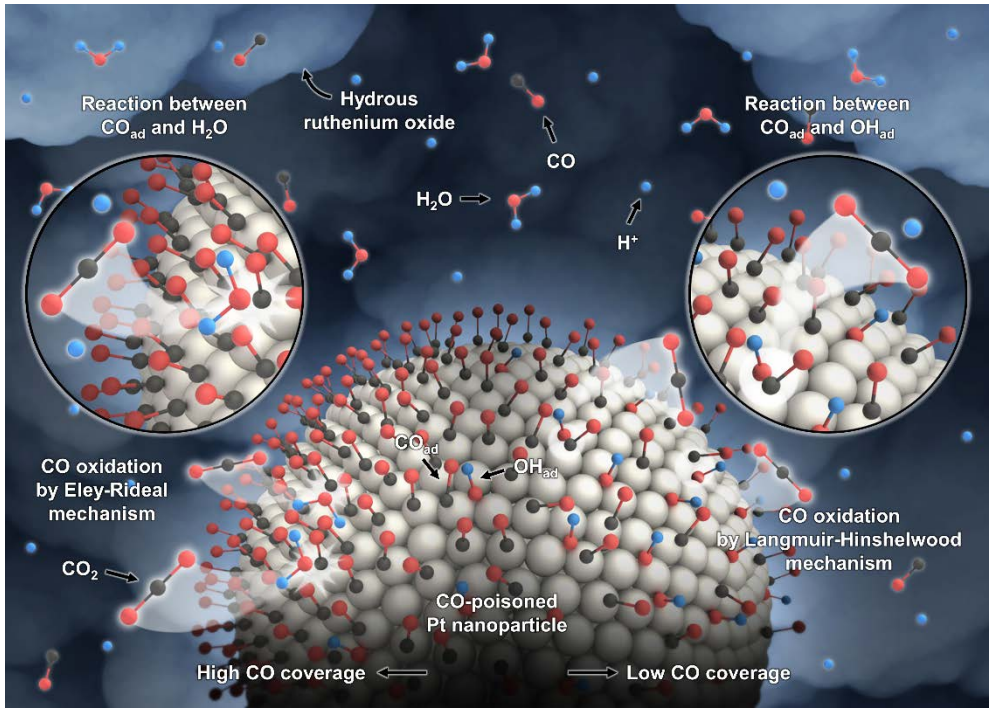


**Figure 2.13.** Schematic image showing the CO oxidation on Pt particles located in within the mixture of Pt/C catalysts and $RuO_xH_y$. CO removals by Eley-Rideal mechanism at high CO coverage and by Langmuir-Hinshelwood mechanism at low CO coverage are presented in the left and right side of the image, respectively.

### 2.3.3. Application for proton exchange membrane fuel cell

In order to investigate the influences of the bifunctional modification of blending Pt nanocatalysts with $RuO_xH_y$ on practical fuel cell devices, PEMFCs employing Pt/C_$RuO_xH_y$ catalysts were prepared. In PEMFCs, anode where reformed hydrogen gas is supplied suffers from the CO poisoning, and therefore the bifunctional effect of Pt/C_$RuO_xH_y$ was verified for HOR in the presence of trace amount of CO. Figure 2.14a shows the HOR activities measured under ultrapure $H_2$ gas feed with the oxidation currents normalized by the limiting value at 0.10 V. In fact, the HOR currents were larger in the case of Pt/C_$RuO_xH_y$ (Figure 2.15a), but this enhancement was attributed to the capacitive behavior of $RuO_xH_y$ as exhibited in the CV measurements (Figure 2.4a). Therefore, it could be concluded that the current increase is not a consequence of enhanced HOR activity. However, when trace amount of CO gas was supplied (100 ppm CO/$H_2$), decrease in the HOR current was more clearly observed in Pt/C than in Pt/C_$RuO_xH_y$, indicating that the CO removal is more efficient on Pt/C_$RuO_xH_y$ catalyst. In order to confirm the enhanced CO management in practical fuel cell applications, PEMFC single cells were prepared with Reference (Pt/C catalyst layer) or Blended (catalyst layer composed of Pt/C_$RuO_xH_y$) anodes. As shown in Figure 2.15b-15d, the performance of the Blended PEMFC is inferior to that of the Reference PEMFC in the absence of CO (ultrapure $H_2$ feed), which might be attributed to the un-optimized composition and thickness. On the other hand, when the CO/$H_2$ gas was injected into the cell, PEMFCs employing Blended anode exhibited outstanding performance compared to that with Reference anode. Around 14 times higher maximum power density and extremely larger current density were achieved by the introduction of $RuO_xH_y$, as displayed in Figure 2.14b and 2.15b – 15d.

In the case of Blended cell with CO/$H_2$ feed, there were oscillations in potentials. There are a few reports on this phenomenon, and this behavior has been understood as the results of coupled electrooxidation of $H_2$ and CO, though there is

no clear explanation yet.[66-68] According to the discussion in the previous section, CO oxidation occurs by both Langmuir-Hinshelwood and Eley-Rideal mechanism in the Blended electrode. Based on the discussion, an explanation of the oscillating behavior can be suggested as follows. As the cell operation is continued, the CO coverage on Pt surface becomes higher, and cell potential decreases to a low level. In this environment, CO can be oxidized by Eley-Rideal mechanism as observed as discussed above. This process can facilitate the rapid reactivation of the Pt nanocatalysts by enabling the formation of $OH_{ad}$ for the Langmuir-Hinshelwood CO removal. Consequently, the repeated poisoning and reactivation processes contribute to the potential maintenances up to significantly higher current densities.

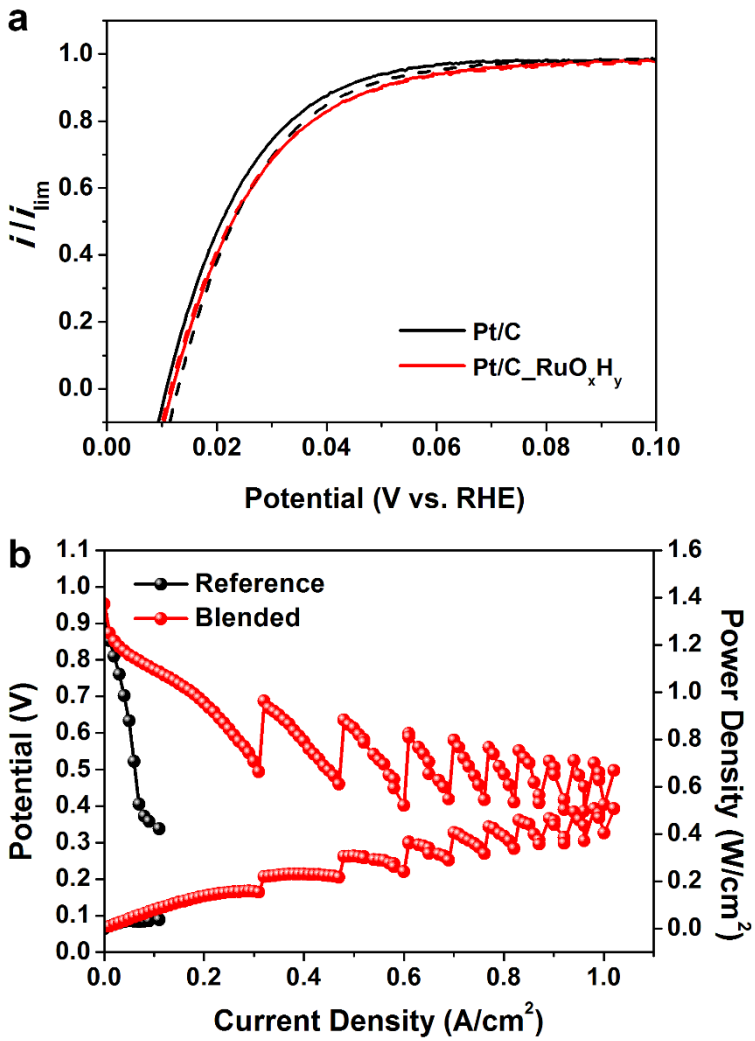


**Figure 2.14.** (a) Forward scans of hydrogen oxidation polarization curves in pure H2 (solid line) or 100 ppm $CO/H_2$ (dashed line) saturated 0.5 M $H_2SO_4$ measured by using a RDE with rotation speed of 1600 rpm. The HOR currents were normalized to the maximum current density (ilim). (b) Single cell performances of PEMFCs employing Reference and Blended anodes measured with 100 ppm $CO/H_2$ feed.

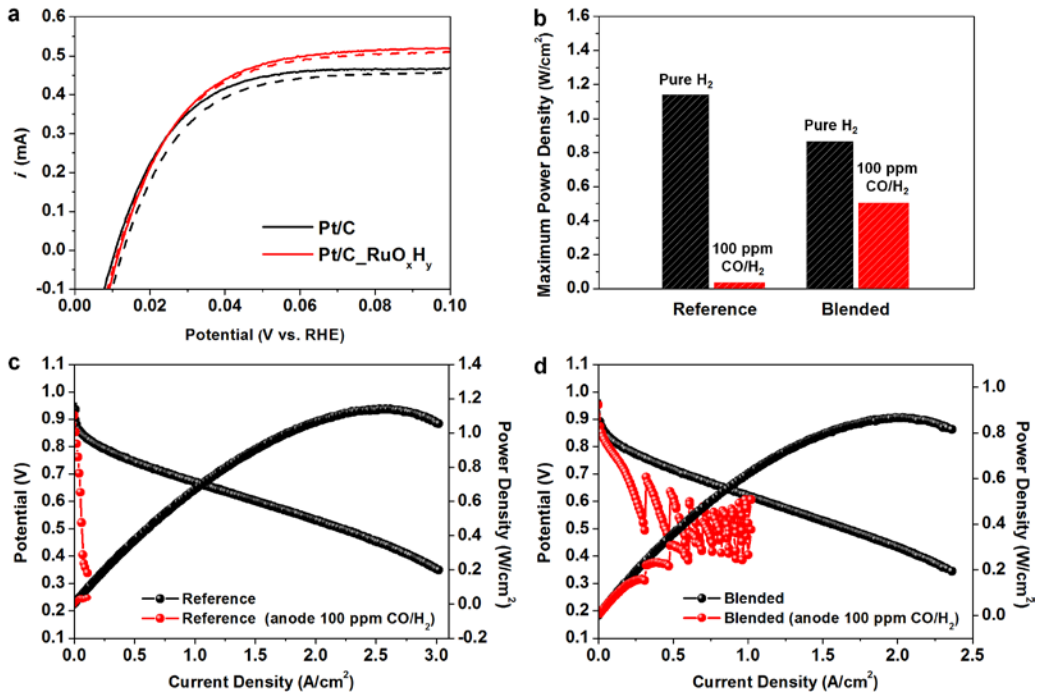


**Figure 2.15.** (a) Forward scans of hydrogen oxidation polarization curves in pure $H_2$ (solid line) or 100 ppm $CO/H_2$ (dashed line) saturated 0.5 M $H_2SO_4$ measured by using a RDE with rotation speed of 1600 rpm. (b) Comparison of maximum power densities of the single cell data displayed in (c) and (d). Single cell performances of PEMFCs employing (c) Reference and (d) Blended anodes with pure $H_2$ (black line/dots) or 100 ppm $CO/H_2$ (red line/dots) feed.

### 2.3.4. Application for direct methanol fuel cell

For further verification of the effectiveness of my approach, DMFC single cells were also prepared. CO poisoning is a critical problem in the DMFC anode where methanol oxidation reaction and generation of CO intermediate take place. For this reason, there have been numerous research works for the rapid removal of CO on the catalysts' surface, and substantial advances were achieved by PtRu alloy based materials,[23,69] and consequently PtRu bimetallic electrocatalysts are being used. In the DMFC cathode where oxygen reduction reaction (ORR) occurs, CO poisoning is also an important issue because of the CO produced by the methanol crossover and oxidation. However, there have been few reports on the CO removal in cathode. Therefore, DMFC cathodes with Pt/C or Pt/C_$RuO_xH_y$ catalyst layer were fabricated, and PtRu/C based anodes were prepared.

Figure 2.16a and 2.16b shows SEM images of MEAs prepared by spraying Pt/C (Figure 2.16a) and Pt/C_$RuO_xH_y$ (Figure 2.16b) electrocatalyst inks containing Nafion® ionomer. For proper comparisons, the amounts of Pt nanoparticles in the catalyst layers were equalized. Therefore, the thickness of catalyst coated membrane (CCM)-fabricated cathode was relatively thinner (around 20 μm), while the oxide blended structure of Pt/C and $RuO_xH_y$ had larger thickness (around 35 μm) due to the additional $RuO_xH_y$ content. Figure 2.16c shows the top-view of the Pt/C_$RuO_xH_y$ based electrode, and the corresponding elemental EDS map results for Pt and Ru shown in Figure 2.16d implies that the blending of Pt and Ru has been uniformly done even in large scale.

Figure 2.17a shows the single cell performances of DMFCs containing Pt/C or Pt/C_$RuO_xH_y$ based cathodes, and it was designated each cell as "Reference" or "Blended", respectively. Blended cathode exhibited a significant increase in current density and power density in all potential regions. The differences in maximum power density and current density at 0.5 V of the Reference and Blended cases were 10.38% and 60.40%, respectively. In order to

address the origin of this obvious enhancement in performance, analyses on ORR activity of Pt/C_$RuO_xH_y$ were first performed. Figure 2.17b shows the ORR measurement results by using rotating disk electrode (RDE) and 0.5 M $H_2SO_4$ electrolyte. As can be seen from the half-wave potentials, the difference in the ORR activities of Pt/C and Pt/C_$RuO_xH_y$ was negligible, probably due to the ORR kinetics of Pt/C and Pt/C_$RuO_xH_y$ governed by the behaviors in high potential range, where the OH coverage approaches to unity. After all, it was clear that the enhancement of the DMFC performance was not ascribed to the enhanced oxygen reduction kinetics. In addition, the ORR activity of PtRu/C was measured for comparison, and relatively poor activity was observed, as reported elsewhere, indicating that the electronic effect of PtRu/C is disadvantageous for ORR.

Since there was no significant changes in oxygen reduction performances by blending Pt nanoparticles with $RuO_xH_y$, oxidation kinetics of crossovered methanol were investigated. In general, methanol oxidation in the cathode of DMFCs is undesirable because this causes the generation of intermediate CO and the consequent CO poisoning of ORR catalysts.[42] However, there is possible advantage of higher MOR activity in cathode in terms of CO management. Though there are neither theoretical proofs nor experimental verifications explaining that the CO oxidation serves as the limiting step for the overall methanol oxidation, in most of the previous research works, MOR performance is strongly dependent on the efficient removal of CO from the catalysts' surface.[70-73] This implies that a superior MOR activity indicates a better CO oxidation kinetics, and thus there is tradeoff between methanol tolerance (low CO production) and high MOR activity (rapid CO removal). Figure 2.17c shows the methanol oxidation behaviors in the cathode of DMFC single cell, which was measured by the continuous feed of methanol solution into the anode. Unreacted methanol moved to the cathode by crossover through the Nafion® membrane, and it was oxidized by linear potential sweep from 0.0 V to 0.75 V with humidified nitrogen gas being purged into the

cathode. As can be seen from Figure S10c, by blending the Pt nanoparticles with $RuO_xH_y$, there was a significant negative shift (around 80 mV) in onset potential. Also the anodic (methanol oxidation) current density was increased to a large extent in all potential regions after the MOR onset. Considering that there is no difference between the ORR activities of Pt/C and Pt/C_$RuO_xH_y$, the superior MOR kinetic of Blended cathode seems to have larger influence on the CO management compared to the CO production by dissociation of methanol, resulting in an enhanced overall performance in DMFC devices.

To investigate the surface kinetics and mass transfer in the DMFC single cell, EIS analysis was performed. Figure 2.18a-2.18d shows the Nyquist plots measured by applying 0.40 V, 0.45 V, 0.50 V, and 0.55 V of bias to the DMFCs with Reference or Blended cathode. Comparison between the Reference and Blended DMFCs demonstrates that the overall performance of the Blended cell is superior to that of the Reference due to the charge transfer resistance at 0.50 V and 0.55 V, but this trend is reversed at 0.40 V and 0.45 V. From the DMFC single cell results shown in Figure 2.17a, it is clearly visible that the charge transfer kinetics is dominant in 0.50 – 0.55 V region, and limitation by mass transfer becomes larger on the performance at lower potentials.[47] The effect of thicker catalyst layer is sufficiently large to decrease the overall performance of the Blended DMFC to be lower than that of the Reference DMFC in the case of low (< 0.5 V) potentials.[74] Therefore, it could be confirmd again that the enhanced performance by replacement of Reference cathode with Blended electrode is mainly due to the advances in CO management, because there was no indication of enhancement by the larger thickness of catalyst layer.

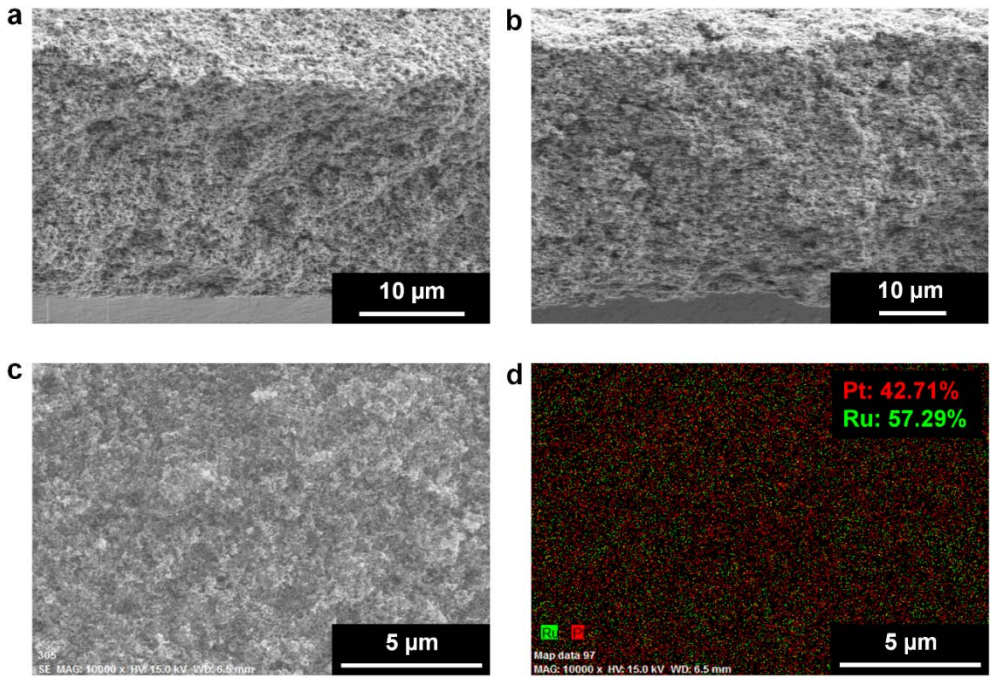


**Figure 2.16.** Cross-sectional SEM images of (a) Reference and (b) Blended catalyst layer for DMFCs. (c) Top-view SEM images of Blended catalyst layer and (d) corresponding elemental EDS maps of Pt and Ru.

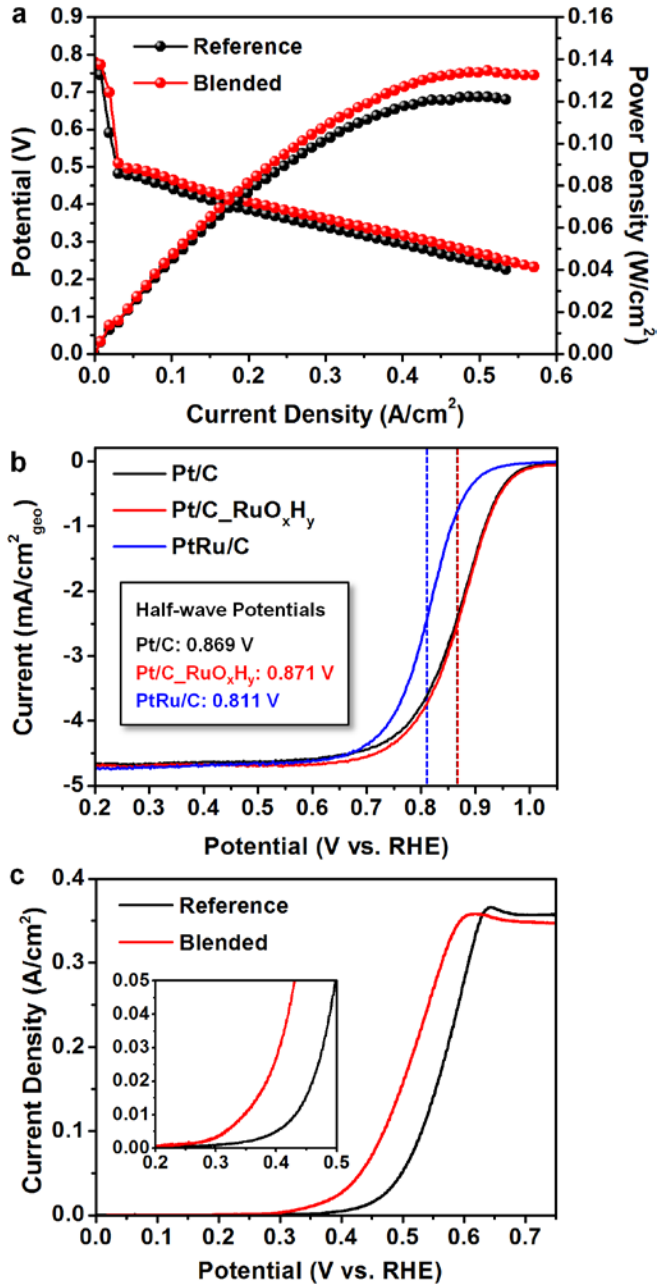


**Figure 2.17.** (a) Single cell performance results of DMFCs employing Reference and Blended cathodes. (b) Oxygen reduction currents measured by using a RDE with rotation speed of 1600 rpm. (c) Oxidation current densities of crossovered methanol with 200 ml/min $N_2$ flow into the cathode.

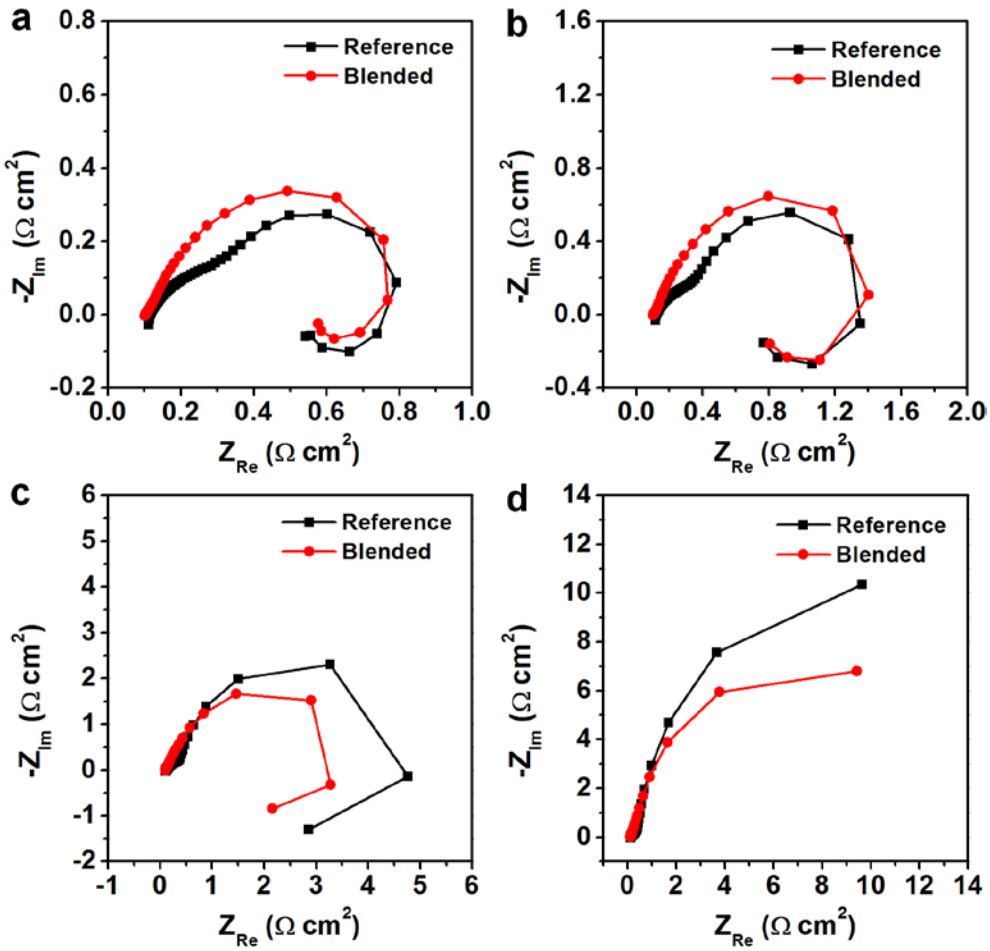


**Figure 2.18.** Nyquist diagrams of DMFCs with bias of (a) 0.40 V, (b) 0.45 V, (c) 0.50 V, and (d) 0.55 V.

## 2.4. Conclusions

In this work, CO oxidation reaction without the presence of electronic effect was investigated by designing a model system, which was composed of blended $RuO_xH_y$ with state-of-the-art Pt nanocatalysts. Absence of electronic effect was confirmed by various physicochemical analyses, and enhanced CO removal and modified CO oxidation properties by tailored oxophilicity were verified by electrochemical measurements and also by single cell analyses. Furthermore, two diverse mechanisms for CO removal (Langmuir-Hinshelwood and Eley-Rideal) were observed in the case of blended catalysts, and combination of these CO oxidation mechanisms enabled effective management especially at high CO coverage. Since this research work is the first report on the experimental investigation on the extended understanding of bifunctional effect and provides an orthogonal understanding on the removal of CO at high coverage by two diverse mechanisms, the investigations and corresponding discussion performed in this study is anticipated to give important insights for the design of catalyst layer with highly efficient CO managing properties, without the complicated synthesis of alloy catalysts.

## 2.5. References


[1] Kowal, A.; Li, M.; Shao, M.; Sasaki, K.; Vukmirovic, M. B.; Zhang, J.; Marinkovic, N. S.; Liu, P.; Frenkel, A. I.; Adzic, R. R. *Nat. Mater.* **2009**, *8*, 325-330.

[2] Chung, D. Y.; Kim, H.-i.; Chung, Y.-H.; Lee, M. J.; Yoo, S. J.; Bokare, A. D.; Choi, W.; Sung, Y.-E. *Sci. Rep*. **2014**, *4*, 7450.

[3] Kim, O.-H.; Cho, Y.-H.; Kang, S. H.; Park, H.-Y.; Kim, M.; Lim, J. W.; Chung, D. Y.; Lee, M. J.; Choe, H.; Sung, Y.-E. *Nat. Commun*. **2013**, *4*, 2473.

[4] Greeley, J.; Stephens, I. E. L.; Bondarenko, A. S.; Johansson, T. P.; Hansen, H. A.; Jaramillo, T. F.; Rossmeisl, J.; Chorkendorff, I.; Nørskov, J. K. *Nat. Chem.* **2009**, *1*, 552-556.

[5] Chen, J.; Takanabe, K.; Ohnishi, R.; Lu, D.; Okada, S.; Hatasawa, H.; Morioka, H.; Antonietti, M.; Kubota, J.; Domen, K. *Chem. Commun*. **2010**, *46*, 7492-7494.

[6] Seo, J.; Cha, D.; Takanabe, K.; Kubota, J.; Domen, K. *ACS Catal*. **2013**, *3*, 2181-2189.

[7] Zhao, D.; Xu, B.-Q. *Angew. Chem. Int. Ed*. **2006**, *45*, 4955-4959.

[8] Chen, C.; Kang, Y.; Huo, Z.; Zhu, Z.; Huang, W.; Xin, H. L.; Snyder, J. D.; Li, D.; Herron, J. A.; Mavrikakis, M. *Science* **2014**, *343*, 1339-1343.

[9] Huang, X.; Zhao, Z.; Cao, L.; Chen, Y.; Zhu, E.; Lin, Z.; Li, M.; Yan, A.; Zettl, A.; Wang, Y. M.; Duan, X.; Mueller, T.; Huang, Y. *Science* **2015**, *348*, 1230-1234.

[10] Hwang, S. J.; Kim, S.-K.; Lee, J.-G.; Lee, S.-C.; Jang, J. H.; Kim, P.; Lim, T.-H.; Sung, Y.-E.; Yoo, S. J. *J. Am. Chem. Soc*. **2012**, *134*, 19508-19511.

[11] Stamenkovic, V. R.; Fowler, B.; Mun, B. S.; Wang, G.; Ross, P. N.; Lucas, C. A.; Marković, N. M. *Science* **2007**, *315*, 493-497.

[12] Yoo, S. J.; Hwang, S. J.; Lee, J.-G.; Lee, S.-C.; Lim, T.-H.; Sung, Y.-E.; Wieckowski, A.; Kim, S.-K. *Energy Environ. Sci*. **2012**, *5*, 7521-7525.

[13] Nørskov, J. K.; Rossmeisl, J.; Logadottir, A.; Lindqvist, L.; Kitchin, J. R.; Bligaard, T.; Jónsson, H. *J. Phys. Chem. B* **2004**, *108*, 17886-17892.

[14] Urchaga, P.; Baranton, S.; Coutanceau, C.; Jerkiewicz, G. *Langmuir* **2012**, *28*, 3658-3663.

[15] Urchaga, P.; Baranton, S.; Coutanceau, C.; Jerkiewicz, G. *Langmuir* **2012**, *28*, 13094-13104.

[16] Baschuk, J. J.; Li, X. *Int. J. Energy Res.* **2001**, *25*, 695-713.

[17] García-Rodríguez, S.; Somodi, F.; Borbáth, I.; Margitfalvi, J. L.; Peña, M. A.; Fierro, J. L. G.; Rojas, S. *Appl. Catal. B* **2009**, *91*, 83-91.

[18] de la Fuente, J. L. G.; Martínez-Huerta, M. V.; Rojas, S.; Hernández-Fernández, P.; Terreros, P.; Fierro, J. L. G.; Peña, M. A. *Appl. Catal. B* **2009**, *88*, 505-514.

[19] Alayoglu, S.; Nilekar, A. U.; Mavrikakis, M.; Eichhorn, B. *Nat. Mater.* **2008**, *7*, 333-338.

[20] Hsieh, Y.-C.; Zhang, Y.; Su, D.; Volkov, V.; Si, R.; Wu, L.; Zhu, Y.; An, W.; Liu, P.; He, P.; Ye, S.; Adzic, R. R.; Wang, J. X. *Nat. Commun.* **2013**, *4*, 2466.

[21] Lee, S. J.; Mukerjee, S.; Ticianelli, E. A.; McBreen, J. *Electrochim. Acta* **1999**, *44*, 3283-3293.

[22] Mukerjee, S.; Lee, S. J.; Ticianelli, E. A.; McBreen, J.; Grgur, B. N.; Markovic, N. M.; Ross, P. N.; Giallombardo, J. R.; De Castro, E. S. *Electrochem. Solid-State Lett.* **1999**, *2*, 12-15.

[23] Petrii, O. A. *J. Solid State Electrochem.* **2008**, *12*, 609-642.

[24] Antolini, E.; Lopes, T.; Gonzalez, E. R. *J. Alloys Compd.* **2008**, *461*, 253-262.

[25] Gasteiger, H. A.; Marković, N.; Ross, P. N.; Cairns, E. J. *Electrochim. Acta* **1994**, *39*, 1825-1832.

[26] Jusys, Z.; Kaiser, J.; Behm, R. J. *Electrochim. Acta* **2002**, *47*, 3693-3706.

[27] Lu, C.; Rice, C.; Masel, R. I.; Babu, P. K.; Waszczuk, P.; Kim, H. S.; Oldfield, E.; Wieckowski, A. *J. Phys. Chem. B* **2002**, *106*, 9581-9589.

[28] Koper, M. T. M. *Surf. Sci.* **2004**, *548*, 1-3.

[29] Roth, C.; Benker, N.; Buhrmester, T.; Mazurek, M.; Loster, M.; Fuess, H.;

Koningsberger, D. C.; Ramaker, D. E. *J. Am. Chem. Soc.* **2005**, *127*, 14607-14615.

[30] Wakisaka, M.; Mitsui, S.; Hirose, Y.; Kawashima, K.; Uchida, H.; Watanabe, M. *J. Phys. Chem. B* **2006**, *110*, 23489-23496.

[31] Arenz, M.; Mayrhofer, K. J. J.; Stamenkovic, V.; Blizanac, B. B.; Tomoyuki, T.; Ross, P. N.; Markovic, N. M. *J. Am. Chem. Soc.* **2005**, *127*, 6819-6829.

[32] Ianniello, R.; Schmidt, V. M.; Stimming, U.; Stumper, J.; Wallau, A. *Electrochim. Acta* **1994**, *39*, 1863-1869.

[33] Kobayashi, T.; Babu, P. K.; Chung, J. H.; Oldfield, E.; Wieckowski, A. *J. Phys. Chem. C* **2007**, *111*, 7078-7083.

[34] Kobayashi, T.; Babu, P. K.; Gancs, L.; Chung, J. H.; Oldfield, E.; Wieckowski, A. *J. Am. Chem. Soc.* **2005**, *127*, 14164-14165.

[35] Maillard, F.; Gloaguen, F.; Hahn, F.; Léger, J.-M. *Fuel Cells* **2002**, *2*, 143-152.

[36] Marković, N. M.; Grgur, B. N.; Lucas, C. A.; Ross, P. N. *J. Phys. Chem. B* **1999**, *103*, 487-495.

[37] Marković, N. M.; Schmidt, T. J.; Grgur, B. N.; Gasteiger, H. A.; Behm, R. J.; Ross, P. N. *J. Phys. Chem. B* **1999**, *103*, 8568-8577.

[38] Wang, H.; Abruña, H. D. *J. Phys. Chem. Lett.* **2015**, *6*, 1899-1906.

[39] Wang, H.; Jusys, Z.; Behm, R. J.; Abruña, H. D. *J. Phys. Chem. C* **2012**, *116*, 11040-11053.

[40] Koper, M. T. M.; Lebedeva, N. P.; Hermse, C. G. M. *Faraday Discuss.* **2002**, *121*, 301-311.

[41] Ma, J.-H.; Feng, Y.-Y.; Yu, J.; Zhao, D.; Wang, A.-J.; Xu, B.-Q. *J. Catal.* **2010**, *275*, 34-44.

[42] Blizanac, B. B.; Pylypenko, S.; Olson, T. S.; Konopka, D.; Atanassov, P. *J. Electrochem. Soc.* **2011**, *158*, B485-B491.

[43] Jeon, M. K.; Lee, K. R.; Woo, S. I. *Langmuir* **2010**, *26*, 16529-16533.

[44] Scibioh, M. A.; Kim, S.-K.; Cho, E. A.; Lim, T.-H.; Hong, S.-A.; Ha, H. Y. *Appl. Catal. B* **2008**, *84*, 773-782.

[45] Sebastián, D.; Stassi, A.; Siracusano, S.; Vecchio, C. L.; Aricò, A. S.; Baglio, V. *J. Electrochem. Soc.* **2015**, *162*, F713-F717.

[46] Xi, J.; Wang, J.; Yu, L.; Qiu, X.; Chen, L. *Chem. Commun*. **2007**, 1656-1658.

[47] Yuan, H.; Guo, D.; Qiu, X.; Zhu, W.; Chen, L. *J. Power Sources* **2009**, *188*, 8-13.

[48] Wang, Y.; Wang, G.; Li, G.; Huang, B.; Pan, J.; Liu, Q.; Han, J.; Xiao, L.; Lu, J.; Zhuang, L. *Energy Environ. Sci.* **2015**, *8*, 177-181.

[49] Jeon, T.-Y.; Lee, K.-S.; Yoo, S. J.; Cho, Y.-H.; Kang, S. H.; Sung, Y.-E. *Langmuir* **2010**, *26*, 9123-9129.

[50] Kim, I.-H.; Kim, K.-B. *J. Electrochem. Soc.* **2006**, *153*, A383-A389.

[51] Lasch, K.; Hayn, G.; Jörissen, L.; Garche, J.; Besenhardt, O. *J. Power Sources* **2002**, *105*, 305-310.

[52] Rolison, D. R.; Hagans, P. L.; Swider, K. E.; Long, J. W. *Langmuir* **1999**, *15*, 774-779.

[53] Qiu, Z.; Huang, H.; Du, J.; Tao, X.; Xia, Y.; Feng, T.; Gan, Y.; Zhang, W. *J. Mater. Chem. A* **2014**, *2*, 8003-8008.

[54] Lee, J.; Yoo, J. M.; Ye, Y.; Mun, Y.; Lee, S.; Kim, O.-H.; Rhee, H.-W.; Lee, H. I.; Sung, Y.-E.; Lee, J. *Adv. Energy Mater.* **2015**, *5*, 1402093.

[55] Selvarani, G.; Sahu, A. K.; Kiruthika, G. V. M.; Sridhar, P.; Pitchumani, S.; Shukla, A. K. *J. Electrochem. Soc.* **2009**, *156*, B118-B125.

[56] Ruan, M.; Sun, X.; Zhang, Y.; Xu, W. *ACS Catal.* **2015**, *5*, 233-240.

[57] Feliu, J. M.; Orts, J. M.; Gómez, R.; Aldaz, A.; Clavilier, J. *J. Electroanal. Chem.* **1994**, *372*, 265−268.

[58] Akemann, W.; Friedrich, K. A.; Stimming, U. *J. Chem. Phys.* **2000**, *113*, 6864−6874.

[59] Samjeské, G.; Komatsu, K.-i.; Osawa, M. *J. Phys. Chem. C* **2009**, *113*, 10222−10228.

[60] Housmans, T. H. M.; Hermse, C. G. M.; Koper, M. T. M. *J. Electroanal. Chem.*

**2007**, *607*, 69−82.

[61] Lee, K.-S.; Park, H.-Y.; Ham, H. C.; Yoo, S. J.; Kim, H. J.; Cho, E.; Manthiram, A.; Jang, J. H. *J. Phys. Chem. C* **2013**, *117*, 9164-9170.

[62] Tuckerman, M. E.; Chandra, A.; Marx, D. Acc. *Chem. Res.* **2006**, *39*, 151-158.

[63] Mohammed, O. F.; Pines, D.; Pines, E.; Nibbering, E. T. *J. Chem. Phys.* **2007**, *341*, 240-257.

[64] Erdey-Gruz, T. *Transport Phenomena in Electrolyte Solutions*; Adam Higler: London, **1974**.

[65] Kornyshev, A. A.; Kuznetsov, A. M.; Spohr, E.; Ulstrup, J. *J. Phys. Chem. B* **2003**, *107*, 3351-3366

[66] Rohland, B.; Plzak, V. *J. Power Sources* **1999**, *84*, 183-186.

[67] Zhang, J.; Datta, R. *J. Electrochem. Soc*. **2002**, *149*, A1423-A1431.

[68] Zhang, J.; Fehribach, J. D.; Datta, R. *J. Electrochem. Soc.* **2004**, *151*, A689-A697.

[69] Pedersen, C. M.; Escudero-Escribano, M.; Velázquez-Palenzuela, A.; Christensen, L. H.; Chorkendorff, I.; Stephens, I. E. L. *Electrochim. Acta* **2015**, *179*, 647-657.

[70] Mancharan, R.; Goodenough, J. B. *J. Mater. Chem.* **1992**, *2*, 875-887.

[71] Zeng, J.; Yang, J.; Lee, J. Y.; Zhou, W. *J. Phys. Chem. B* **2006**, *110*, 24606-24611.

[72] Lee, K.-S.; Jeon, T.-Y.; Yoo, S. J.; Park, I.-S.; Cho, Y.-H.; Kang, S. H.; Choi, K. H.; Sung, Y.-E. *Appl. Catal. B: Environ.* **2011**, *102*, 334-342.

[73] Lee, K.-S.; Park, I.-S.; Park, H.-Y.; Jeon, T.-Y.; Cho, Y.-H.; Sung, Y.-E. *J. Electrochem. Soc.* **2009**, *156*, B1150-B1155.

[74] Matar, S.; Liu, H. *Electrochim. Acta* **2010**, *56*, 600-606.

# Chapter 3. Studies on oxophilic effect in platinum nanocatalyst for electrocatalysis in acidic medium

## 3.1. Introduction

Proton exchange membrane fuel cell (PEMFC) is a highly efficient energy-conversion device which generates electricity using hydrogen and oxygen as reactants. In the device, proton is conducted through polymer electrolyte in order to form closed circuit and reactions ($H_{2\,(g)} \rightarrow 2H^{+}_{\,(aq)} + 2\,e^{-}$ and $1/2O_{2\,(g)} + 2H^{+} + 2e^{-} \rightarrow H_2O_{\,(l)}$ for anode and cathode, respectively) occur at the electrodes of PEMFC.[1-4] Meanwhile, proton exchange membrane (PEM) electrolyzer is clean hydrogen-production device and operated by inverse reaction ($H_2O_{\,(l)} \rightarrow 1/2O_{2\,(g)} + 2H^{+}_{\,(aq)} + 2e^{-}$ and $2H^{+}_{\,(aq)} + 2e^{-} \rightarrow H_{2\,(g)}$ for anode and cathode, respectively) of PEMFC by power supply.[5-8] PEMFC has shown vastly superior performance to the fuel cell based on the membrane which conducts hydroxyl ion and the trend has also corresponded to that of the electrochemical water-splitting devices.[8-10]

In addition, the performance of these cells are strongly influenced by reaction kinetics at each electrode, and thus developments of PEMFC and PEM electrolyzer have been achieved along with developments of highly efficient electrocatalysts in the electrodes.[11-14] Most representative electrocatalysts in PEMFC are platinum (Pt) nanocatalyst on carbon support and Pt-metal alloy catalysts. These electrocatalysts have been consistently and fundamentally studied in many previous reports.[15-20] In general, the reason for enhancement of Pt catalyst by alloying with second metal species is explained by strain effect, ligand effect, and geometric effect on Pt surface.[21-23] These effects commonly adjust adsorption energies of reaction intermediates on Pt site. However, these adsorption energies

are scaled with each other, and thus selective tuning on adsorption energy of one type of intermediates is impossible.[24,25] For this reason, activity trends of electrocatalysts show volcano shape that has maximized electrocatalytic activity where it has optimum adsorption energy and the shape has been confirmed by many experiments and theoretical calculations.[1,2,26,27] From this view, since the effects induced from metal alloy are in line with tuning the adsorption energy, these approaches are regarded as a kind of effort of moving the activity 'along' the ridge of the volcano.

However, there is one more effect for Pt-metal alloy, which is called as bifunctional effect generally interchanged with the term of oxophilic effect. In general, bifunctional effect indicates functions of different kinds of two sites for one reaction. More specifically, the effect is understood as an interaction between oxygen species on second metal and adsorbed species on Pt in the vicinity of the second metal.[28-30] The effect of increasing oxphilicity on Pt surface is expected to bring enhanced activity escaping from volcano-like trend and has been mainly observed in methanol oxidation reaction, carbon monoxide (CO) oxidation in both acid and alkaline media and hydrogen oxidation/evolution in alkaline electrolyte. However, bifunctional effect and the other effects usually work together in the electrocatalytic system and it is hard to obtain separated understanding on bifunctional effect in the real electrochemical system, and thus there have been a few efforts to address the influences of these effects.[31-35] Masel and Wieckowski group performed temperature programmed desorption technique using ruthenium (Ru)-decorated Pt surface and measured 4 times larger bifunctional effect than other electronic effects.[34] In addition, Jeon et al. reported enhanced bifunctional effect when heat treatment induces segregation of Pt in PtRu/C for methanol oxidation.[35] These researches exhibited possibilities of additional tuning the activity of Pt catalyst by oxophilic behavior. More importantly, there are critical works on bifunctional effect progressively performed by N. Markovic's group.[36,37]

In 2012, they observed bifunctional effect of electrochemically deposited Ni, Co, Fe, Mn hydroxide/oxyhydroxide on Pt (111) substrate in an alkaline electrolyte. These materials could reduce more overpotential of electrochemical production of hydrogen and CO oxidation, more metal (Ni, Co, Fe and Mn)-oxygen binding strength was reduced. It indicated that the metal-oxygen binding strength was correlated with activity of oxygen evolution reaction (OER) in alkaline electrolyte. Therefore, it could be concluded that bifunctional effect and tuning of oxophilicity worked on Pt substrate have a definite interrelationship with water dissociation activity and oxygen evolution activity in alkaline media.

Until recently, Ir oxide received great attention due to its highly active and stable characteristics in electrocatalytic OER, and the degree of crystallinity has been understood as one of the most important factors governing the OER performance of iridium oxide.[38,39] Based on these results, amorphous ruthenium oxide hydrate and amorphous iridium oxide hydrate were thermally annealed at various temperatures, and hydrous Ru and Ir oxide catalysts with different OER activities in an acidic electrolyte was obtained. By physicochemical comparisons between the hydrous oxide catalysts, it was verified that there is a new descriptor for OER activity in acid. In addition, as a continuation of the investigations on bifunctional effect in acidic media, blended catalysts were prepared by uniformly mixing Pt/C and oxide hydrate catalysts with different activities in OER. Based on the CO oxidation in this set of blended catalysts, a linear correlation between OER activity of hydrous oxide catalysts and CO oxidation performance in blended catalysts was verified in acid electrolyte. Based on this observation and various model experiments in CO oxidation, long-range water activation by exchanges between O-H and hydrogen bond in chains of water molecules is suggested in this chapter.

## 3.2. Experimental section

### 3.2.1. Preparation of electrocatalysts

For the electrochemical and physicochemical analyses, ruthenium (IV) oxide hydrate (99.9% $RuO_xH_y$, Sigma-Aldrich) and iridium (IV) oxide dihydrate (99.99% $IrO_xH_y$, Alfa Aesar) were annealed by box-furnace at 100 °C, 200 °C, 300 °C, 400 °C, and 500 °C for 2 hrs. These oxides were mixed with 5 wt% Nafion® ionomer (Sigma-Aldrich, added as a binder) and isopropanol (Sigma-Aldrich), and subsequently stirred and under ultrasonication for ink preparation of electrochemical characterization. In addition, blended catalyst inks were prepared by mixing Pt/C (20 wt%, 40 wt%, and 60 wt% of equivalent Pt weight, Johnson Matthey), 5 wt% Nafion® ionomer (Sigma-Aldrich, added as a binder), isopropanol (Sigma-Aldrich) and as-received oxide hydrate or the annealed oxide. As a control sample, conventional catalyst ink composed of Pt/C, Nafion® ionomer and IPA was also prepared. After vigorous stirring and sonication, 3 μL of catalyst ink was dropped onto a glassy carbon substrate (geometric surface area: 0.196 $cm^2$).

### 3.2.2. Physical characterizations

In order to examine change of weight and water content of the as-received oxide hydrates during annealing process, thermogravimetric analysis was conducted using TA Instruments Q-5000 IR model with a heating rate of 10 °C/min in air. The morphologies of as-received oxide hydrates and annealed oxides were characterized by transmission electron microscopy (FEI Tecnai F20 used), and the structures of blended catalysts were also characterized by transmission electron microscopy (TEM; JEOL JEM 2100 used) equipped with an energy dispersive spectroscopy (EDS) accessary. The crystalline structure of the oxide materials were analyzed using high resolution powder diffraction (HRPD) measured at the 9B

beamline of Pohang Accelerator Laboratory (PAL). The incident beam was vertically collimated using a mirror and monochromatized to a wavelength of 1.5179 Å using a double-crystal Si (111) monochromator. X-ray spectroscopy (XAS) of Ru and Ir oxides were performed in fluorescence mode at 8C beamline of PAL. The beam was monochromatized with Si (111) monochromator, and the intensity was detuned by 20% in order to inhibit undesirable higher harmonics. The spectra were processed using Athena software of the IFEFFIT package. The core level X-ray photoelectron spectroscopy (XPS) spectra and near edge X-ray absorption fine structures (NEXAFSs) of as-received oxide hydrates and annealed oxides were recorded by 8A1 beamline of PAL (U7-undulator radiation), and the results were analyzed by using XPSPEAK41 and Athena software, repectively. In addition, Pt 4f electronic structures of the blended catalysts were examined by XPS (KRATOS AXIS-His, Al Kα radiation source).

### 3.2.3. Electrochemical measurements

Electrochemical measurements were carried out by using a potentiostat (PGSTAT101, Autolab) based on a conventional three-electrode electrochemical cell comprising a glassy carbon (working electrode), a platinum wire (counter electrode), and a saturated calomel reference electrode. Oxygen evolution polarization curves were measured in an electrochemical cell within the potential range of 1.0−1.8 V vs. reversible hydrogen electrode (RHE) with the scan rate of 10 mV/s and rotation at 1600 rpm. 0.5 M $H_2SO_4$ was used as an electrolyte, and $O_2$ was continuously purged into the solution during the measurement. For the CO stripping analyses (monolayer CO oxidation), CO molecules were pre-adsorbed (chemisorption) on the surface of catalysts at 0.05 V vs. RHE by injecting 99% CO gas for 15 min followed by the removal of CO gas dissolved in the electrolyte by 30 min of Ar purging. CO stripping voltammetry was performed in 0.5 M $H_2SO_4$ in potential range of 0.05−1.05 V vs. RHE. For CO bulk oxidation measurments,

same measurement condition was applied with exceptions of scan rate which varied (5 mV/s, 20 mV/s, and 50 mV/s), continuous CO gas feeds, and rotation at 1600 rpm. In order to check the effect of anion adsorption and proton concentration, 0.01, 0.05, and 0.1 M $HClO_4$ were additionally used as electrolytes for CO bulk oxidation. All electrochemical measurements were performed at 20 °C which was controlled by a thermostat and a circulating jacket.

## 3.3. Results and discussion

### 3.3.1. Basic physicochemical characterizations of ruthenium oxides and iridium oxides

In order to investigate the degree of hydration in hydrous Ru and Ir oxides, thermal gravimetric analysis (TGA) was performed, and Figure 3.1 shows the TGA results of $RuO_xH_y$ and $IrO_xH_y$ measured in air at a heating rate of 10 K/min. It is clearly observable from the TGA data that the mass of the oxide hydrates decreases as the temperature increases, and this indicates the removal of water from the hydrous oxides. Since saturating behaviors of mass profile were apparent at the temperature higher than 900 K, we calculated the degree of hydration based on the assumption that the dehydration of oxide hydrates are complete at 1000 K. Table 3.1 shows the number of water molecules per $RuO_2$ or $IrO_2$ at various annealing temperatures, which was initially around 2 in both $RuO_xH_y$ and $IrO_xH_y$ and exhibited gradual drop as the temperature was increased. Meanwhile, steep decreases in weights of hydrous oxides, which seem to be ascribable to the fast removal of water by rapid growth of oxide crystals, were observed at around 250 °C and 400 °C in the cases of $RuO_xH_y$ and $IrO_xH_y$, respectively. The hydrous oxides after the heat treatments were abbreviated as depicted in Table 1; for example, $RuO_xH_y$ after the thermal annealing at 200 °C was noted as $RuO_xH_y$_200.

Figure 3.2 and Figure 3.3 show the TEM images of $RuO_xH_y$ and $IrO_xH_y$ that were thermally annealed at various temperatures (100 to 500 °C), respectively.

Both of the hydrous oxides had disordered nanostructures in pristine states, and gradual changes in morphologies were observable as a consequence of crystallization in elevated temperatures. In the case of $RuO_xH_y$, formations of crystallites led to the nanoporous structures followed by growth of particles sizes in higher temperatures, $IrO_xH_y$ manifested a substantial increase in crystallinity from 400 °C while the changes in overall morphologies were not significant.[40]

In order to investigate the effect of heat treatment on the crystalline properties of Ru and Ir oxide hydrates, synchrotron-based high-resolution powder diffraction (HRPD) measurements were performed. As can be seen from the HRPD patterns displayed in Figures 3.4a and 3.4b, amorphous $RuO_xH_y$ and $IrO_xH_y$ gradually turned into crystalline $RuO_2$ and $IrO_2$, respectively. Meanwhile, $IrO_xH_y$ showed minor reflection of metallic phase (JCPDS 06-0598). The presence of metallic Ir in the same commercial $IrO_xH_y$ was previously reported by Schlögl and his co-workers,[38,39] and the presence of thick oxide on the surface of the metallic contaminants was verified by keen XPS analysis. In addition, the quantity of Ir obtained by Rietveld refinement was negligibly small (2.4 wt%). Therefore, the effect of metallic Ir in the $IrO_xH_y$ electrocatalysis was considered unimportant throughout this study.

X-ray absorption fine structure (XAFS) analyses were performed for further understanding of the changes in $RuO_xH_y$ and $IrO_xH_y$ induced by thermal annealing. Figures 3.4c and 3.4d show the k3-weighted Fourier transform of extended X-ray absorption fine structure (EXAFS) data for the oxide hydrates. Structural ordering by increased crystallinity was clear from the signals at large R induced by interactions at far distances. It was noteworthy to observe that the signals from interactions in a significantly long range (R larger than around 4 Å) were apparent from 300 °C and 400 °C in the cases of $RuO_xH_y$ and $IrO_xH_y$, respectively. These results well match with the temperatures responsible for rapid water removal which are discussed in TGA analysis, implying that the crystal

growth in $RuO_xH_y$ and $IrO_xH_y$ are accelerated beyond those temperatures (250 °C for $RuO_xH_y$ and 400 °C for $IrO_xH_y$). Meanwhile, though the crystalline properties of $RuO_xH_y$ and $IrO_xH_y$ show vigorous changes during the thermal annealing, the oxidation state of Ru and Ir did not show any change during the heat treatment, as can be seen from the X-ray absorption near edge structure (XANES) data displayed in Figure 3.5. From this observation, we could conclude that Ru and Ir in pristine oxide hydrates exist as $RuO_2$ and $IrO_2$, respectively, without having electronic interaction with the $H_2O$ molecules that are present in hydrated state.[41-42]

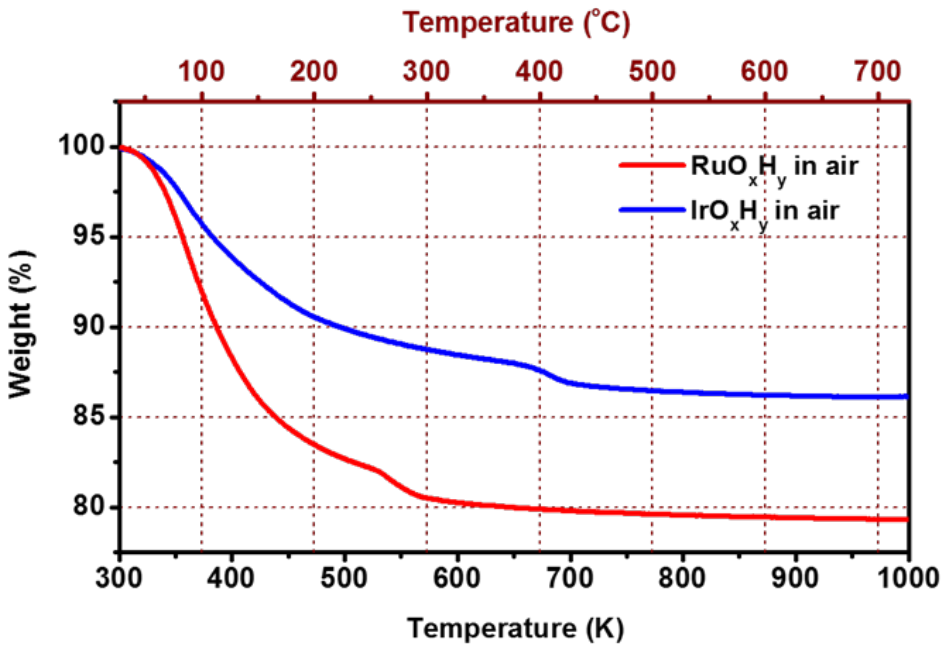


**Figure 3.1.** Thermal gravimetric analysis (TGA) results of $RuO_xH_y$ and $IrO_xH_y$ in air measured at a heating rate of 10 K/min.

| | $RuO_xH_y$ | $IrO_xH_y$ |
|---|---|---|
| ASP | $RuO_2*1.93H_2O$ | $IrO_2*2.00H_2O$ |
| 100 ℃ | $RuO_2*1.18H_2O$ | $IrO_2*1.37H_2O$ |
| 200 ℃ | $RuO_2*0.39H_2O$ | $IrO_2*0.63H_2O$ |
| 300 ℃ | $RuO_2*0.11H_2O$ | $IrO_2*0.37H_2O$ |
| 400 ℃ | $RuO_2*0.06H_2O$ | $IrO_2*0.21H_2O$ |
| 500 ℃ | $RuO_2*0.03H_2O$ | $IrO_2*0.04H_2O$ |

**Table 3.1.** Degree of hydration in hydrous Ru and Ir oxides.

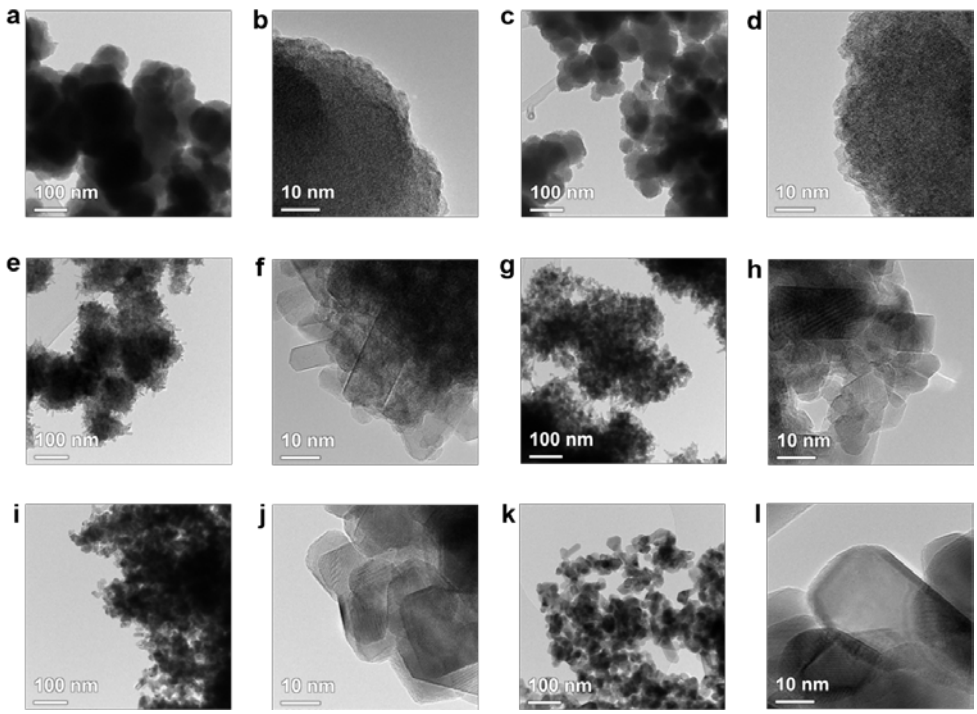


**Figure 3.2.** Transmission electron microscopy (TEM) images of (a,b) $RuO_xH_y$, (c,d) $RuO_xH_y$_100, (e,f) $RuO_xH_y$_200, (g,h) $RuO_xH_y$_300, (i,j) $RuO_xH_y$_400, and (k,l) $RuO_xH_y$_500.

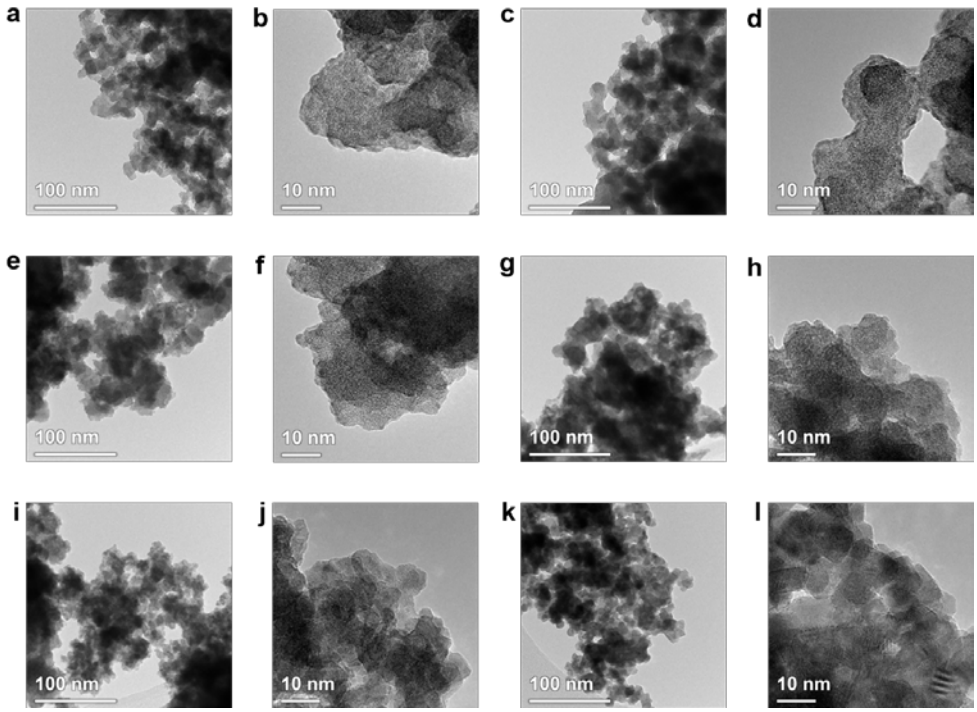


**Figure 3.3.** Transmission electron microscopy (TEM) images of (a,b) $IrO_xH_y$, (c,d) $IrO_xH_y$_100, (e,f) $IrO_xH_y$_200, (g,h) $IrO_xH_y$_300, (i,j) $IrO_xH_y$_400, and (k,l) $IrO_xH_y$_500.

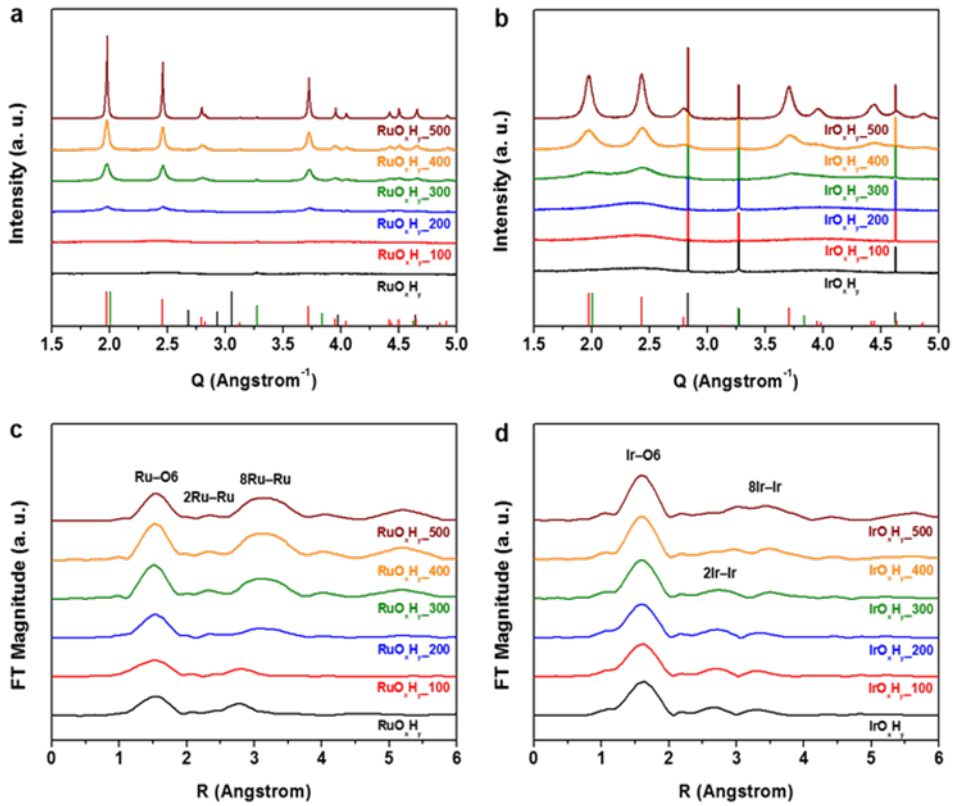


**Figure 3.4.** (a,b) High-resolution powder diffraction (HRPD) patterns for (a) hydrous Ru oxides and (b) hydrous Ir oxides. (c,d) k3-weighted Fourier transforms of extended X-ray absorption fine structure (EXAFS) data for (c) hydrous Ru oxides and (d) hydrous Ir oxides.

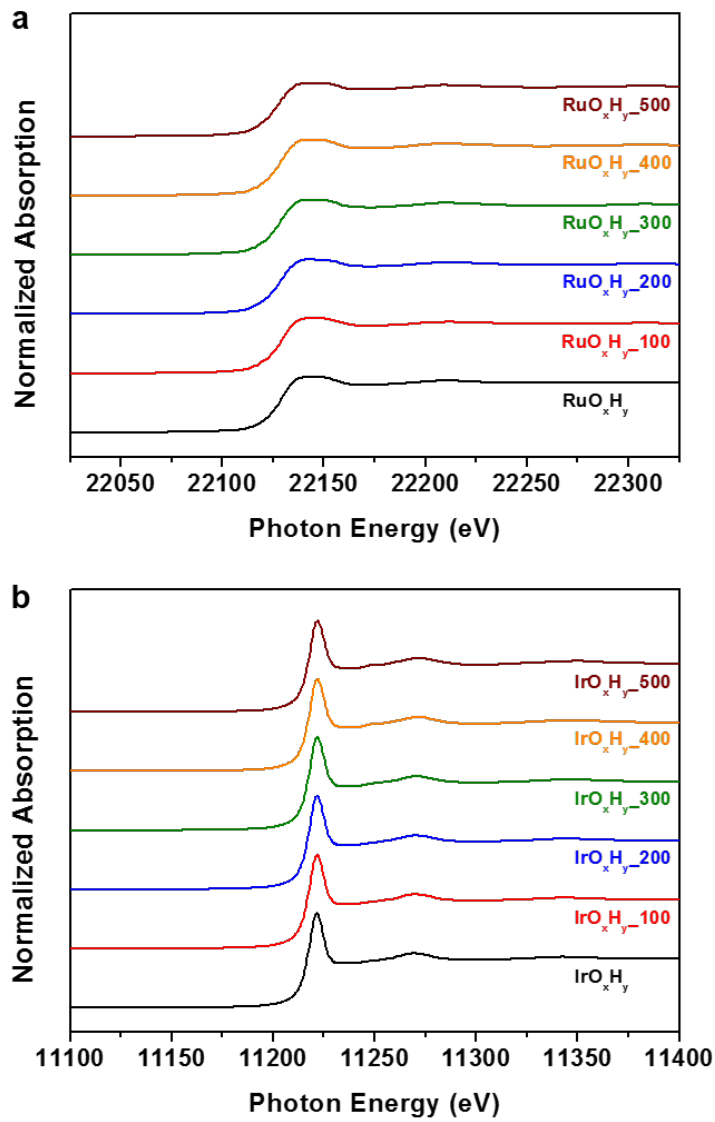


**Figure 3.5.** X-ray absorption near edge structure (XANES) spectra for (a) hydrous Ru oxides and (b) hydrous Ir oxides.

### 3.3.2. Oxygen evolution reaction in acidic medium

Figures 3.6a and 3.6b shows oxygen evolution reaction (OER) polarization curves of oxide hydrates before and after the heat treatments at various temperatures. The electrochemical measurements were performed in 0.5 M $H_2SO_4$ solution using a rotating disk electrode (RDE) in order to suppress the accumulation of $O_2$ bubbles on the surface. In general, ruthenium oxide and iridium oxide have been regarded as the most active OER catalysts in acidic media, and low crystallinity is known to be beneficial to achieve a high performance.[38,39,43] In terms of catalytic activity, $RuO_2$ is more favorable for OER compared to $IrO_2$, but Ru oxide suffers from poor stability that leads to severe dissolution of catalysts during the OER operation at high potential, and Ir oxide is thereby considered as state-of-the-art electrocatalyst for OER.[44,45] These experimental results were in line with the previous observations, that pristine $RuO_xH_y$ and $RuO_xH_y$_100 went through a severe degradation in first potential sweep (see Figure 3.7) and completely lost the activity (Figure 3.6a), though $IrO_xH_y$ exhibited a decent OER performance (Figure 3.6b). However, after the heat treatments at 200 °C and higher temperatures, $RuO_xH_y$ was stabilized and manifested excellent OER activity, even surpassing the performance of Ir oxide catalysts. For quantitative comparisons between the OER performances of the hydrous oxide catalysts, overpotential values at 10 mA/cm$^2$ were obtained from the OER polarization curves, and the results are displayed in Table 3.2. In both cases of $RuO_xH_y$ and $IrO_xH_y$, further increase in the thermal annealing temperature from the stabilized states resulted in the drops in catalytic activities.

In order to investigate OER mechanism of the catalysts, Tafel slopes of the OER catalysts were calculated from linear fitting by Tafel equation ($\eta = b \log(j) + a$) as depicted in Figures 3.6c and 3.6d. Elemental steps for OER in acidic media are known as follows:[46]

$$\text{(a) } S + H_2O \rightarrow S\text{-}OH^* + H^+ + e^- \quad (120\ mV)$$

(a') S-OH* → S-OH (60 mV)

(b) S-OH → S-O + $H^+$ + $e^-$ (40 mV)

(b') S-OH + S-OH → S-O + $H_2O$ (40 mV)

(c) S-O + S-O → 2S + $O_2$ (30 mV)

wherein S indicates a surface active site. (a) is water-dissociation step on the active site, and (a') is rearrangement of intermediate OH via surface reaction. (b) and (b') are parallel steps that occur with the dependence on the adsorption strength of the intermediate, and (c) is typical recombination step of adsorbed O. Tafel slopes are governed by the rate-determining step (RDS), and the slopes corresponding to the elemental steps are displayed next to the reaction steps above. As can be seen from Figures 3.6c and 3.6d, Tafel slopes of the hydrous oxides were over 60 mV/dec except for the $RuO_xH_y$_200. The Tafel slope over 60 mV indicates that the OER activities of $RuO_xH_y$ and $IrO_xH_y$ are dependent on water dissociation (step (a)) and OH formation on surface active site (step (a')). However, $RuO_xH_y$_200 exhibited a Tafel slope of 46.4 mV/dec, implying that water dissociation and OH rearrangement are relatively fast and not rate limiting, the second electron transfer step ((b) or (b')) being the RDS. This result clearly shows that $RuO_xH_y$_200 is highly efficient for water dissociation and thereby qualifies itself as an excellent electrocatalyst for OER in acidic media.

Another noteworthy observation was that the OER activity of $RuO_xH_y$_200 was not only the highest among the hydrous oxides but also comparable to the recently reported state-of-the-art electrocatalysts that were elaborately designed by various theoretical and technical backgrounds. The comparisons of current densities at a specific overpotential (250 mV) and Tafel slope between the $RuO_xH_y$_200 and the best-performing catalysts in the previous literatures are summarized in Table 3.3.[12,40,47,48] It was clear from the comparative investigations that the $RuO_xH_y$_200 shows one of the highest activities in OER,

even though the catalysts were prepared by simple thermal annealing process in air atmosphere. In order to figure out the stability of $RuO_xH_y$_200, we performed cyclic voltammetry in an OER operation potential region, and the 100 scan results are displayed in Figure 3.8. From the decent stability observable from the long-term potential scans, which is a strikingly high durability in Ru oxide catalysts, it could be concluded that heat treatment approach leading to a partial dehydration and moderated crystallinity is an effective way to tailor both the activity and stability of the Ru oxides.

Since the oxide hydrates show clear differences in activities for OER in acidic medium, further investigations for the understanding of the activity trends in OER were performed by various X-ray techniques. Figures 3.9 shows the synchrotron X-ray photoelectron spectroscopy (XPS) results obtained at Ru 3p and Ir 4f, and the XPS O 1s spectra of Ru and Ir oxide hydrates are displayed in Figure 3.10 and Figure 3.11, respectively. The O 1s signals were deconvoluted into three peaks according to the previous study:[49,50] O1 at around 530 eV from O atoms bound to metals, O2 at around 531.5 eV from defective (low-coordinated) O atoms, and O3 at around 533 eV associated with hydroxyl groups or surface-adsorbed oxygen species (i.e. $O_2$ and $H_2O$). Areal ratios of O1, O2, and O3 of Ru and Ir oxide hydrates are summarized in Table 3.4 and Table 3.5, respectively. As the thermal annealing temperature was increased, portion of O1 became larger in both Ru and Ir oxide hydrates, as a consequence of the enhanced crystallinity. Meanwhile, it was notable that O2 manifested different tendencies in $RuO_xH_y$ and $IrO_xH_y$. In the case of Ru oxide, O2 was increased from pristine $RuO_xH_y$ to $RuO_xH_y$_100, but sharp decrease was observed in $RuO_xH_y$_200, and then the portion of O2 grew larger again as the temperature was elevated from 200 to 500 °C. In addition, it was notable that an exactly opposite tendency was observable in O3 of Ru oxides. The portion of O3 decreased from $RuO_xH_y$ to $RuO_xH_y$_100, increased at $RuO_xH_y$_200, and then gradually decreased at higher

annealing temperature. Peculiarly low level of O2 (defective O) and high level of O3 (hydroxyl groups or adsorbed oxygen species) in $RuO_xH_y$_200 seems to be related to the initiation of crystallization which led to the formation of small crystallites and consequent increase in the amount of hydroxyl groups on the surface. Nevertheless, Ru oxide catalysts that are sufficiently stabilized for OER operation (thermally annealed at 200 – 500 °C) exhibited clear tendency. In the case of Ir oxides, contrary to Ru oxides, the portion of O2 showed gradual decrease followed by saturation at around 45% as the annealing temperature was increased. However, O3 showed same tendency as in the case of Ru oxides, of which relative content became smaller in the elevated temperatures.

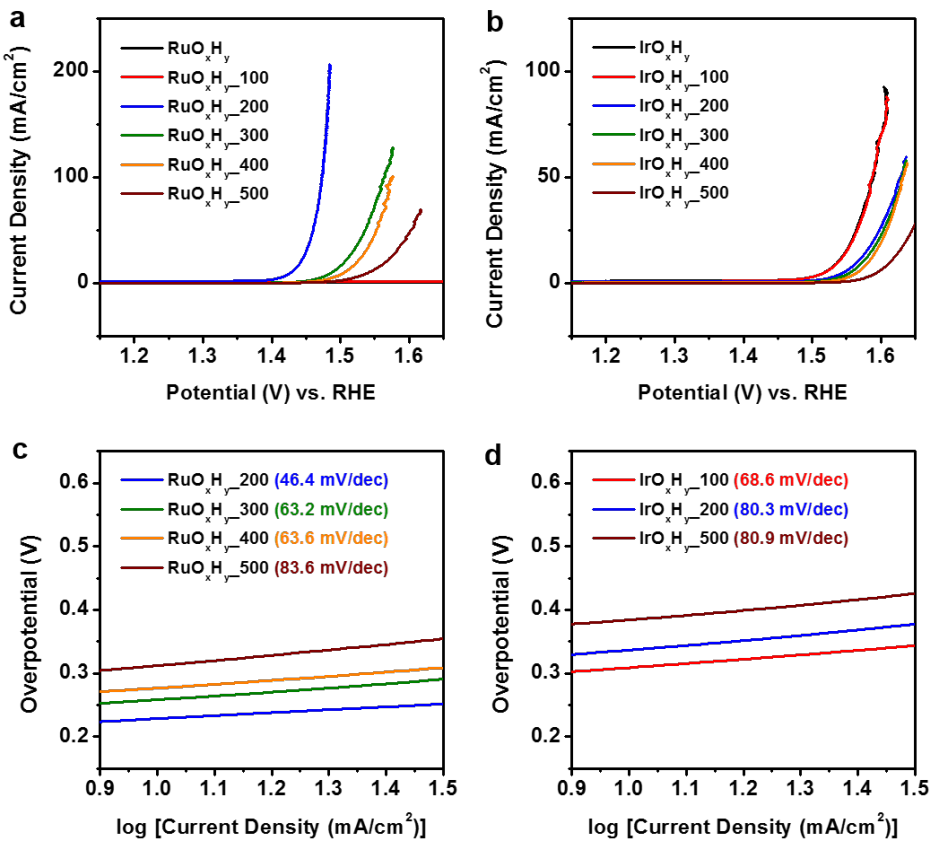


**Figure 3.6.** (a,b) iR-corrected oxygen evolution reaction (OER) polarization curves of (a) hydrous Ru oxides and (b) hydrous Ir oxides measured in 0.5 M $H_2SO_4$ electrolyte. (c,d) Tafel plots of (c) hydrous Ru oxides and (d) hydrous Ir oxides and the Tafel slopes obtained by the linear fittings based on the Tafel equation.

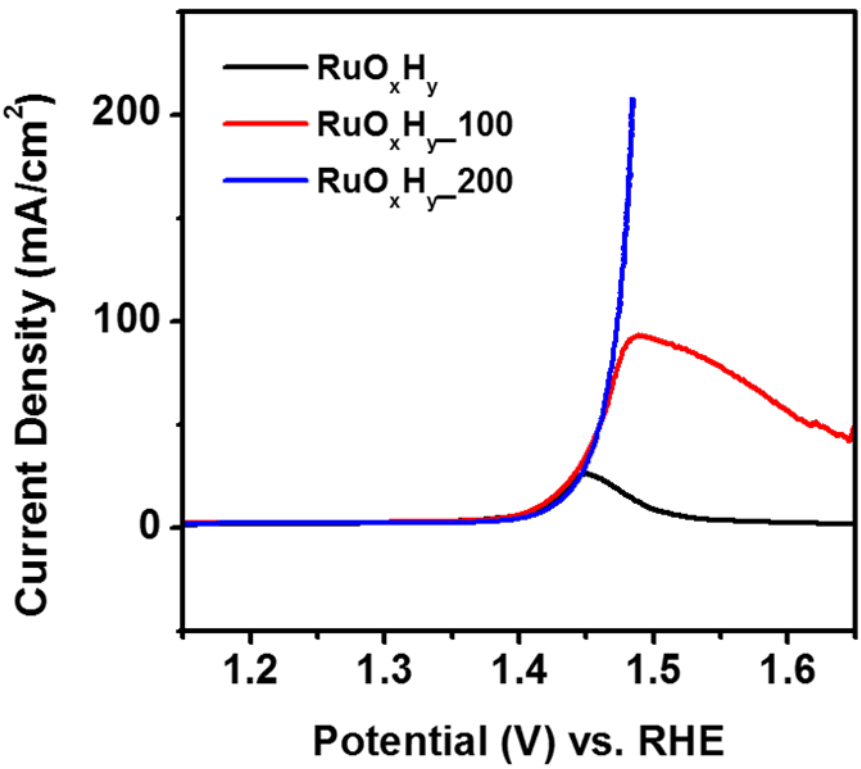


**Figure 3.7.** iR-corrected 1st scan of oxygen evolution reaction (OER) polarization curves of $RuO_xH_y$s, $RuO_xH_y$_100, and $RuO_xH_y$_200 measured in 0.5 M $H_2SO_4$ electrolyte.

| | Potential (V) at 10 $mAcm^{-2}$ | | Potential (V) at 10 $mAcm^{-2}$ |
|---|---|---|---|
| $RuO_xH_y$ | N/A | $IrO_xH_y$ | 1.537 |
| $RuO_xH_y$ 100 | N/A | $IrO_xH_y$ 100 | 1.537 |
| $RuO_xH_y$ 200 | 1.427 | $IrO_xH_y$ 200 | 1.567 |
| $RuO_xH_y$ 300 | 1.487 | $IrO_xH_y$ 300 | 1.574 |
| $RuO_xH_y$ 400 | 1.505 | $IrO_xH_y$ 400 | 1.582 |
| $RuO_xH_y$ 500 | 1.540 | $IrO_xH_y$ 500 | 1.612 |

**Table 3.2.** Potential values (vs. RHE) at OER current densities of 10 $mA/cm^2$ for hydrous Ru and Ir oxides.

| | Electrolyte | Substrate | Current density ($mAcm^{-2}$) at specific overpotential | Tafel slope (mV/dec) | Ref. |
|---|---|---|---|---|---|
| $RuO_2$ | 0.1 M $HClO_4$ | GCE | 0.01 @ 250 mV | N/A | 47 |
| $RuO_2$ | 0.5 M $H_2SO_4$ | Au | 0.03 @ 250 mV | 50 | 40 |
| $IrO_2$ | 0.1 M $HClO_4$ | GCE | 0.004 @ 250 mV | N/A | 47 |
| $IrO_2$ | 0.5 M $H_2SO_4$ | Au | 0.0015 @ 250 mV | 57.8 | 40 |
| $IrO_2$@$RuO_2$ | 0.5 M $H_2SO_4$ | Au | 6 @ 250 mV | 60.2 | 40 |
| NiCeOx-Au | 1.0 M KOH | Au | ~ 1 @ 250 mV | N/A | 48 |
| $IrO_x/SrIrO_3$ | 0.5 M $H_2SO_4$ | $SrIrO_3$ | 1 ~ 2 @ 250 mV | N/A | 12 |
| $RuO_xH_y$ 200 /oxide area | 0.5 M $H_2SO_4$ | GCE | 0.49 @ 250 mV | 46.4 | This work |

**Table 3.3.** Comparison of oxygen evolution reaction activities of the state-of-the-art electrocatalysts in the previous literatures and $RuO_xH_y$_200 in this study.

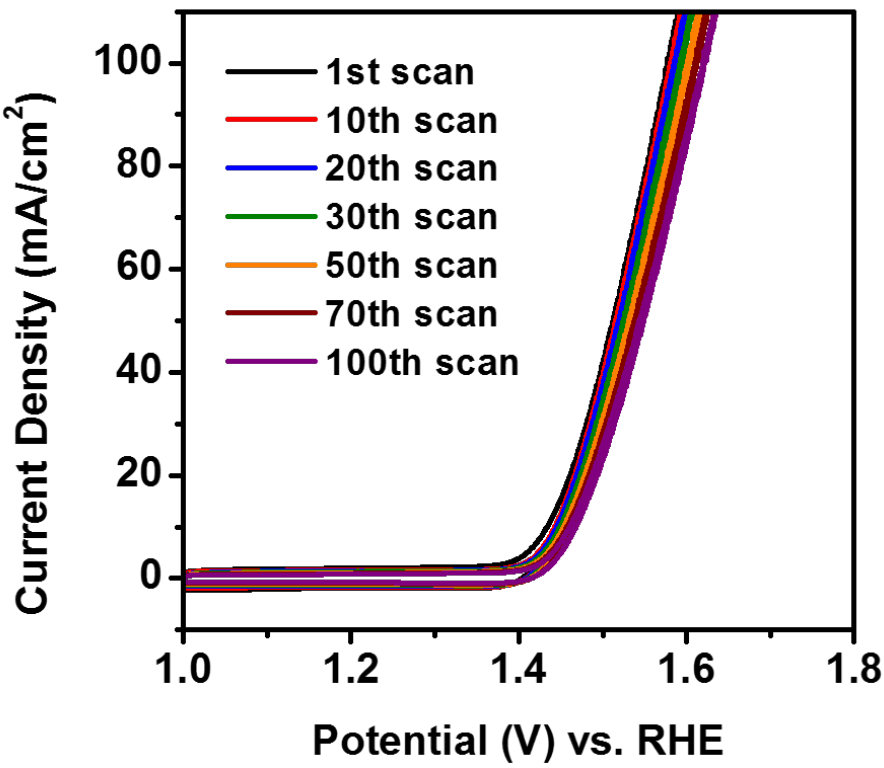


**Figure 3.8.** iR-corrected oxygen evolution reaction (OER) polarization curves of $RuO_xH_y$_200 measured in 0.5 M $H_2SO_4$ for 100 potential cycles.

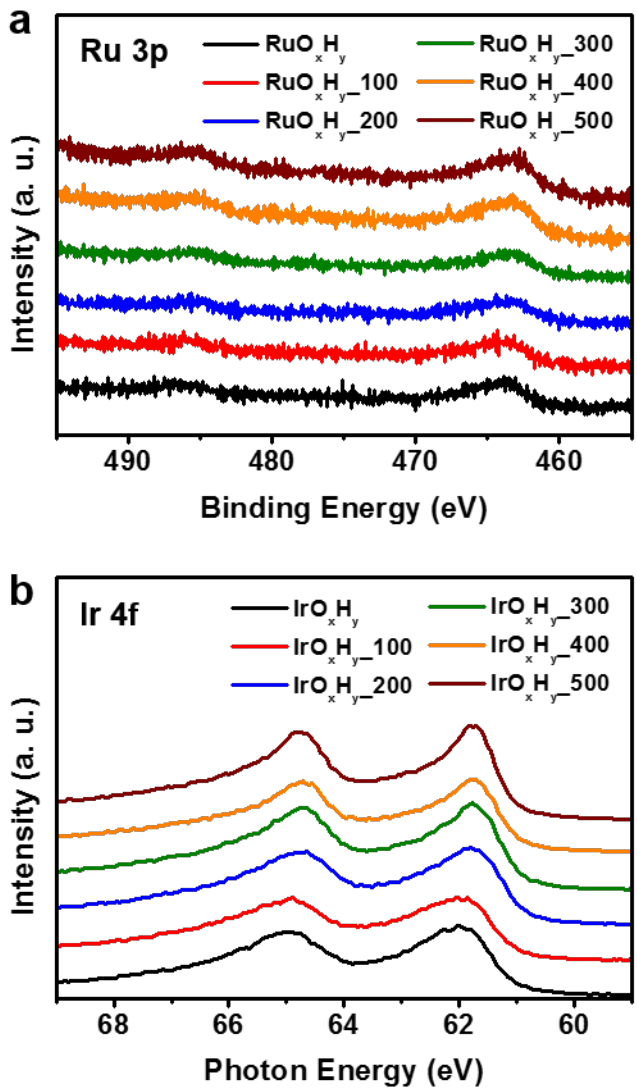


**Figure 3.9.** Synchrotron X-ray photoelectron spectroscopy (XPS) results of (a) hydrous Ru oxides at Ru 3p core level and (b) hydrous Ir oxides at Ir 4f core level.

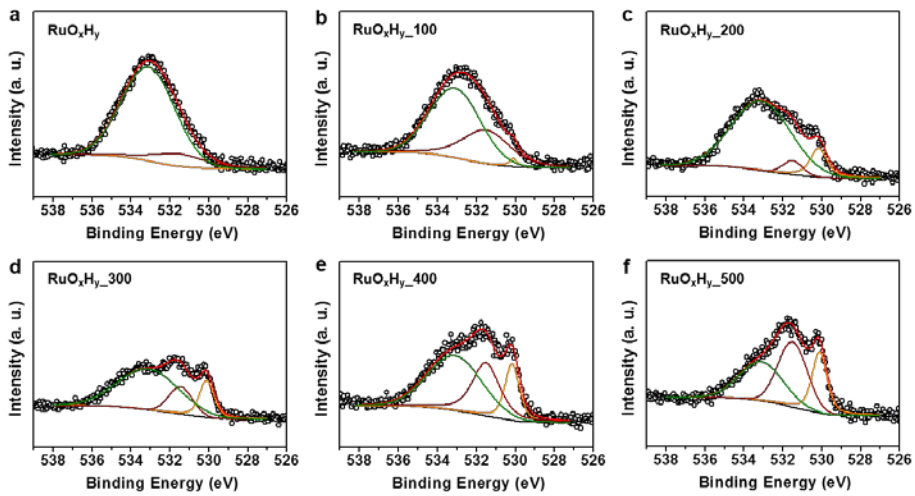


**Figure 3.10.** Synchrotron X-ray photoelectron spectroscopy (XPS) results of hydrous Ru oxides obtained at O 1s core level and the fitted curves.

| | Areal Ratio (%) | | |
|---|---|---|---|
| | O1 | O2 | O3 |
| $RuO_xH_y$ | N/A | 14.08 | 85.92 |
| $RuO_xH_y$ 100 | 1.80 | 34.34 | 63.86 |
| $RuO_xH_y$ 200 | 12.92 | 5.62 | 81.46 |
| $RuO_xH_y$ 300 | 17.49 | 17.20 | 65.31 |
| $RuO_xH_y$ 400 | 17.60 | 32.48 | 50.92 |
| $RuO_xH_y$ 500 | 24.06 | 40.10 | 35.84 |

**Table 3.4.** Fitted results of the O 1s XPS spectra of hydrous Ru oxides displayed in Figure 3.10.

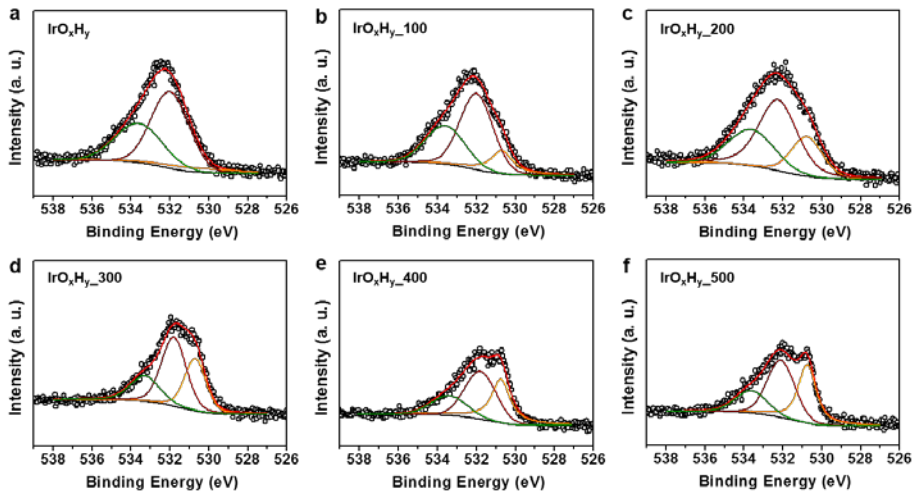


**Figure 3.11.** Synchrotron X-ray photoelectron spectroscopy (XPS) results of hydrous Ir oxides obtained at O 1s core level and the fitted curves.

| | Areal Ratio (%) | | |
|---|---|---|---|
| | O1 | O2 | O3 |
| $IrO_xH_y$ | 6.71 | 56.81 | 36.48 |
| $IrO_xH_y$ 100 | 15.78 | 53.14 | 31.08 |
| $IrO_xH_y$ 200 | 21.22 | 51.37 | 27.41 |
| $IrO_xH_y$ 300 | 31.43 | 46.94 | 21.63 |
| $IrO_xH_y$ 400 | 35.89 | 43.60 | 20.51 |
| $IrO_xH_y$ 500 | 36.08 | 45.10 | 18.82 |

**Table 3.5.** Fitted results of the O 1s XPS spectra of hydrous Ir oxides displayed in Figure 3.11.

In the previous literatures, defective oxygen was often understood as a descriptor for the OER activity in alkaline media.[50,51] In contrast, the trend of O2 in Ru oxides and Ir oxides were opposite in my experiments, and this indicates that the OER activity is not governed by the portion of defective O in acidic electrolyte. In order to investigate the relationship between the O in different chemical states and the OER activity, relative amounts of each oxygen species were plotted with regard to the OER activities (represented by potential values at 10 $mA/cm^2$ of OER current), as displayed in Figure 3.12. In the case of O1 (Figure 3.12a) and O2 (Figure 3.12b), linear correlation between the portion and OER activity was hardly observable ($R^2$ being less than 0.7 in linear fittings), though the linear trends in Ru and Ir oxides were observable in separate. In contrast, high linearity ($R^2 > 0.9$) was clearly apparent for whole Ru and Ir oxide catalysts in the case of O3 (Figure 3.12c). Therefore, it is suggested that the portion of adsorbed oxygen species as a general descriptor for OER activity in acid electrolyte. This also indicates that adsorbed oxygen species on the surface have crucial role in acidic media.

In order to further understand the physicochemical state of oxygen in the hydrous oxide catalysts and the OER activity in acidic media, near edge X-ray absorption fine structure (NEXAFS) spectra of the oxide hydrate catalysts were obtained at oxygen K-edge, and the results are displayed in Figure 3.13. These spectra reflect the dipole electron transitions from the O 1s to the unoccupied O2p state which is hybridized with Ru4d or Ir5d state.[52,53] In the case of Ru oxides (Figure 3.13a), excitation energy positions at peak intensities were marked as follows: peak (i) at 529 – 530 eV responsible for the electronic transition into $t_{2g}$ state, peak (ii) at 532 – 533 eV from the electronic transition into $e_g$ state, and peak (iii) at around 530 eV originating from the scattering events. In pristine $RuO_xH_y$, relatively broad (i) and (ii) peaks were observable, and this can be attributed to the solid state broadening induced by hydrated water in ruthenium oxides. Peak (iii) is known to be dependent on the distances between the oxygen atoms, and from the

diminishing of peak (iii) as the annealing temperature was increased, elongation of oxygen-oxygen distance was perceived, as can be indirectly cross-checked from the metal-metal distances in the EXAFS spectra displayed in Figure 4c. In the case of NEXAFS spectra of Ir oxide samples (Figure 3.13b), only peaks (i) and (ii) responsible for the electronic transition into $t_{2g}$ and $e_g$ states were apparent, respectively. Peak broadening was also observable in pristine $IrO_xH_y$, and a pre-peak at around 529 eV from defective oxygen introduced by Ir vacancies was visible in Ir oxides that were heat treated at relatively low temperatures. According to the previous publications by Pfeifer et al.,[38,39] electronic defects in anionic and cationic frameworks ($O^-$ and $Ir^{3+}$) are important for high OER activity, and this seems to be one of the reasons for higher OER performance in the $IrO_xH_y$ annealed in lower temperature. In both of the Ru and Ir oxides, the areal peak (i) / peak (ii) ratio was increased as the thermal annealing temperature was elevated. This can be understood as the vacancies in $t_{2g}$ compared to that in $e_g$ is becoming larger in Ru and Ir oxide catalysts after high-temperature treatment. Though there is no clear explanation for the relationship between the (i) / (ii) ratio and the OER activities, it could be concluded here that the relatively smaller vacancy in $t_{2g}$ state is beneficial for the electrocatalytic OER.

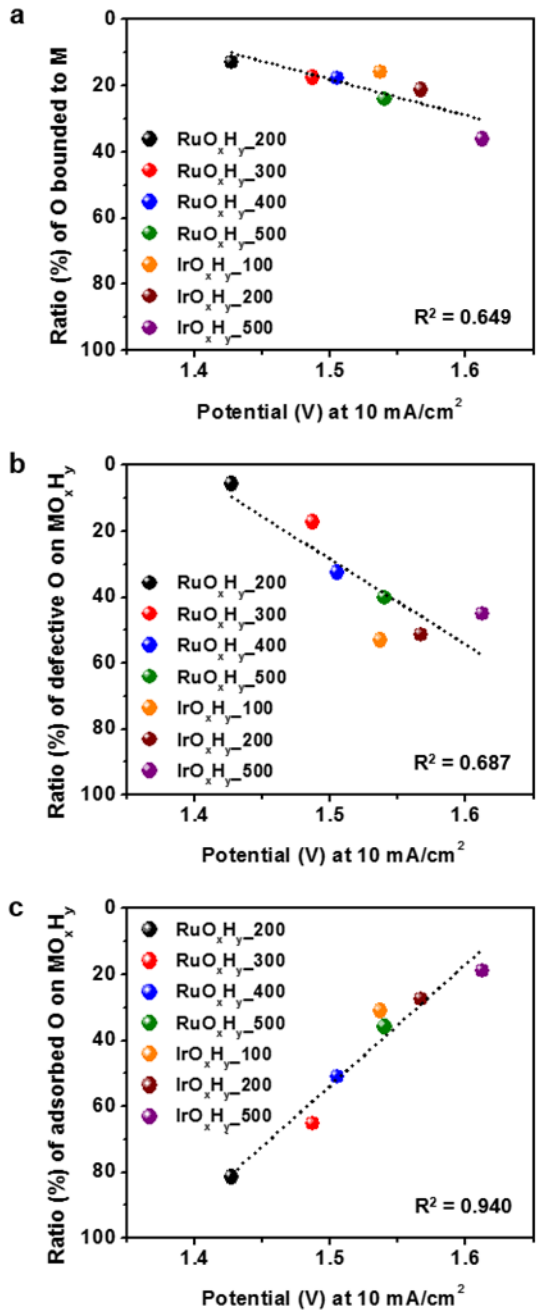


**Figure 3.12.** Comparisons between OER activities of hydrous oxide catalysts (represented by the potential values at 10 mA/cm$^2$) and portions of three different types of oxygen obtained by XPS analyses. (a) O1, (b) O2, and (c) O3.

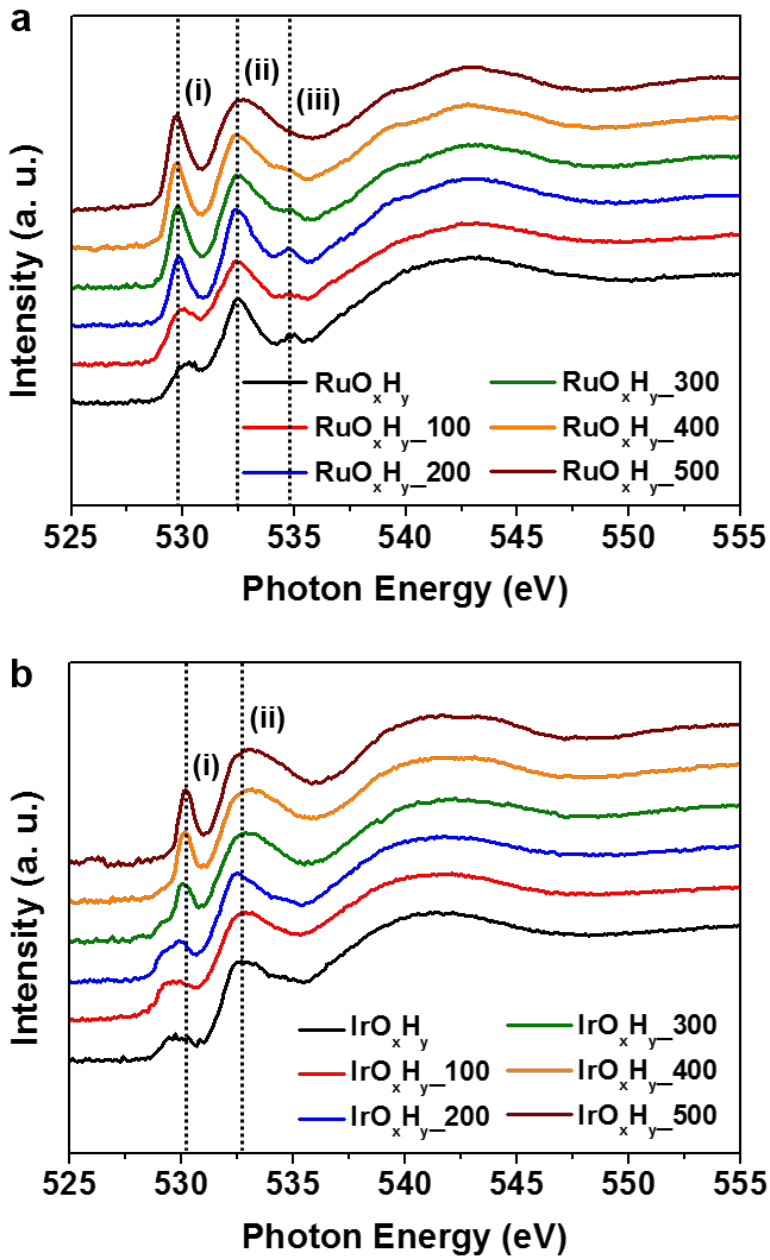


**Figure 3.13.** Near edge X-ray absorption fine structure (NEXAFS) spectra of (a) hydrous Ru oxides and (b) hydrous Ir oxides obtained at O K-edge.

### 3.3.3. Oxophilic effect in acidic medium

In Chapter 2, investigations on bifunctional effect in CO oxidation was performed by a blend of Pt/C and $RuO_xH_y$. Based on the discussion in previous section, further studies on the role of hydrous oxides in CO oxidation was performed. For a more clear verification on the effect of junctions between Pt nanoparticles and $RuO_xH_y$, that the main origin of enhanced CO oxidation is not the migration of adsorbed CO to the Pt-$RuO_xH_y$ contact region, blended catalysts with nominally same number of $RuO_xH_y$-carbon support junction but different probability for the presence of Pt nanoparticles at the junction were prepared by using proper amounts of commercial Pt/C with different loading levels (20 wt%, 40 wt% and 60 wt%) of Pt nanoparticles, of which TEM images are displayed in Figure 3.14. The selection of pristine $RuO_xH_y$ was based on the consideration that $RuO_xH_y$ is the most oxophilic material among the hydrous oxides with high OER activity (before the dissolution in high potentials as depicted in Figure 3.7). Figure 3.15 to Figure 3.17 show the TEM analysis results of blended catalysts, wherein uniform mixture of Pt/C and $RuO_xH_y$ are clearly observable. A very small portion of Pt nanoparticles were in direct contact with $RuO_xH_y$, and from the different density of Pt nanoparticles on the carbon supports in the case of 20 wt% (Figure 3.15), 40 wt% (Figure 3.16), and 60 wt% (Figure 3.17) Pt/C catalysts, it was indirectly verified that the control in the number of junctions was properly accomplished. Then, CO oxidations after monolayer adsorption on the surface of Pt (monolayer CO oxidation) were performed in the three blended catalysts, and the results are displayed in Figures 3.18a (20 wt%), 3.18b (40 wt%), and 3.18c (60 wt%). From the CO oxidation potentials and areas under monolayer CO oxidation currents, which shows the amount of CO oxidized at certain potentials, enhancements in CO oxidation by incorporation of $RuO_xH_y$ were calculated by the portion of negatively shifted areas. There were two noteworthy observations: First, though the portion of Pt nanoparticles in direct contact with $RuO_xH_y$ was extremely small, enhancement

in CO oxidation was significant (>10%) in all of the blended catalysts. Second, enhancements in CO oxidation did not show any increase when the loading level of Pt was increased from 20 wt% to 40 wt%. This indicates that the major origin of enhancement in CO oxidation is not the effect of direct contact between the Pt/C and $RuO_xH_y$. Meanwhile, in the case of 60 wt% Pt/C, enhancement in monolayer CO oxidation was as large as 19.7%. This can be attributed to the agglomeration of Pt nanoparticles induced by reduced inter-Pt nanoparticle distances as a result of increased loading level, because migration of CO along the connected Pt nanoparticles may take place. In this case, due to the significantly large rate constants for migration of CO on Pt compared to those for desorption of CO from Pt, CO adsorbed on Pt nanoparticles that are not in direct contact with $RuO_xH_y$ but are connected to the Pt that is forming a junction with $RuO_xH_y$ may move toward $RuO_xH_y$ and react with –OH on the surface of $RuO_xH_y$. However, it is clear from the TEM image that the portion of Pt nanoparticle at the junctions are still negligibly small in the case of 60 wt% Pt/C, and therefore the main reason for the enhanced CO oxidation is unlikely to result from the direct contact between Pt and OER catalyst. This was additionally checked by performing CO oxidation with continuous CO feed (bulk CO oxidation) using the same blended catalysts. Figure 3.18d shows the bulk CO oxidation results, and the enhancements in CO oxidation performance were quantified by the magnitude of negative shifts in the peak potentials. The potential shifts in the blended catalysts with different loading level of Pt were within comparable range, and it was notable to observe that the shifts in the peak potentials were almost identical in the cases of 40 wt% (157 mV) and 60 wt% (159 mV).

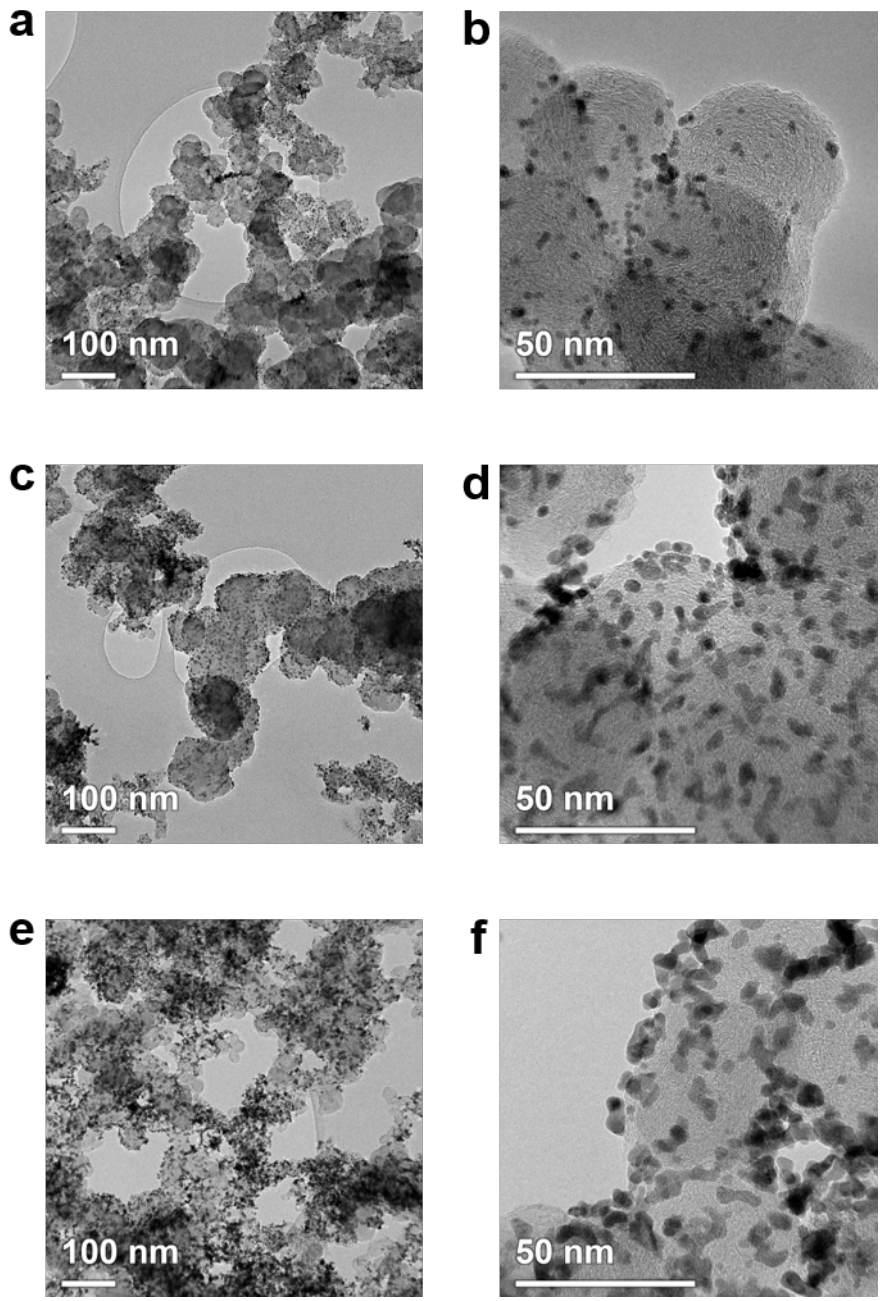


**Figure 3.14.** Transmission electron microscopy (TEM) images of Pt/Cs with different loading levels of Pt. (a,b) 20 wt%, (c,d) 40 wt%, and (e,f) 60 wt%.

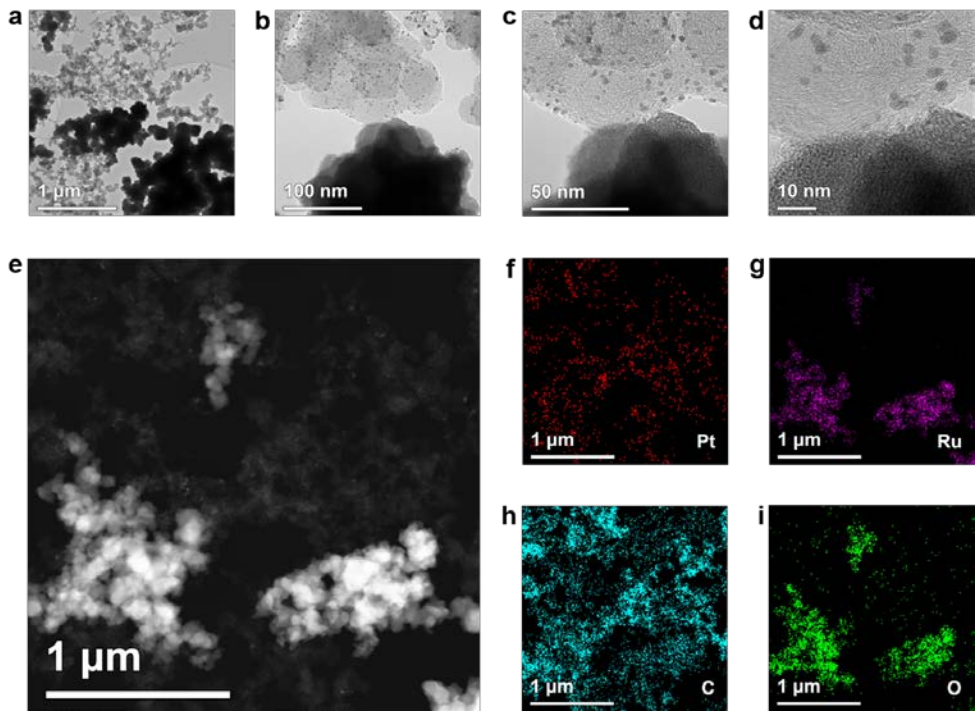


**Figure 3.15.** (a-d) TEM images of the blended catalyst comprising 20 wt% Pt/C and $RuO_xH_y$ at various magnifications. (e) STEM image of the blended catalyst and (f-i) the corresponding elemental EDS maps of (f) Pt, (g) Ru, (h) C, and (i) O.

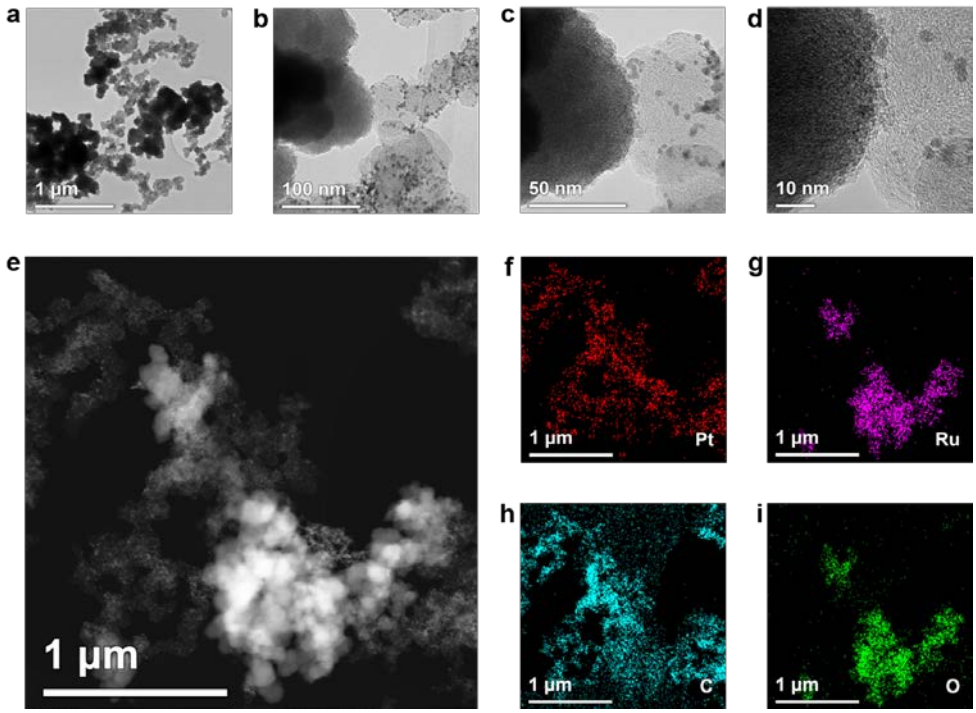


**Figure 3.16.** (a-d) TEM images of the blended catalyst comprising 40 wt% Pt/C and $RuO_xH_y$ at various magnifications. (e) STEM image of the blended catalyst and (f-i) the corresponding elemental EDS maps of (f) Pt, (g) Ru, (h) C, and (i) O.

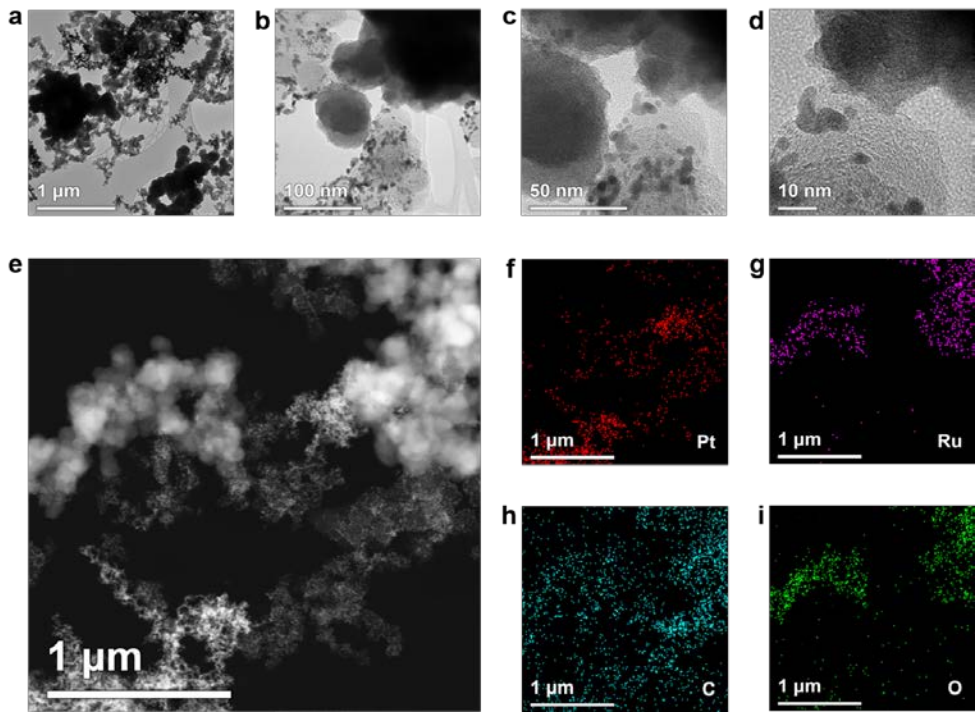


**Figure 3.17.** (a-d) TEM images of the blended catalyst comprising 60 wt% Pt/C and $RuO_xH_y$ at various magnifications. (e) STEM image of the blended catalyst and (f-i) the corresponding elemental EDS maps of (f) Pt, (g) Ru, (h) C, and (i) O.

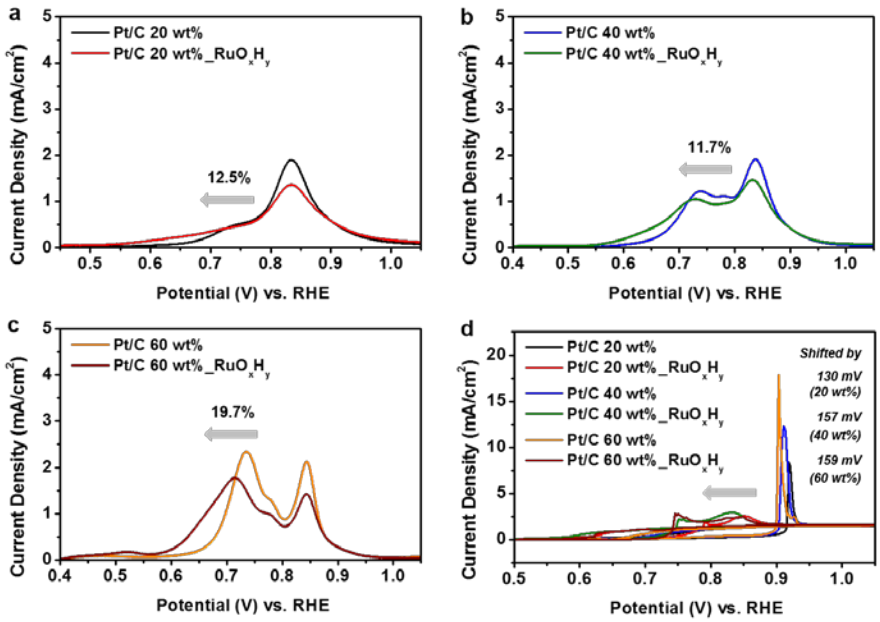


**Figure 3.18.** Background-corrected CO stripping results of (a) Pt/C 20 wt% and Pt/C 20 wt%_$RuO_xH_y$, (b) Pt/C 40 wt% and Pt/C 40 wt%_$RuO_xH_y$, and (c) Pt/C 60 wt% and Pt/C 60 wt%_$RuO_xH_y$ measured in $H_2SO_4$ electrolyte after monolayer CO adsorption. (d) Background-corrected bulk CO oxidation results measured in CO saturated 0.5 M $H_2SO_4$ with rotation at 1600 rpm.

Considering that the effect of OER catalysts in this case is diverse from the conventional bifunctional mechanisms that are valid when Pt and oxophilic material is neighboring to each other, it was unable to address the enhanced CO oxidation in the blended catalysts by the interpretations in former reports.[28-30,36,37] Therefore, in order to figure out the effect of oxophilic materials in the blends, bulk CO oxidations were performed with blended catalysts composed of Pt/C and OER catalysts with different activities ($RuO_xH_y$_200 to 500, and $IrO_xH_y$_100, 200, and 500). The STEM images and elemental EDS maps of blended catalysts are depicted in Figure 3.19 (blends of Pt/C and Ru oxides) and Figure 3.20 (blends of Pt/C and Ir oxides), which clearly show that the blends were prepared with high uniformity. Then the electronic interaction between Pt and hydrous oxides was investigated by XPS analyses (Figure 3.21), and lack of electronic effect was clearly verified in all of the blended catalysts by identical XPS Pt 4f spectra. In addition, inertness of the oxide hydrates in CO oxidation was confirmed (Figure 3.22).

Figure 3.23 shows the bulk CO oxidation results of blended catalysts obtained by electrochemical measurements at various scan rates. In all of the cases, trend in CO stripping performance was in line with that in the OER activities of the incorporated hydrous oxides. For quantitative comparisons, potentials at the first half maximum of CO oxidation peaks were selected as representative values, and they are shown in the legends. Figure 3.24 shows the comparison between OER activity (which is evaluated by the potential at current density of 10 $mA/cm^2$ in OER, as depicted in Table 3.2) and CO oxidation performance of hydrous oxide catalysts, and linear correlation between the OER activity and CO oxidation performance was observable. A stronger linearity was observed at higher scan rate, and $R^2$ value was increased up to 0.985 when the bulk CO oxidation was performed at 50 mV/s. The linear relationship between the OER activity of the incorporated oxide hydrates and the CO oxidation performance in the blended catalysts shows that the enhancement in CO oxidation is originated from the

oxophilic properties of the oxide hydrate catalysts. Moreover, considering that the portion of Pt nanoparticles in direct contract with oxide hydrates are negligibly small, this linear correlation means that the CO oxidation characteristic of Pt can be modified by the –OH formation property at the surface of hydrous oxides that are not neighboring to the Pt nanoparticle.

In general, CO oxidation on Pt surface takes place by Langmuir-Hinshelwood reaction by –CO and –OH on the Pt surface. Therefore, the formation of –OH is necessary for CO oxidation, and dissociation of water molecule at the surface of Pt limits overall CO oxidation in acidic media.[54,55] Considering that the CO oxidation was significantly facilitated by the presence of hydrous oxides, it can be understood that –OH formation on the Pt nanoparticles in the blended catalysts are actually being influenced by the event of –OH formation on the hydrous oxide catalysts (located at a fairly far distance), which is also a result of water dissociation at the surface (of the hydrous oxide). In short, it is clear from the experimental observations that facilitated water dissociation can accelerate another dissociation of a water molecule that is not necessarily neighboring to the formerly dissociated water molecule.

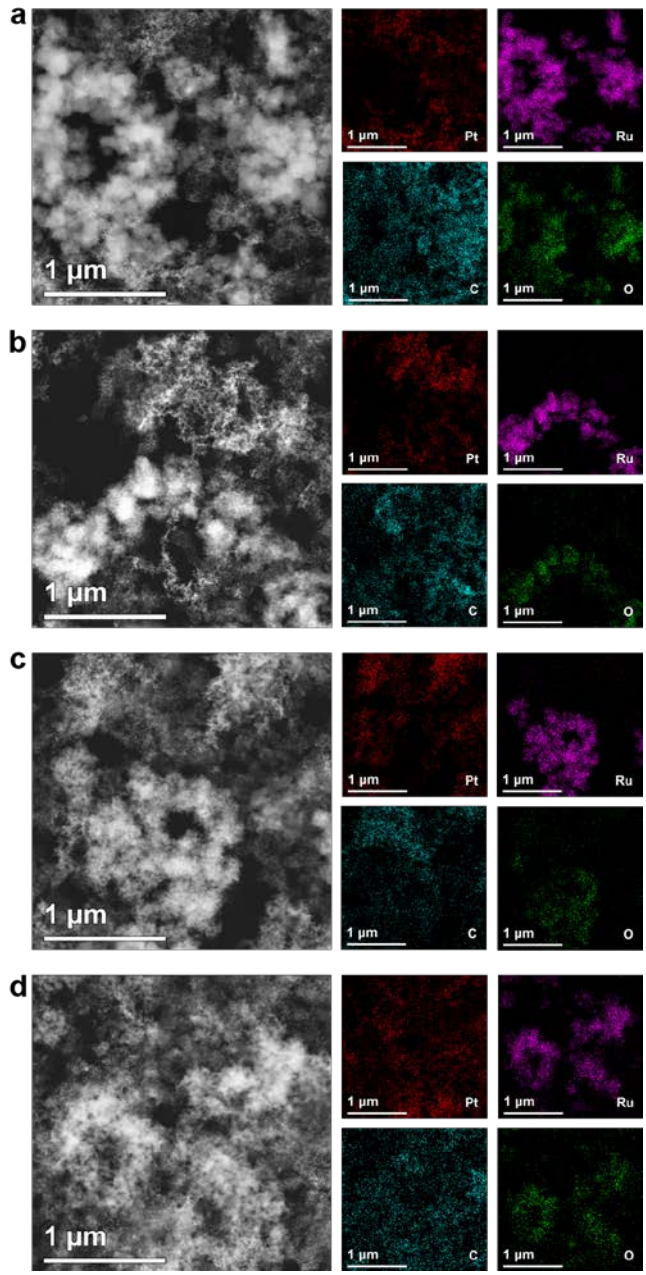


**Figure 3.19.** STEM image of the blended catalysts comprising Pt/C and thermally annealed hydrous Ru oxides at various temperatures and the corresponding elemental EDS maps of Pt, Ru, C, and O. (a) $RuO_xH_y$_200, (b) $RuO_xH_y$_300, (c) $RuO_xH_y$_400, and (d) $RuO_xH_y$_500.

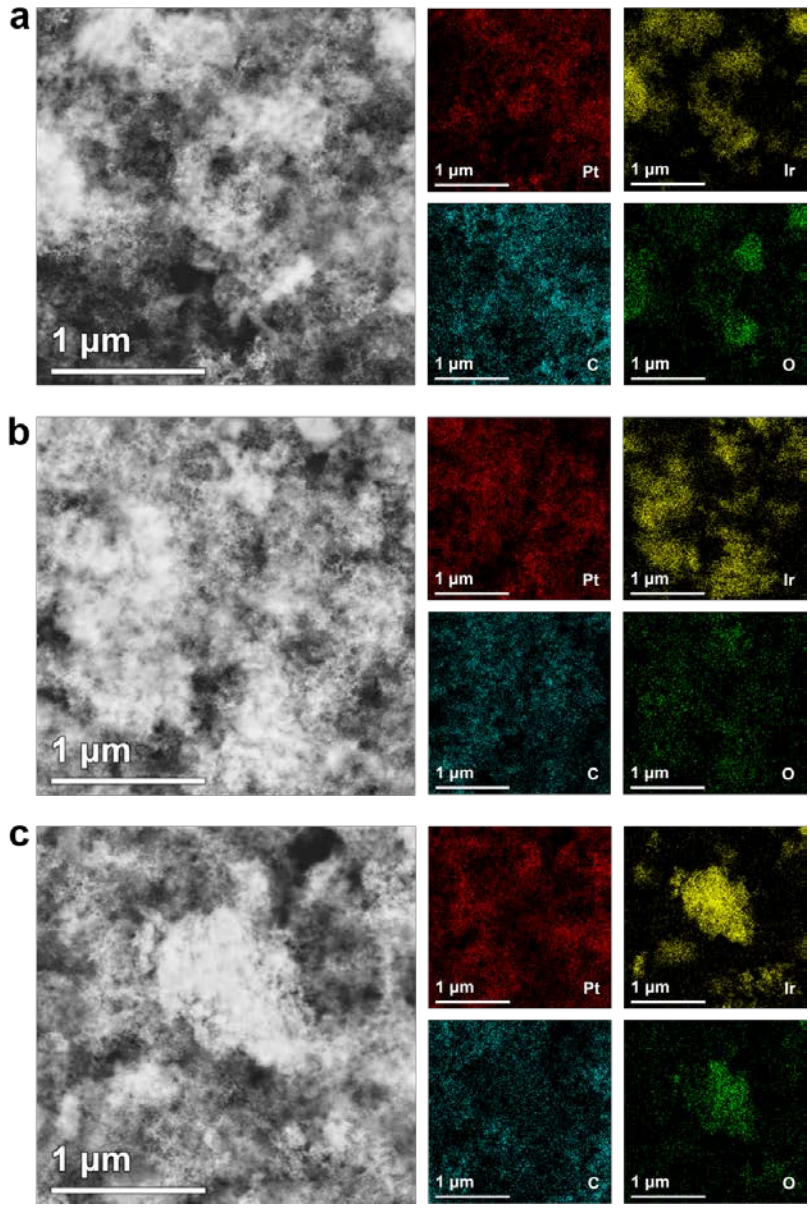


**Figure 3.20.** STEM image of the blended catalysts comprising Pt/C and thermally annealed hydrous Ir oxides at various temperatures and the corresponding elemental EDS maps of Pt, Ir, C, and O. (a) $IrO_xH_y$_100, (b) $IrO_xH_y$_200, and (c) $IrO_xH_y$_500.

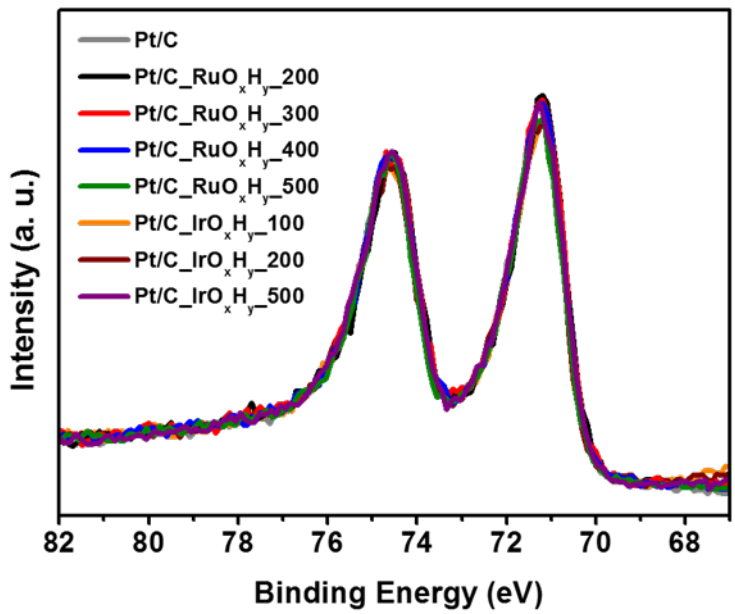


**Figure 3.21.** XPS Pt 4f spectra of the blended catalysts comprising Pt/C and hydrous oxides.

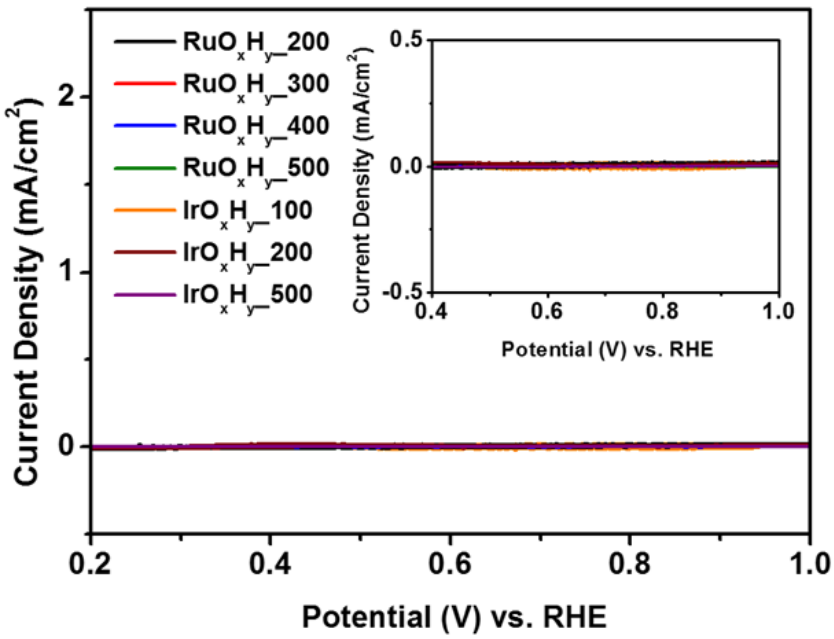


**Figure 3.22.** Background-corrected bulk CO oxidation results of hydrous Ru and Ir oxides measured in CO saturated 0.5 M $H_2SO_4$ with rotation at 1600 rpm.

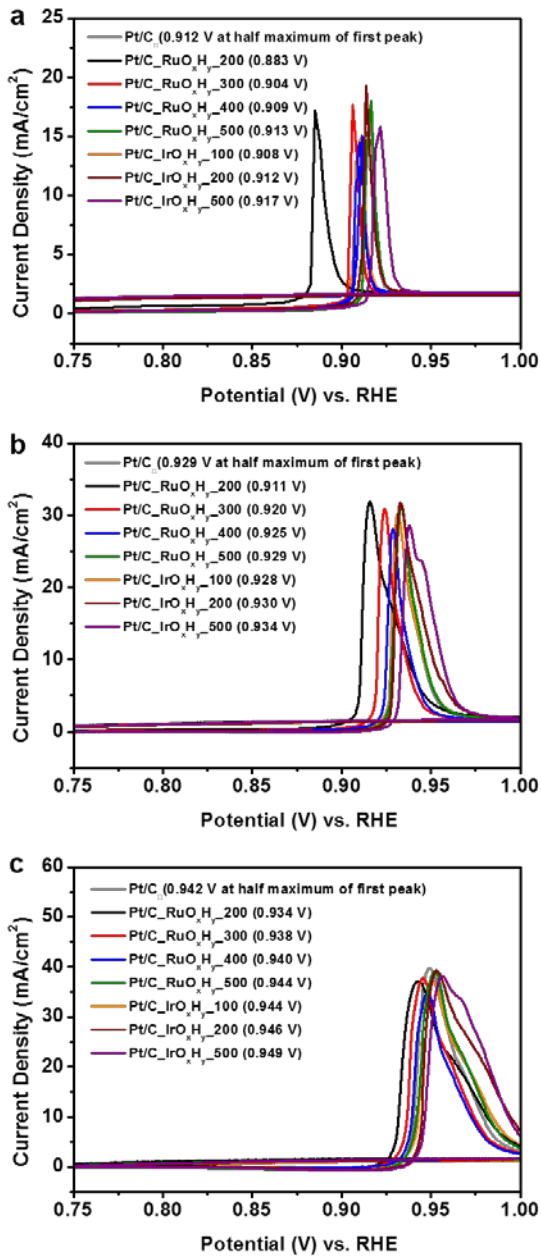


**Figure 3.23.** Background-corrected bulk CO oxidation results of the blended catalysts measured in CO saturated 0.5 M $H_2SO_4$ at the scan rates of (a) 5 mV/s, (b) 20 mV/s, and (c) 50 mV/s with rotation at 1600 rpm. Potential values at first half-maximums of CO oxidation currents were obtained for quantitative comparisons.

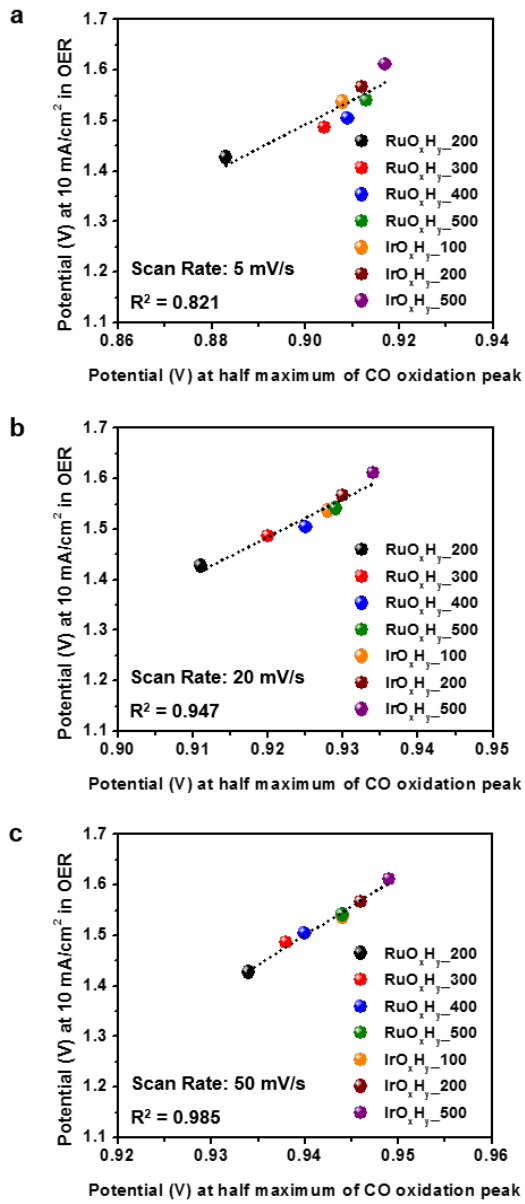


**Figure 3.24.** Comparisons between CO oxidation performances of the blended catalysts (represented by the potential values at the first half-maximum of the CO oxidation peaks and OER activities of the hydrous oxides (represented by the potential values at OER current density of 10 mA/cm$^2$). The comparisons were performed at three different scan rates of bulk CO oxidation; (a) 5 mV/s, (b) 20 mV/s, and (c) 50 mV/s.

In order to verify this long-range water activation, bulk CO oxidation for the blend of Pt/C and $RuO_xH_y$ was performed in $HClO_4$ solution at various concentrations. As in the case of model experiments in monolayer CO oxidation (Figure 3.18), pristine $RuO_xH_y$ was selected because it has the largest oxophilicity among the hydrous oxides, as can be observed from the dramatic shift of potential in the bulk CO oxidation (Figure 3.25). Usage of $HClO_4$ electrolyte was intended to neglect any anion adsorption effect at Pt surfaces. Figure 3.26 shows the bulk CO oxidation results for Pt/C and Pt/C_$RuO_xH_y$ in 0.01 M, 0.05 M, and 0.1 M $HClO_4$ solution. In the case of Pt/C, increase in the electrolyte concentration resulted in the rise of CO oxidation currents, and this can be attributed to the enhancement in ionic conductivity. However, the potentials for CO oxidation was irrelevant to the electrolyte concentration, and this clearly shows that the oxophilicity of Pt nanoparticles is not affected by the electrolyte concentration. On the other hand, negative shift in CO oxidation potential in addition to the increment in CO oxidation current was observable in the blended catalyst. From this result, it could be verified that the oxophilicity (water dissociation property in this case) of Pt nanoparticles are tailored by the long-range interaction with $RuO_xH_y$, which seems to be transferred through electrolyte. In acidic media, proton conduction mechanism is generally known as the switching of the O-H bond and hydrogen bond in chains of water molecules.[56,57] Based on this mechanism, the experimental results can be explained without any leap of logic, because water dissociation at the surface of hydrous oxide can affect the –OH formation at the surface of a Pt nanoparticle through the chains of water molecules connected by O-H and hydrogen bond. In the potential ranges prior to CO oxidation, formation of –OH takes place at the surface of $RuO_xH_y$ by $H^+$ adsorption or water dissociation. In either case, local change in pH near the surface of $RuO_xH_y$ may induce switching of O-H and hydrogen bonds which may lead to fluctuations in the covalency of O-H bond in water molecules that are located near the Pt nanoparticles. This may

enable –OH formation on the Pt surface in a lower potential by facilitating water dissociation when O-H bond strength becomes instantly weaker. The long-range water activation by proton transfer mechanism is further supported by the enhanced CO oxidation property of the blended catalysts in higher electrolyte concentration, because changes in local proton concentrations, which accelerates the switching of bonds in water chains, occur in larger magnitude when proton concentration is increased. From the experimental observations and discussion above, it is strongly suggested the presence of long-range water activation by proton conduction mechanism in electrocatalysis performed in acidic media.

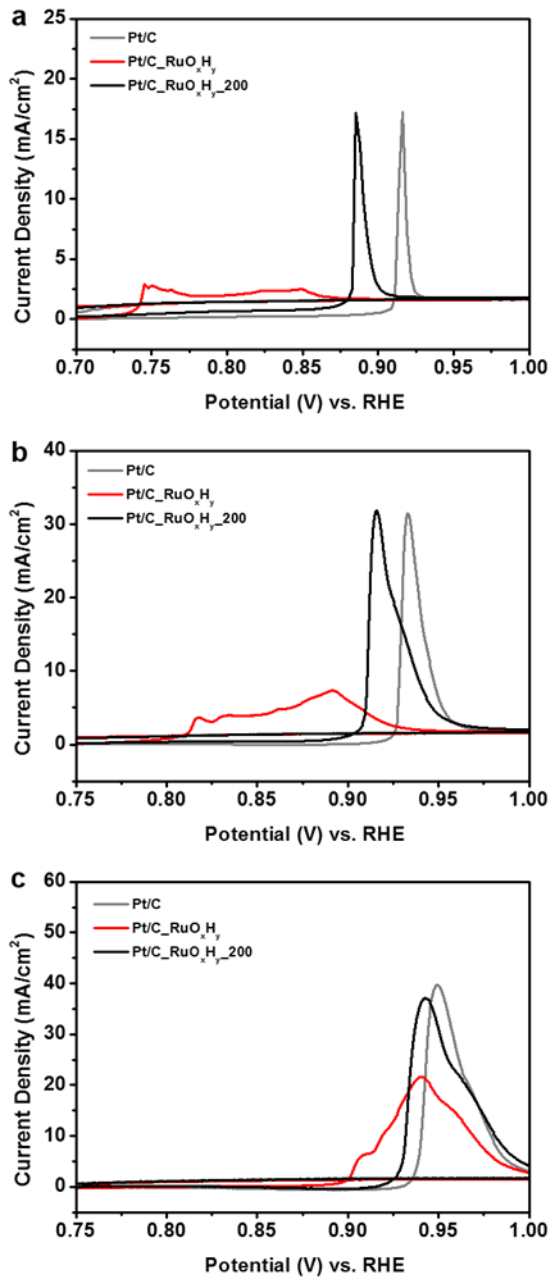


**Figure 3.25.** Background-corrected bulk CO oxidation results of Pt/C, Pt/C_$RuO_xH_y$, and Pt/C_$RuO_xH_y$_200 measured in CO saturated 0.5 M $H_2SO_4$ at the scan rates of (a) 5 mV/s, (b) 20 mV/s, and (c) 50 mV/s with rotation at 1600 rpm.

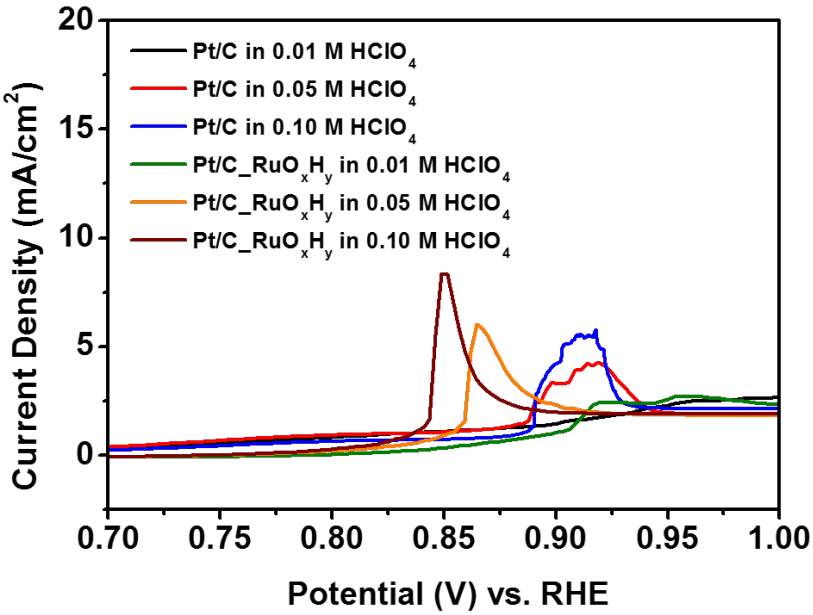


**Figure 3.26.** Background-corrected bulk CO oxidation results of Pt/C and Pt/C_$RuO_xH_y$ measured in CO saturated condition using $HClO_4$ electrolytes of various concentrations and with rotation at 1600 rpm.

## 3.4. Conclusions

In this chapter, investigations in OER activity and bifunctional effect in acidic media were performed by using $RuO_xH_y$ and $IrO_xH_y$ with modified degree of hydration by heat treatment in air. $RuO_xH_y$ was stabilized after thermal annealing in 200 °C and higher temperatures, and both $RuO_xH_y$ and $IrO_xH_y$ exhibited decrease in OER activity when the annealing temperature was elevated. Based on the different OER activities of hydrous oxide catalysts in acid electrolyte and keen interpretation of the XPS obtained at core level of oxygen, importance of hydroxyl groups or surface-adsorbed oxygen species was verified. Moreover, blended catalysts composed of uniformly mixed Pt/C and oxide hydrates with different OER activity, which represents oxophilicity, were prepared, and long-range water activation that facilitates –OH formation on Pt surface was verified by various model experiments in CO oxidation.

## 3.5. References


[1] Stamenkovic, V. R.; Fowler, B.; Mun, B. S.; Wang, G.; Ross, P. N.; Lucas, C. A.; Marković, N. M. *Science* **2007**, *315*, 493−497.

[2] Greeley, J.; Stephens, I. E. L.; Bondarenko, A. S.; Johansson, T. P.; Hansen, H. A.; Jaramillo, T. F.; Rossmeisl, J.; Chorkendorff, I.; Nørskov, J. K. *Nat. Chem.* **2009**, *1*, 552−556.

[3] Kim, O.-H.; Cho, Y.-H.; Kang, S. H.; Park, H.-Y.; Kim, M.; Lim, J. W.; Chung, D. Y.; Lee, M. J.; Choe, H.; Sung, Y.-E. *Nat. Commun*. **2013**, *4*, 2473.

[4] Cho, H.; Kim, S. M.; Kang, Y. S.; Kim, J.; Jang, S.; Kim, M.; Park, H.; Bang, J. W.; Seo, S.; Suh, K.-Y.; Sung, Y.-E, Choi, M. *Nat. Commun*. **2015**, *6*, 8484.

[5] Barbir, F. *Solar Energy* **2005**, *78*, 661−669.

[6] Grigoriev, S. A.; Porembsky, V. I.; Fateev, V. N. *Int. J. Hydrogen Energ*. **2006,** *31*, 171−175.

[7] Jiao, Y.; Zheng, Y.; Jaroniec, M.; Qiao, S. Z. *Chem. Soc. Rev.* **2015**, *44*, 2060−2086.

[8] Carmo, M.; Fritz, D. L.; Mergel, J.; Stolten, D. *Int. J. Hydrogen Energ*. **2013,** *31*, 4901−4934.

[9] Zhang, H.; Shen, P. K. *Chem. Soc. Rev.* **2012**, *41*, 2382−2394.

[10] Siracusano, S.; Van Dijk, N.; Payne-Johnson, E.; Baglio, V.; Aricò, A. S. *Appl. Catal., B* **2015**, *164*, 488−495.

[11] She, Z. W.; Kibsgaard, J.; Dickens, C. F.; Chorkendorff, I.; Nørskov, J. K.; Jaramillo, T. F. *Science* **2017**, *355*, eaad4998.

[12] Seitz, L. C.; Dickens, C. F.; Nishio, K.; Hikita, Y.; Montoya, J.; Doyle, A.; Kirk, C.; Vojvodic, A.; Hwang, H. Y.; Norskov, J. K.; Jaramillo, T. F. *Science*, **2016**, *353*, 1011−1014.

[13] Wu, G.; More, K. L.; Johnston, C. M.; Zelenay, P. *Science* **2011**, *332*, 443−447.

[14] Lim, B., Jiang, M.; Camargo, P. H. C.; Cho, E. C.; Tao, J.; Lu, X.; Zhu, Y.; Xia,

Y. *Science* **2009**, *324*, 1302−1305.

[15] Bing, Y.; Liu, H.; Zhang, L.; Ghosh, D.; Zhang, J. *Chem. Soc. Rev.* **2010**, *39*, 2184−2202.

[16] Kim, J.; Rong, C.; Liu, J. P.; Sun, S. *Adv. Mater.* **2009**, *21*, 906−909.

[17] Jackson, A.; Viswanathan, V.; Forman, A. J.; Larsen, A. H.; Nørskov, J. K.; Jaramillo, T. F. *ChemElectroChem* **2014**, *1*, 67−71.

[18] Chen, C.; Kang, Y.; Huo, Z.; Zhu, Z.; Huang, W.; Xin, H. L.; Snyder, J. D.; Li, D.; Herron, J. A.; Mavrikakis, M. *Science* **2014**, *343*, 1339−1343.

[19] Huang, X.; Zhao, Z.; Cao, L.; Chen, Y.; Zhu, E.; Lin, Z.; Li, M.; Yan, A.; Zettl, A.; Wang, Y. M.; Duan, X.; Mueller, T.; Huang, Y. *Science* **2015**, *348*, 1230−1234.

[20] Mistry, H.; Varela, A. S.; Kühl, S.; Strasser, P.; Cuenya, B. R. *Nat. Rev. Mater.* **2016**, *1*, 16009.

[21] Kitchin, J. R.; Nørskov, J. K.; Barteau, M. A.; Chen, J. G. *Phy. Rev. Lett.* **2004**, *93*, 156801.

[22] Strasser, P.; Koh, S.; Anniyev, T.; Greeley, J.; More, K.; Yu, C.; Liu, Z.; Kaya, S.; Nordlund, D.; Ogasawara, H.; Toney, M. F.; Nilsson, A. *Nat. Chem.* **2010**, *2*, 454−460.

[23] Jia, Q.; Liang, W.; Bates, M. K.; Mani, P.; Lee, W.; Mukerjee, S. *ACS Nano* **2015**, *9*, 387−400.

[24] Calle-Vallejo, F.; Martínez, J. I.; Rossmeisl, J. *Phys. Chem. Chem. Phys.* **2011**, *13*, 15639−15643.

[25] Stephens, I. E. L.; Bondarenko, A. S.; Grønbjerg, U.; Rossmeisl, J.; Chorkendorff, I. J. *Energy Environ. Sci.* **2012**, *5*, 6744−6762.

[26] Hammer, B; Norskov, J. K. *Adv. Catal.* **2000**, *45*, 71−129.

[27] Stamenkovic, V. R.; Mun, B. S.; Arenz, M.; Mayrhofer, J. J.; Lucas, C. A.; Wang, G.; Ross, P. N.; Marković N. M. *Nat. Mater.* **2007**, *6*, 241−247.

[28] Wang, H.; Abruña, H. D. *J. Phys. Chem. Lett.* **2015**, *6*, 1899−1906.

[29] Gasteiger, H. A.; Marković, N. M.; Ross, P. N.; Cairns, E. J. *J. Phys. Chem.*

**1994**, *98*, 617−625.

[30] Mukerjee, S.; Urian, R. C. *Electrochim. Acta.* **2002**, *47*, 3219−3231.

[31] Koper, M. T. M. *Surf. Sci.* **2004**, *548*, 1−3.

[32] Roth, C.; Benker, N.; Buhrmester, T.; Mazurek, M.; Loster, M.; Fuess, H.; Koningsberger, D. C.; Ramaker, D. E. *J. Am. Chem. Soc.* **2005**, *127*, 14607−14615.

[33] Wakisaka, M.; Mitsui, S.; Hirose, Y.; Kawashima, K.; Uchida, H.; Watanabe, M. *J. Phys. Chem. B* **2006**, *110*, 23489−23496.

[34] Lu, C.; Rice, C.; Masel, R. I.; Babu, P. K.; Waszczuk, P.; Kim, H. S.; Oldfield, E.; Wieckowski, A. *J. Phys. Chem. B* **2002**, *106*, 9581−9589.

[35] Jeon, T.-Y.; Lee, K.-S.; Yoo, S. J.; Cho, Y.-H.; Kang, S. H.; Sung, Y.-E. *Langmuir* **2010**, *26*, 9123−9129.

[36] Subbaraman, R.; Tripkovic, D.; Strmcnik, D.; Chang, K.-C.; Uchimura, M.; Paulikas, A. P.; Stamenkovic, V.; Markovic, N. M. *Science*, **2011**, *334*, 1256−1260.

[37] Subbaraman, R.; Tripkovic, D.; Chang, K.-C.; Strmcnik, D.; Paulikas, A. P.; Hirunsit, P.; Chan, M.; Greely, J.; Stamenkovic, V.; Markovic, N. M. *Nat. Mater.* **2012**, *11*, 550−557.

[38] Pfeifer, V.; Jones, T. E.; Velasco Vélez, J. J.; Massué, C.; Arrigo, R.; Teschner, D.; Girgsdies, F.; Scherzer, M.; Greiner, M. T.; Allan, J.; Hashagen, M.; Weinberg, G.; Piccinin, S.; Hävecker, M.; Knop-Gericke, A.; Schlögl, R. *Surf. Interface Anal.* **2016**, *48*, 261−273.

[39] Pfeifer, V.; Jones, T. E.; Velasco Vélez, J. J.; Massué, C.; Greiner, M. T.; Arrigo, R.; Teschner, D.; Girgsdies, F.; Scherzer, M.; Allan, J.; Hashagen, M.; Weinberg, G.; Piccinin, S.; Hävecker, M.; Knop-Gericke, A.; Schlögl, R. *Phys. Chem. Chem. Phys.* **2016**, *18*, 2292−2296.

[40] Audichon, T.; Napporn, T. W.; Canaff, C.; Morais, C.; Comminges, C.; Kokoh, K. B. *J. Phys. Chem. C* **2016**, *120*, 2562−2573.

[41] Zheng, J. P.; Huang, C. K. *J. New. Mat. Electr. Sys.* **2002**, *5*, 41−46.

[42] Dmowski, W.; Egami, T.; Swider-Lyons, K. E.; Love, C. T.; Rolison, D. R. *J.*

*Phys. Chem. B* **2002**, *106*, 12677−12683.

[43] Tsuji, E.; Imanishi, A.; Fukui, K.-i.; Nakato, Y. *Electrochim. Acta.* **2011**, *56*, 2009−2016.

[44] Reier, T.; Oezaslan, M.; Strasser, P. *ACS Catal.* **2012**, *2*, 1765−1772.

[45] Cherevko, S.; Geiger, S.; Kasian, O.; Kulyk, N.; Grote, J.-P.; Savan, A.; Shrestha, B. R.; Merzlikin, S.; Breitbach, B.; Ludwig, A.; Mayrhofer, K. J. J. *Catal. Today* **2016**, *262*, 170−180.

[46] de Faria, L. A.; Boodts, J. F. C.; Trasatti, S. *J. Appl. Electrochem.* **1996**, *26*, 1195−1199.

[47] Lee, Y.; Suntivich, J.; May, K. J.; Perry, E. E.; Shao-Horn, Y. *J. Phys. Chem. Lett.* **2012**, *3*, 399−404.

[48] Ng, J. W. D.; García-Melchor, M.; Bajdich, M.; Chakthranont, P.; Kirk, C.; Vojvodic, A.; Jaramillo, T. F. *Nat. Energy* **2016**, 1, 16053.

[49] Ananth, A.; Gandhi, M. S.; Mok, Y. S. *J. Phys. D: Appl. Phys*. **2013**, *46*, 155202.

[50] Bao, J.; Zhang, X.; Fan, B.; Zhang, J.; Zhou, M.; Yang, W.; Hu, X.; Wang, H.; Pan, B.; Xie, Y. *Angew, Chem*. **2015**, *127*, 7507−7512.

[51] Zhuang, L.; Ge, L.; Yang, Y.; Li, M.; Jia, Y.; Yao, X.; Zhu, Z. *Adv. Mater.* **2017**, 1606793.

[52] Tsai, H. M.; Babu, P. D.; Pao, C. W.; Chiou, J. W.; Jan, J. C.; Krishna Kumar, K. P.; Chien, F. Z.; Pong, W. F.; Tsai, M.-H.; Chen, C.-H.; Jang, L. Y.; Lee, J. F.; Chen, R. S.; Huang, Y. S.; Tsai, D. S. *Appl. Phys. Lett.* **2007**, *90*, 042108.

[53] Zhou, J. G.; Fang, H. T.; Hu, Y. F.; Sham, T. K.; Wu, C. X.; Liu, M.; Li, F. *J. Phys. Chem. C* **2009**, *113*, 10747−10750.

[54] Gu, X.-K.; Ouyang, R.; Sun, D.; Su, H.-Y.; Li, W.-X. *ChemSusChem* **2012**, *5*, 871–878.

[55] Wang, J. G.; Hammer, B. *J. Catal*. **2006**, *243*, 192–198.

[56] Erdey-Gruz, T. *Transport Phenomena in Electrolyte Solutions*; Adam Higler:

London, **1974**.

[57] Kornyshev, A. A.; Kuznetsov, A. M.; Spohr, E.; Ulstrup, J. *J. Phys. Chem. B* **2003**, *107*, 3351-3366

# Chapter 4. Studies on oxophilic effect in platinum nanocatalyst for electrocatalysis in basic medium

## 4.1. Introduction

Alkaline electrolytes have the effect of reducing the anion adsorption, and the oxygen reduction reaction and the oxygen evolution reaction are generally known to be faster than the electrochemical reaction in the acidic electrolyte.[1-5] In addition, since it is less corrosive than acidic electrolytes, the range of catalyst selection is wide, and non-precious metals or metal oxides other than platinum, carbon-based catalysts, and combinations of them have been extensively studied.[6-15] Therefore, various researches on alkaline anion exchange membrane fuel cell (AEMFC) and water-alkali electrolyzer which are operated in a basic environment have been studied.[16-22] The oxygen-based reactions are complex reactions, and many studies have been carried out, however, the hydrogen electrochemistry, which is the counter reactions of oxygen-based reactions, have also attracted much attention. Since rates of the hydrogen-based reactions are considerably slow in many catalysts including Pt in alkaline electrolytes, it is considered necessary to increase the reactivity of these catalysts. In addition, researches on this hydrogen oxidation/evolution reaction have been increased, and many discussions have been made about how to achieve enhanced activity of the catalysts.[23-25] The issue that is most actively discussed is whether only the hydrogen oxidation is affected by adsorption energy of hydrogen or by the adsorption energy of the hydroxyl group at the same time. In other words, the previous point is the study about the electronic effect which is finding the optimal catalytic activity depending on the hydrogen adsorption strength, and the later study is about increasing the hydrogen

oxidation by changing the oxophilicity of the catalyst.[26-33] Beyond this controversy, strong evidence has been reported that the oxophilic effect exists for the hydrogen evolution reaction (HER), the reverse reaction of hydrogen oxidation.[34,35] In HER mechanisms, it is noteworthy that Volmer step in basic media is dissociation step of water and the step generally shows low activities of HER catalysts including Pt. Pt catalyst is considered as efficient catalysts for the adsorption and recombination of the $H_{ad}$, however, it is inefficient in the water dissociation step.[34] Otherwise, it is known that the Pt is the most active catalyst as a single material, and studies for tuning its performance more optimally have been made. In the case of $M(OH)_2$ or MOOH deposited on Pt (111) substrate reported by N. Markovic's group, HER activity of Pt substrate was tuned by a metal-oxygen binding strength of deposited $M(OH)_2$ or MOOH.[35] They suggested that water dissociation step was promoted by those catalysts and Tafel step (recombination of adsorbed H atoms) occurred on Pt surface preceded by adsorption of H when water dissociation occurred. This mechanism could be regarded a kind of bifunctional mechanism or co-catalyst system. Since $OH^-$ was produced by water dissociation, an interaction between $OH^-$ and $M(OH)_2$/MOOH was important, and thus metal-oxygen binding strength was a descriptor in HER activity. They also conducted bulk-CO oxidation on $M(OH)_2$/MOOH deposited Pt surface and obtained the same trend of CO oxidation activity which could be explained by bifunctional effect ($Pt\text{-}CO_{ad}$ + MO(OH) + OH- -> Pt + M-OH + $HCO^{3-}$). Thus, metal-oxygen binding strength seemed to be a reasonable descriptor for the electrochemistry in alkaline media and $Ni(OH)_2$ was considered as a material at the top of bifunctional effect. Together with this report, additional cationic effect, bifunctionality of $Ni(OH)_2$/other metal substrate, and practical approach to controlling the morphology of $Ni(OH)_2$ and Pt substrate were reported.[36-38]

In the previous chapters, oxophilic effect in Pt nanocatalysts was investigated without the presence of electronic effect by using blended catalysts in

acid media. In this chapter, further studies on oxophilic effect in alkaline media were performed. By keen electrochemical measurements on CO oxidation, oxygen evolution, and hydrogen evolution and physicochemical characterizations, long-range oxophilic interactions between Pt nanoparticles and various water dissociation catalysts through electrolyte was verified in the blended catalysts system. Furthermore, in-depth discussion on the effect of metal-oxygen interaction on oxophilic effects was carried out.

## 4.2 Experimental section

### 4.2.1. Preparation of electrocatalysts

For the electrochemical and physicochemical analyses, iridium (IV) oxide dihydrate (99.99% $IrO_xH_y$, Alfa Aesar) were used as received and Ni, Co, and Fe (oxy)hydroxides were synthesized by modified method of the previous report.[39] To synthesize $Ni(OH)_2$, 25 ml of NaOH aqueous solution (0.2 M) was added dropwisely into 50 ml of $NiCl_2$ solution (2 mmol of $NiCl_2 \cdot 6H_2O$ dissolved in 50 ml of $H_2O$) which was heated to 65 °C with vigorous stirring. During the process, argon was purged through the solution to remove dissolved air. The mixture was further aged for 12 hours. After that, the reacted solution was centrifuged and washed several times with $H_2O$ and ethanol and dried at 60 °C under vacuum. For the synthesis of $Co(OH)_2$ and FeOOH, the metal precursor was replaced with $CoCl_2 \cdot 6H_2O$ and $FeSO_4 \cdot 7H_2O$ respectively. In particular, in the case of FeOOH, 2 ml of 30% $H_2O_2$ solution was added to the reaction mixture containing $Fe(OH)_2$, which led to the oxidation of $Fe^{2+}$ into $Fe^{3+}$ to make FeOOH. The as-received and sythesized oxides were mixed with 5 wt% Nafion® ionomer (Sigma-Aldrich, added as a binder) and isopropanol (Sigma-Aldrich), and subsequently stirred and under ultrasonication for ink preparation of electrochemical characterization. In addition, blended catalyst inks were prepared by mixing Pt/C (40 wt% of

equivalent Pt weight, Johnson Matthey), 5 wt% Nafion® ionomer (Sigma-Aldrich, added as a binder), isopropanol (Sigma-Aldrich) and as-received oxide hydrate or the annealed oxide. As a control sample, conventional catalyst ink composed of Pt/C, Nafion® ionomer, and IPA was also prepared. After vigorous stirring and sonication, 3 μL of catalyst ink was dropped onto a glassy carbon substrate (geometric surface area: 0.196 $cm^2$).

### 4.2.2. Physical characterizations

The morphologies of metal oxide (hydrate), metal (oxy)hydroxide and the structures of blended catalysts were characterized by transmission electron microscopy (TEM; JEOL JEM 2100 used) equipped with an energy dispersive spectroscopy (EDS) accessary. The crystalline structure of the oxide materials were analyzed using X-ray diffraction (XRD; Rigaku D/MAX 2500 used) with Cu Kα radiation source. The core level X-ray photoelectron spectroscopy (XPS) of O 1s spectra of metal oxide hydrate and metal (oxy)hydroxide were recorded by 8A1 beamline of PAL (U7-undulator radiation) and KRATOS AXIS-HSi (Al Kα radiation source), respectively. The results were analyzed by using XPSPEAK41 software. In addition, Pt 4f electronic structures of the blended catalysts were also examined by XPS (KRATOS AXIS-His, Al Kα radiation source).

### 4.2.3. Electrochemical measurements

Electrochemical measurements were carried out by using a potentiostat (PGSTAT101, Autolab) based on a conventional three-electrode electrochemical cell comprising a glassy carbon (working electrode), a saturated calomel electrode (reference electrode), and a platinum wire for oxygen evolution reaction (OER), CO bulk oxidation and a graphite rod for hydrogen evolution reaction (HER) (counter electrode), respectively. 0.1 M KOH was used as an electrolyte in this chapter. Cyclic voltammetry (CV) was performed in an electrochemical cell within

the potential range of 0.05−1.05 V vs. reversible hydrogen electrode (RHE) with the scan rate of 20 mV/s. HER polarization curves were measured in an electrochemical cell within the potential range of -0.4 to 0.2 V vs. RHE with the scan rate of 20 mV/s and rotation at 2000 rpm, and $H_2$ was continuously purged into the solution during the measurement. OER polarization curves were measured in an electrochemical cell within the potential range of 1.0 to 1.8 V vs. RHE with the scan rate of 5 mV/s and rotation at 1600 rpm, and $O_2$ was continuously purged into the solution during the measurement. For the measurement of OER, 12 wt.% of Vulcan carbon was blended in order to exclude conductivity problems of $NiO_xH_y$, $CoO_xH_y$, and $FeO_xH_y$. CO bulk oxidation measurments were performed in potential range of 0.05−1.05 V vs. RHE with 5 mV/s scan rate, continuous CO gas feeds, and rotation at 1600 rpm. All electrochemical measurements were performed at 20 °C which was controlled by a thermostat and a circulating jacket.

## 4.3 Results and discussion

### 4.3.1. Linkage blended system to electrodeposited-substrate system

In 2012, Markovic and his co-workers reported the trends of oxophilic effect in alkaline media by investigations on CO oxidation, OER, and HER using electrodeposited Ni, Co, Fe, and Mn (oxy)hydroxide on Pt (111) substrate, and the trend in enhancement of performances induced by the oxophilic effect was correlated with metal-hydroxyl binding strength.[35] In order to extend the understandings on the oxophilic effect present in the blended catalysts and compare oxophilic effect in the blended system with that in the previous work by Markovic, Ni, Co and Fe (oxy)hydroxide particles were synthesized by a modified procedure of a recently reported method.[39] Figure 4.1 shows the TEM images of the hydrous Ir oxide ($IrO_xH_y$, Figures 4.1a and 4.1b), Ni hydroxide ($NiO_xH_y$, Figures 4.1c and 4.1d), Co hydroxide ($CoO_xH_y$, Figures 4.1e and 4.1f), and Fe oxyhydroxide ($FeO_xH_y$, Figures 4.1g and 4.1h), and disordered nanostructures were observable in

all cases. It was notable that $NiO_xH_y$, $CoO_xH_y$, and $FeO_xH_y$ had crystalline properties (lattice spacing depicted in high-magnification images) while $IrO_xH_y$ was amorphous. Then the synthesized (oxy)hydroxides were characterized by XRD measurements (Figure 4.2), and they were confirmed as $Ni(OH)_2$, $Co(OH)_2$ and FeOOH by comparison with JCPDS 14-0117, JCPDS 45-0031, and JCPDS 13-0087, respectively. Meanwhile, though $IrO_xH_y$ used in the previous chapter was also utilized in this study for a more generalized comparison, $RuO_xH_y$ was neglected in this chapter due to its unstable nature in alkaline electrolyte (Figure 4.3). The blended catalysts for alkaline electrocatalysis were prepared by uniformly mixing Pt/C with $IrO_xH_y$, $NiO_xH_y$, $CoO_xH_y$, or $FeO_xH_y$. Figure 4.4 to Figure 4.7 show the TEM analyses results of the blended catalysts, and well-dispersed Pt/C and $MO_xH_y$s were clearly observable from the elemental energy dispersive spectroscopy (EDS) mapping results.

Figure 4.8 shows the cyclic voltammetry (CV) diagrams of the blended catalysts, which were measured for the investigations on the basic electrochemical property of the blended catalysts in alkaline media. There was a noteworthy observation that Pt/C_$IrO_xH_y$ and the other three blends manifested a different electrochemical behavior. In the case of Pt/C_$IrO_xH_y$, current densities were increased when $IrO_xH_y$ was added to bare Pt/C. In contrast, decrease in currents was resulted from the incorporation of $NiO_xH_y$, $CoO_xH_y$, or $FeO_xH_y$, especially in the $OH^-$ adsorption/desorption potential region. This indicates that site blocking at the Pt surface is present in the blends of Pt/C and 3d transition metal (oxy)hydroxides, implying a stronger interaction between these (oxy)hydroxides and Pt/C compared to that between Pt/C and $IrO_xH_y$ in Pt/C_$IrO_xH_y$. In addition, degree of decrease in current density at $OH^-$ adsorption/desorption region was the largest in $FeO_xH_y$ followed by $CoO_xH_y$ and $NiO_xH_y$, and this order matched with the differences in standard reduction potentials between Pt and the corresponding 3d transition metals, suggesting that the changes in electrochemical behavior result

from the charge interactions. Nevertheless, as can be expected from the negligible portion of Pt nanoparticles that form direct contact with the oxyhydroxide (confirmed from the TEM analyses), electronic structures of Pt nanocatalysts did not show any notable change, as can be clearly seen from the XPS Pt 4f spectra depicted in Figure 4.9.

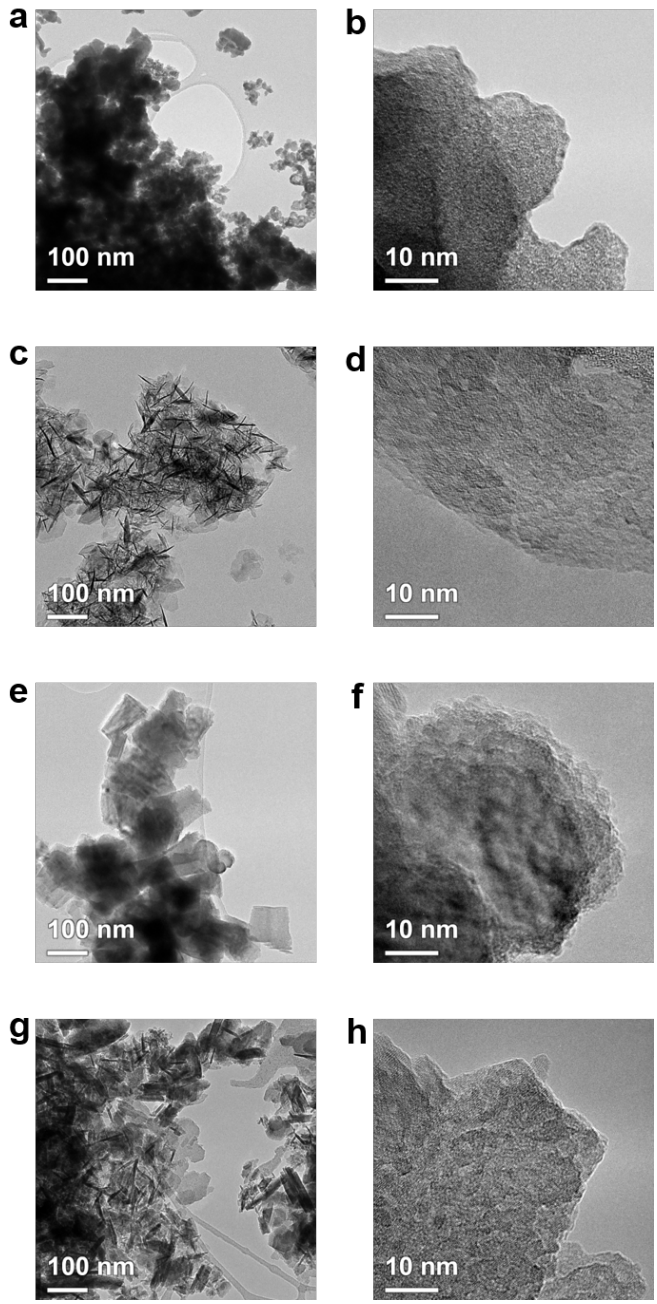


**Figure 4.1.** Transmission electron microscopy (TEM) images of (a,b) $IrO_xH_y$, (c,d) $NiO_xH_y$, (e,f) $CoO_xH_y$, and (g,h) $FeO_xH_y$.

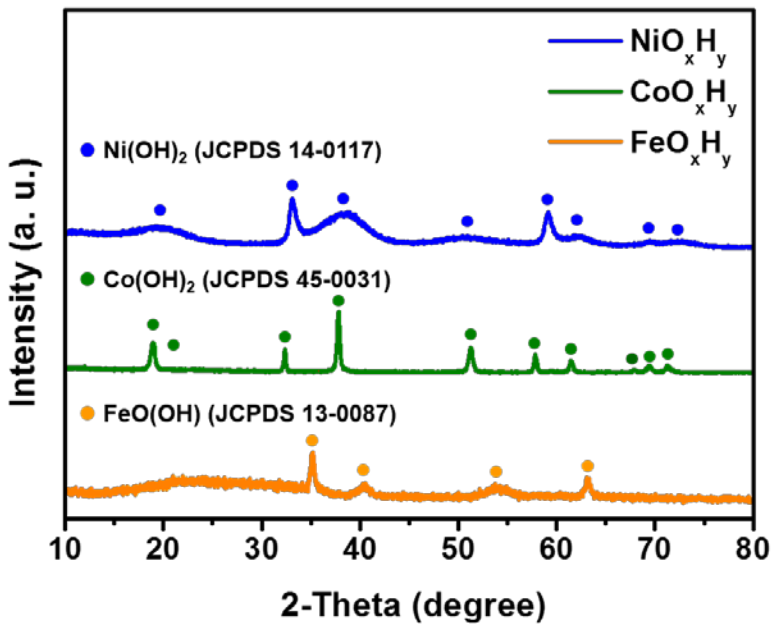


**Figure 4.2.** X-ray diffraction (XRD) patterns of $NiO_xH_y$, $CoO_xH_y$, and $FeO_xH_y$.

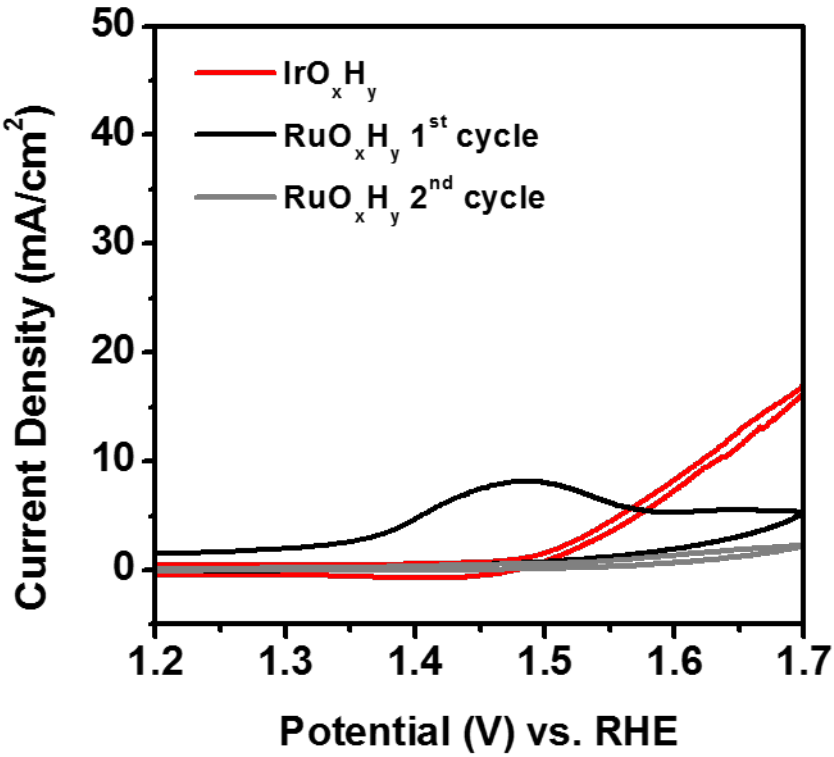


**Figure 4.3.** Oxygen evolution reaction (OER) polarization curves for $RuO_xH_y$ and $IrO_xH_y$ in 0.1 M KOH with rotation at 1600 rpm.

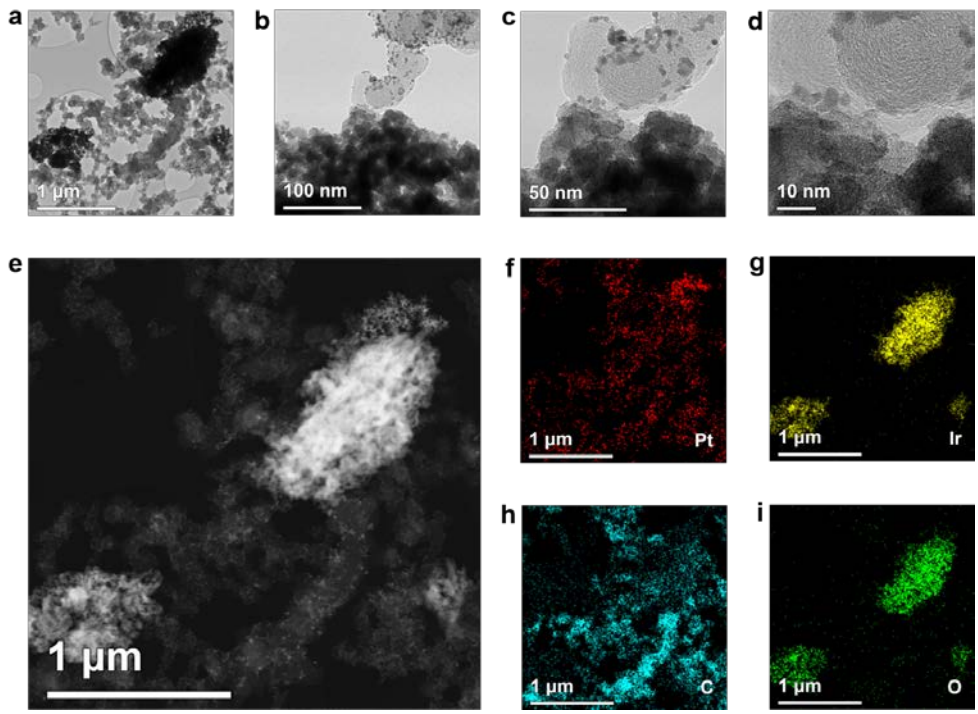


**Figure 4.4.** (a-d) TEM images of the blended catalyst comprising Pt/C and $IrO_xH_y$ at various magnifications. (e) STEM image of the blended catalyst and (f-i) the corresponding elemental EDS maps of (f) Pt, (g) Ir, (h) C, and (i) O.

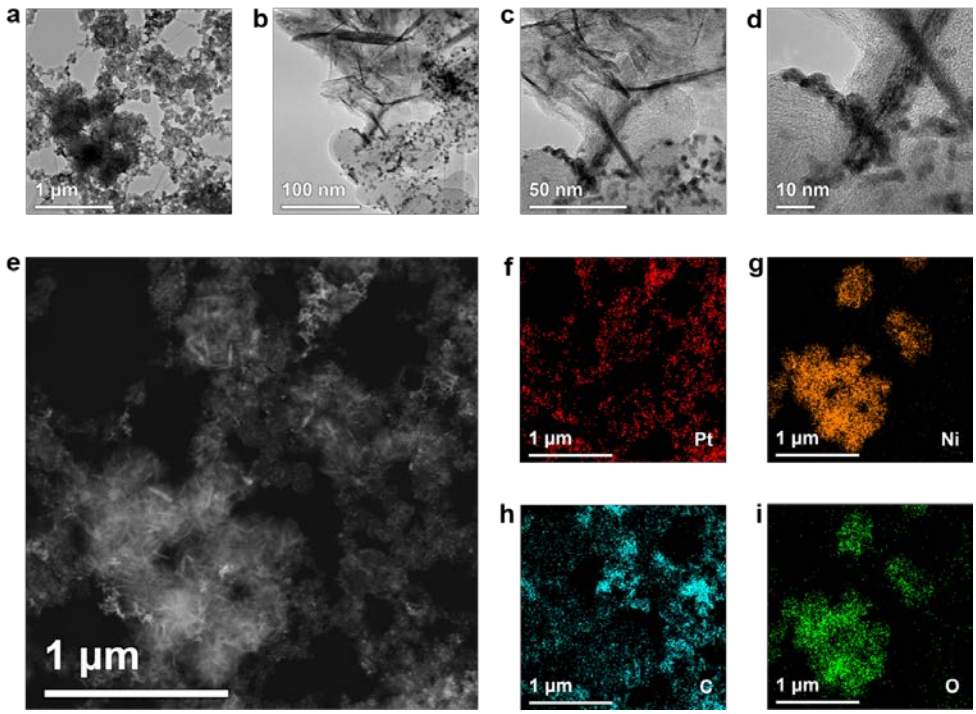


**Figure 4.5.** (a-d) TEM images of the blended catalyst comprising Pt/C and $NiO_xH_y$ at various magnifications. (e) STEM image of the blended catalyst and (f-i) the corresponding elemental EDS maps of (f) Pt, (g) Ni, (h) C, and (i) O.

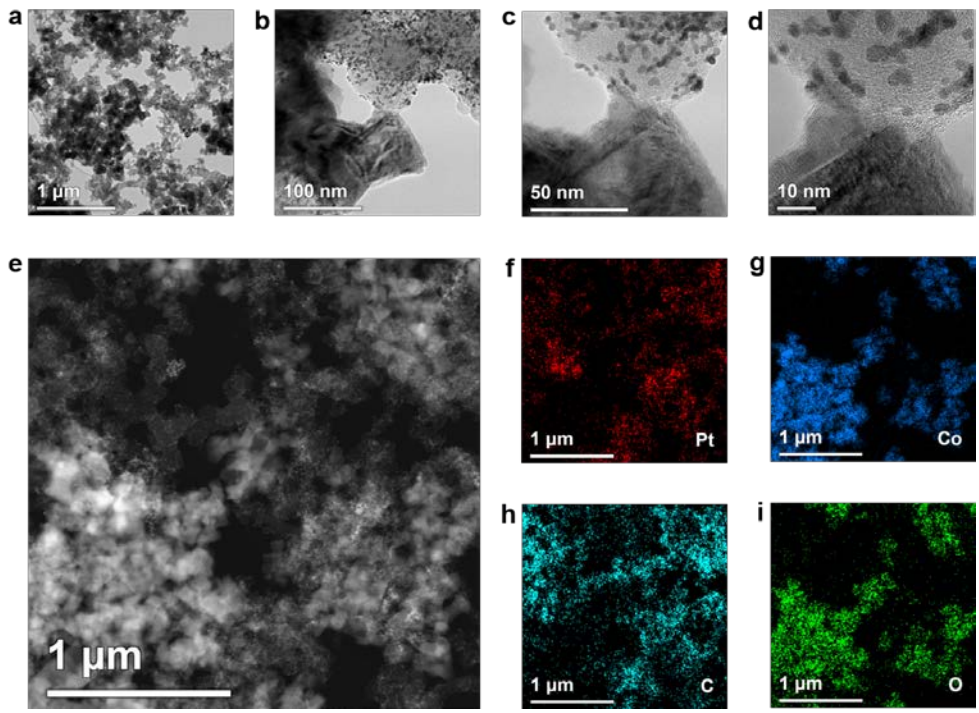


**Figure 4.6.** (a-d) TEM images of the blended catalyst comprising Pt/C and $CoO_xH_y$ at various magnifications. (e) STEM image of the blended catalyst and (f-i) the corresponding elemental EDS maps of (f) Pt, (g) Co, (h) C, and (i) O.

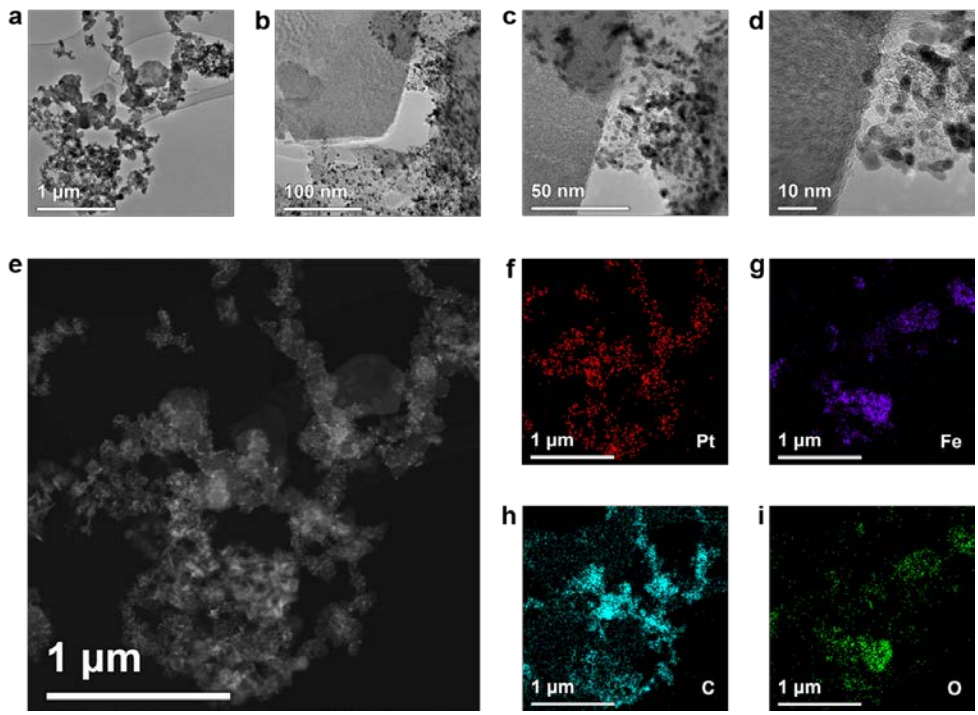


**Figure 4.7.** (a-d) TEM images of the blended catalyst comprising Pt/C and $FeO_xH_y$ at various magnifications. (e) STEM image of the blended catalyst and (f-i) the corresponding elemental EDS maps of (f) Pt, (g) Fe, (h) C, and (i) O.

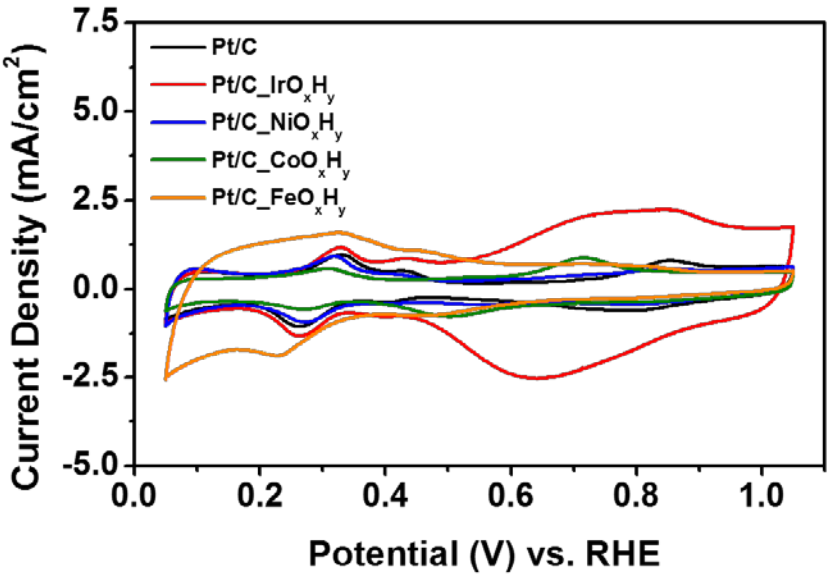


**Figure 4.8.** Cyclic voltammetry (CV) diagrams of the bare Pt/C and the blended catalysts measured in 0.1 M KOH.

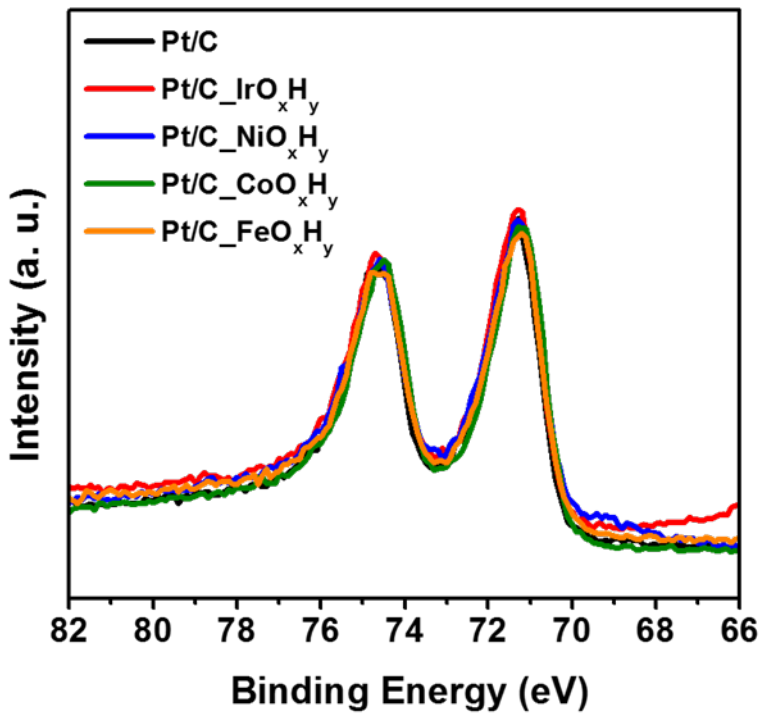


**Figure 4.9.** X-ray photoelectron spectroscopy (XPS) Pt 4f spectra of bare Pt/C and the blended catalysts.

### 4.3.3. Oxophilic effect in alkaline medium

Prior to the electrochemical investigations on the oxophilic effect in blended catalysts, XPS O 1s spectra of $MO_xH_y$s were obtained in order to compare the degree of interaction between metal and oxygen (Figure 4.10). For quantitative evaluations, mean binding energy position was selected to represent the degree of interaction, and these values were depicted in Figure 4.10. Since a lower binding energy position indicates larger interaction between metal and oxygen, it could be verified that $FeO_xH_y$ followed by $CoO_xH_y$, $NiO_xH_y$, and $IrO_xH_y$ has the strongest interaction, and this trend well matched with the previous report and also with the differences in standard reduction potentials. In addition, the XPS O 1s spectra were deconvoluted into 3 peaks according to the criterion used in the previous chapter. Figure 4.11 displays the fitted curves of O 1s spectra and Table 4.1 shows the areal ratio obtained from the fitted results.

In order to understand the effect of oxophilicity in alkaline media, OER polarization curves of $IrO_xH_y$, $NiO_xH_y$, $CoO_xH_y$, and $FeO_xH_y$ were obtained by electrochemical measurements in 0.1 M KOH, and the results are displayed in Figure 4.12a. In alkaline electrolyte, $IrO_xH_y$ showed the highest performance followed by $NiO_xH_y$, $CoO_xH_y$, and $FeO_xH_y$. In order to address the origin of activity trend in OER, the electrocatalytic activities represented by the potential values at 10 $mA/cm^2$ of OER current density were compared with the mean binding energy position in XPS O 1s spectra of $MO_xH_y$ catalysts, and a linear correlation was observable (Figure 4.12b). This result well matched with the previous work reported by Markovic and his co-workers, wherein the degree of metal-oxygen interaction was suggested as the descriptor for oxophilicity and OER activity.[35] Since the $MO_xH_y$ with stronger electronic interaction between metal and oxygen (lower binding energy position in O 1s) shows lower activity in OER, we could conclude that the trends in OER performance can be understood as the result of differences in oxophilicity of metal in the $MO_xH_y$s. The OER activities were also

compared with the portion of different types of oxygen obtained from XPS analyses, but no clear relationship was observable (Figure 4.13).

Figure 4.14a shows the HER polarization curves of blended catalysts, and it was notable to observe that the trend in HER performances was in line with the OER activity in the case of Pt/C_$NiO_xH_y$, Pt/C_$CoO_xH_y$, and Pt/C_$FeO_xH_y$, but a relatively small enhancement was observable in Pt/C_$IrO_xH_y$. This separation in trend matched with the CV analysis results in Figure 4.8, and it was thereby understood as the result of difference in the degree of interactions between Pt/C and $MO_xH_y$s. Figure 4.14b shows the Tafel plots and Tafel slopes obtained in the kinetic current region by linear fittings based on the Tafel equation ($\eta = b \log( j ) + a$). Compared to bare Pt/C, all of the blended catalysts exhibited smaller Tafel slopes. Since the lack of electronic effect was verified by the XPS measurements in Figure 4.9, the origin of enhanced HER activities was expected to be the oxophilic property of $MO_xH_y$, which is further discussed below.

Then the HER activities (represented by potential at -10 $mA/cm^2$) and Tafel slopes of the blended catalysts were compared with the portion of defective oxygen in $MO_xH_y$s. Figure 4.15 shows the plot of HER activity vs. portion of three different types of oxygen, and linear correlation was observable in the case of defective oxygen (Figure 4.15b), while it was unable to find linearity when the HER performances were compared with the portion of oxygen bound to metal (Figure 4.15a) or that of adsorbed oxygen (Figure 4.15c). The linear correlation was also observed in the relationship between the Tafel slopes and portion of defective oxygen (Figure 4.15e), though there was no notable tendency in the cases of other types of oxygen (Figures 4.15d and 4.15f). From these results, importance of defective oxygen for water dissociation in alkaline media was clearly verified.

For a more clear understandings on the oxophilic effect in blended catalysts, bulk CO oxidations were performed in 0.1 M KOH solution, and the results are displayed in Figure 4.16a. It was notable to observe that the trend in CO

oxidation performances was opposite from that in OER activity. By comparisons between CO oxidation performances (represented by the half-wave potentials of CO oxidation), metal-oxygen interaction in $MO_xH_y$s (represented by mean binding energy position of XPS O 1s spectra), and OER activity of $MO_xH_y$s (represented by the potentials at 10 $mA/cm^2$ of OER current density), direct and inverse proportional linear correlations were observed in CO oxidation activity vs. metal-oxygen interaction and CO oxidation activity vs. OER activity as shown in Figure 4.16b and 4.16c, respectively. This trend is opposite from that reported in the previous literature by Markovic and his co-workers, wherein an electrodeposited metal hydroxide on Pt (111) substrate with smaller oxophilicity resulted in a higher CO oxidation performance. The difference in trend can be explained by the key difference between my system and the previous one. In Markovic's work, all of the metal hydroxides that were deposited onto Pt as nano-islands were in direct contact with Pt. Therefore, –OH formed on the surface of metal hydroxides could directly react with CO adsorbed on Pt surfaces. Because desorption of oxygen species limit the OER and also CO oxidation in conventional bifunctional catalysts, a higher CO oxidation activity was observed in the case of metal hydroxide with a weaker metal-oxygen binding strength.[35] However, in blended catalysts, negligible portion of Pt nanocatalysts is in direct contact with metal (oxy)hydroxide, and therefore the reaction between –OH on $MO_xH_y$ and CO adsorbed on Pt is incomparably small when compared with the electrodeposited hydroxides on Pt substrate.

Based on the experimental observations discussed above and diversity between the blended catalysts and the previous metal hydroxide/Pt substrate system, the trend in CO oxidation in blended catalysts can be understood as follows; from the significant difference in CO oxidation activity between the blended catalysts containing $IrO_xH_y$ and 3d transition metal (oxy)hydroxides, the major reason for the enhanced performance is ascribable to the charge interactions discussed in Figure 4.8. Meanwhile, the trend in Pt_$NiO_xH_y$, Pt_$CoO_xH_y$, and

Pt_$FeO_xH_y$ can be explained by the tendency for –OH formation on the surface of hydrous oxides, which may further induce fluctuations in O-H bond strength through the chains of water molecules connected by O-H bonds and hydrogen bonds. From the CV diagrams (Figure 4.8) and degree of metal-oxygen interactions observed by the position of XPS O 1s spectra (Figure 4.10), it could be clearly figured out that the formation of –OH is most preferred in $FeO_xH_y$ followed by $CoO_xH_y$ and $NiO_xH_y$. Due to the long-range tuning of oxophilicity, –OH formation on Pt surface is facilitated by the formation of –OH on the surface of $MO_xH_y$, and consequently accelerate the CO oxidation by Langmuir-Hinshelwood reaction between –OH and –CO on the surface of Pt nanocatalysts. From this interpretation, it could be concluded that the opposite trend in CO oxidation strongly supports long-range oxophilic interaction in the blended catalysts for not only in the case of alkaline electrocatalysis but also for that of electrocatalytic reactions in acidic media, which was investigated in the last chapter.

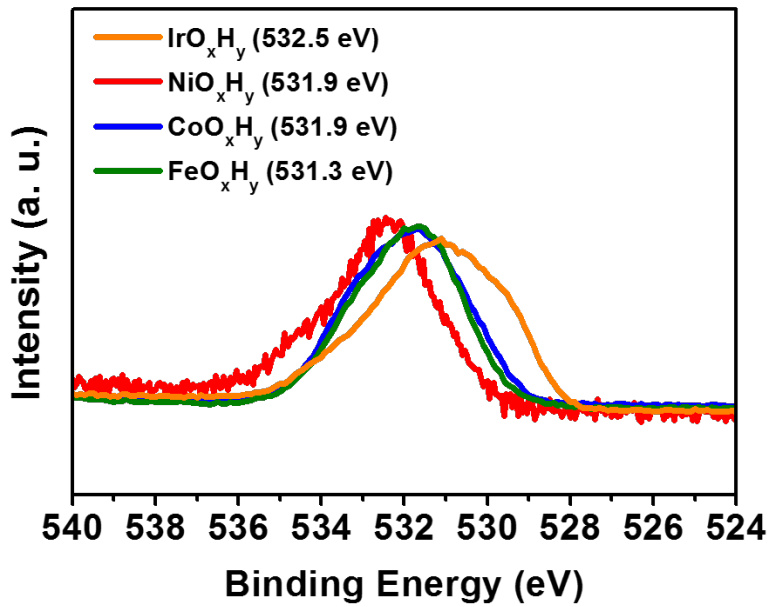


**Figure 4.10.** X-ray photoelectron spectroscopy (XPS) O 1s spectra of $MO_xH_y$.

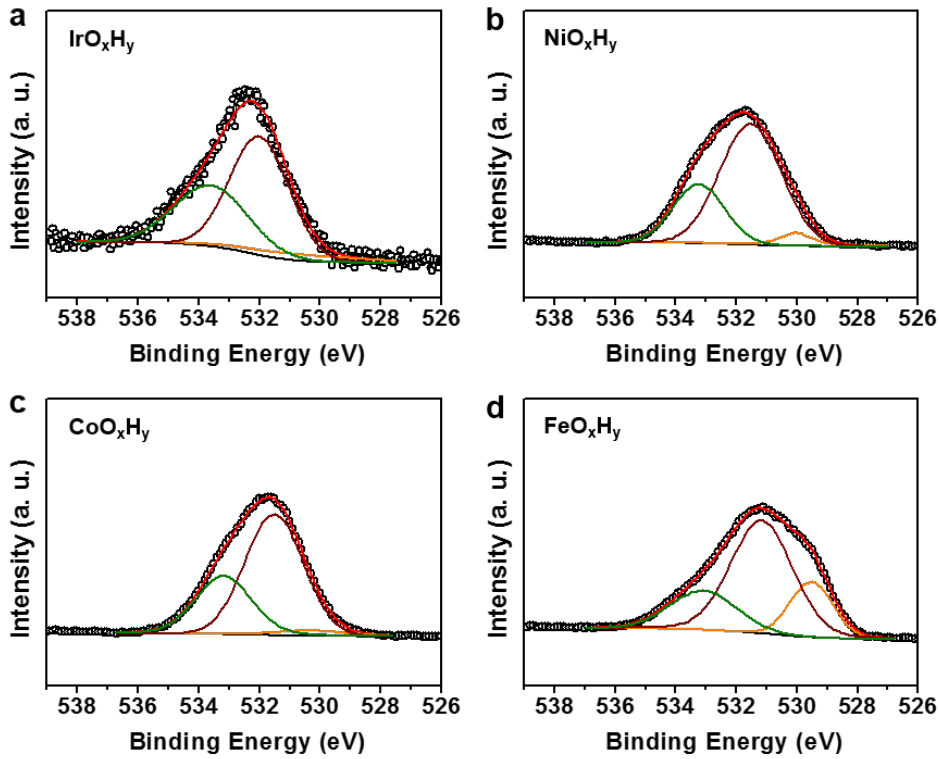


**Figure 4.11.** X-ray photoelectron spectroscopy (XPS) results of $MO_xH_y$s obtained at O 1s core level and the fitted curves.

| | Areal Ratio (%) | | |
|---|---|---|---|
| | O1 | O2 | O3 |
| $IrO_xH_y$ | 6.71 | 56.81 | 36.48 |
| $NiO_xH_y$ | 5.23 | 66.97 | 27.80 |
| $CoO_xH_y$ | 3.93 | 64.15 | 31.92 |
| $FeO_xH_y$ | 19.28 | 59.39 | 21.33 |

**Table 4.1.** Fitted results of the O 1s XPS spectra of $MO_xH_y$s displayed in Figure 4.11.

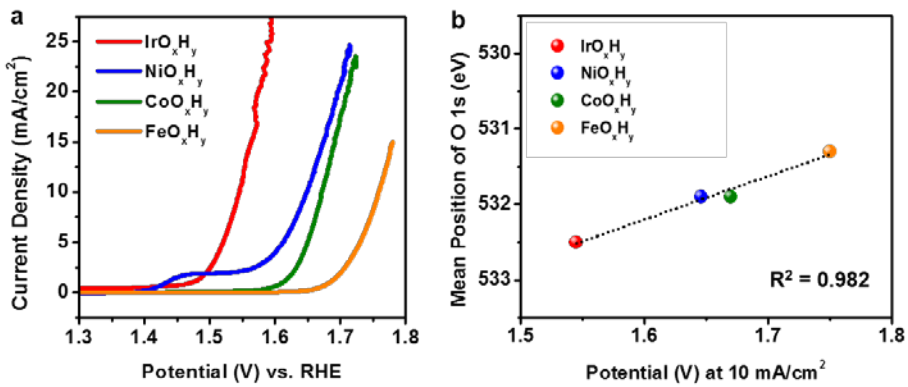


**Figure 4.12.** iR-corrected oxygen evolution reaction (OER) polarizations curves for $MO_xH_y$s in 0.1 M KOH electrolyte with rotation at 1600 rpm. (b) Comparison between potential values at 10 mA/cm$^2$ of oxygen evolution currents and mean binding energy positions of O 1s XPS spectra.

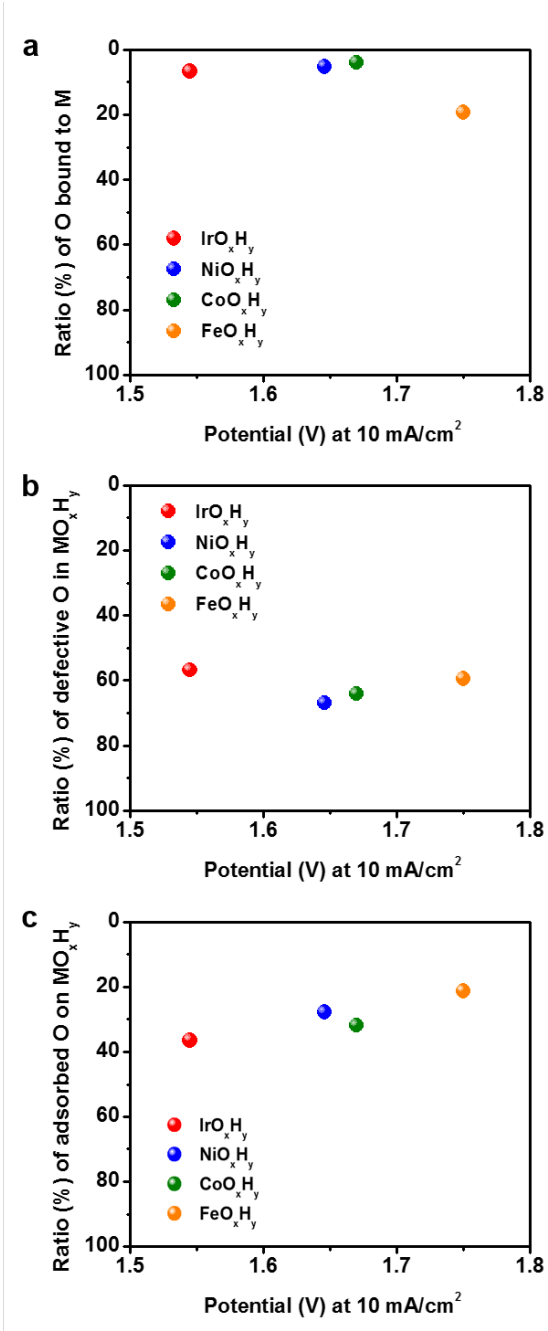


**Figure 4.13.** Comparisons between OER activities of $MO_xH_y$s (represented by the potential values at 10 mA/cm$^2$) and portions of three different types of oxygen obtained by XPS analyses. (a) O1, (b) O2, and (c) O3.

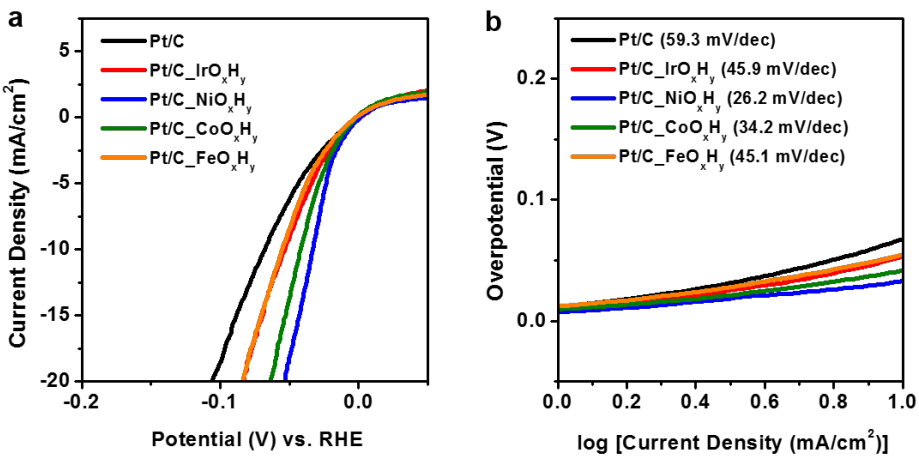


**Figure 4.14.** (a) iR-corrected hydrogen evolution reaction (HER) polarizations curves for bare Pt/C and the blended catalysts in 0.1 M KOH with rotation at 2000 rpm. (b) Tafel plots of the bare Pt/C and the blended catalysts and the Tafel slopes obtained by the linear fittings based on the Tafel equation.

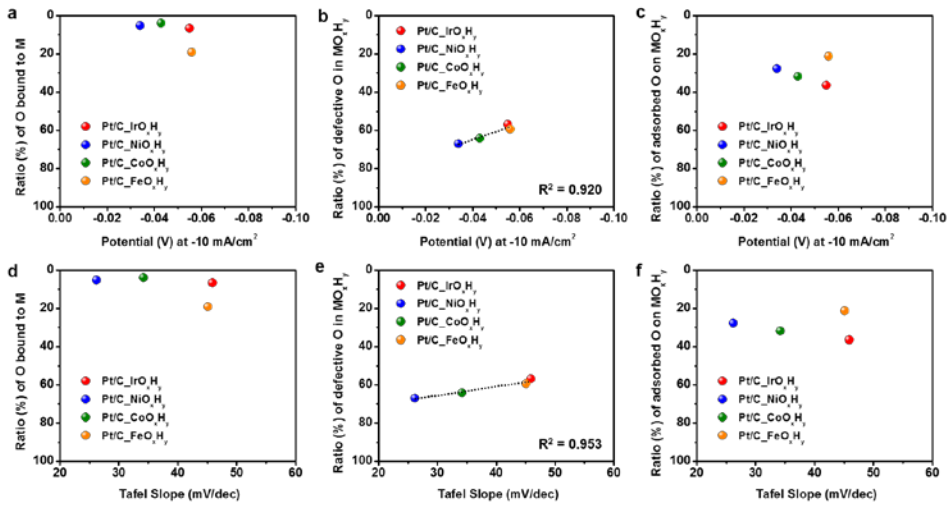


**Figure 4.15.** Comparisons between HER activities of $MO_xH_y$s represented by (a-c) the potential values at 10 mA/cm$^2$ and (d-f) the Tafel slopes and portions of three different types of oxygen obtained by XPS analyses. (a,d) O1, (b,e) O2, and (c,f) O3.

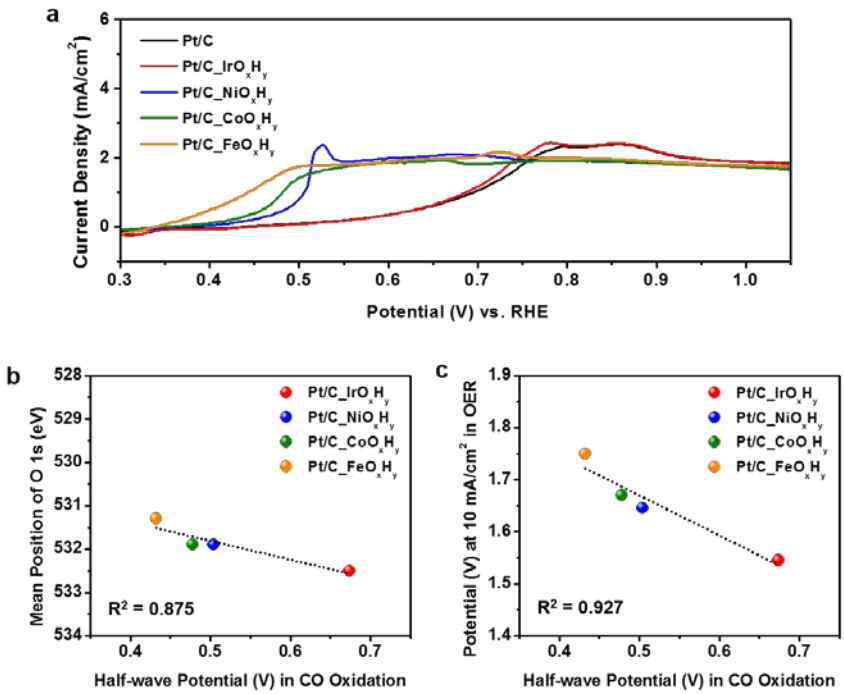


**Figure 4.16.** (a) Background-corrected bulk CO oxidation results of the blended catalysts measured in CO saturated 0.5 M $H_2SO_4$ with rotation at 1600 rpm. (b,c) Comparisons of CO oxidation performances of the blended catalysts (represented by the potential values at the first half-maximum of the CO oxidation peaks with (b) mean binding energy position of XPS O 1s spectra of $MO_xH_y$s and (c) OER activities of the $MO_xH_y$s (represented by the potential values at OER current density of 10 mA/cm$^2$).

## 4.4. Conclusions

In this chapter, investigations on the oxophilic effect in the blended catalysts were performed in alkaline media by using hydrous Ir oxide and 3d transition metal (oxy)hydroxides. By keen electrochemical measurements, trends in the degree of interaction between Pt nanocatalysts and hydrous oxides were observed, and their dependence on the difference in standard reduction potential (oxidation tendency) was verified. In addition, importance of metal-oxygen interaction strength on OER activity was experimentally confirmed based on the XPS analyses, in addition to the linear correlation between the portion of defective oxygen and water dissociation property. Finally, oxophilic effects in the blended catalysts were investigated by CO oxidation, and the presence of long-range bifunctional effect via the interactions through electrolyte was discussed based on the opposite trend in CO oxidation performances compared to the previous work. The investigations performed in this chapter clearly shows the nature of oxophilic effect in alkaline electrolyte, and therefore this work is anticipated to bring advances to the catalyst design for various electrochemical reactions in alkaline media.

## 4.5. References


[1] Ge, X.; Sumboja, A.; Wuu, D.; An, T.; Li, B.; Thomas Goh, F. W.; Andy Hor, T. S.; Zong, Y.; Liu, Z., *ACS Catal.* **2015**, *5*, 4643−4667.

[2] Ramaswamy, N.; Mukerjee, S. *Adv. Phys. Chem.* **2012**, *2012*, 1−17.

[3] Ramaswamy, N.; Mukerjee, *J. Phys. Chem. C* **2011**, *115*, 18015−18026.

[4] Jiao, Y.; Zheng, Y.; Jaroniec, M.; Qiao, S. Z. *Chem. Soc. Rev.* **2015**, *44*, 2060−2086.

[5] Suen, N.-T.; Hung, S.-F.; Quan, Q.; Zhang, N.; Xu, Y.-J.; Chen. H. M. *Chem. Soc. Rev.* **2017**, *46*, 337−365.

[6] Wu, G.; More, K. L.; Johnston, C. M.; Zelenay, P. *Science* **2011,** *332*, 443−447.

[7] Yang, W.; Fellinger, T.-P.; Antonietti, M. *J. Am. Chem. Soc.* **2011,** *133*, 206−209.

[8] Gong, K.; Du, F.; Xia, Z.; Durstock, M.; Dai, L. *Science* **2009,** *323*, 760−764.

[9] Nagaiah, T. C.; Kundu, S.; Bron, M.; Muhler, M.; Schuhmann, W. *Electrochem. Commun.* **2010,** *12*, 338−341.

[10] Chung, H. T.; Won, J. H.; Zelenay, P. *Nat. Commun*. **2013**, *4*, 1922.

[11] Chen, R.; Li, H.; Chu, D.; Wang, G. *J. Phys. Chem. C* **2009,** *113*, 20689−20697.

[12] Burke, M. S.; Enman, L. J.; Batchellor, A. S.; Zou, S.; Boettcher, S. W. *Chem. Mater.* **2015**, *27*, 7549−7558.

[13] Gorlin, Y.; Jaramillo, T. F. *J. Am. Chem. Soc.* **2010,** *132*, 13612−13614.

[14] Liang, Y.; Wang, H.; Zhou, J.; Li, Y.; Wang, J.; Regier, T.; Dai, H. *J. Am. Chem. Soc.* **2012**, *134*, 3517−3523.

[15] Pickrahn, K. L.; Park, S. W.; Gorlin, Y.; Lee, H.-B.-R.; Jaramillo, T. F.; Bent, S. F. *Adv. Energy Mater.* **2012**, *2*, 1269−1277.

[16] Arges, C. G.; Ramani V.; Pintauro, P. N. *Electrochem. Soc. Interface* **2010**, *19*, 31−35.

[17] Zhang, F.; Zhang, H.; Qu, C. *J. Mater. Chem.* **2011**, *21*, 12744−12752.

[18] Jin, H.; Wang, J.; Su, D.; Wei, Z.; Pang, Z.; Wang, Y. *J. Am. Chem. Soc.* **2015**, *137*, 2688−2694.

[19] Liu, X.; Wang, X.; Yuan, X.; Dong, W.; Huang, F. *J. Mater. Chem. A* **2016**, *4*, 167−172.

[20] Zeng, K.; Zhang, D. *Prog. Energy Combust. Sci.* **2010**, *36*, 307−326.

[21] Varcoe, J. R.; Slade, R. C. T.; *Fuel Cells* **2005**, *5*, 187−200.

[22] Matsumoto, K.; Fujigaya, T.; Yanagi, H.; Nakashima, N. *Adv. Funct. Mater.* **2011**, *21*, 1089−1094.

[23] Zou, X.; Zhang, Y. *Chem. Soc. Rev.* **2015**, *44*, 5148−5180.

[24] Sheng, W.; Gasteiger, H. A.; Shao-Horn, Y. *J. Electrochem. Soc.* **2010**, *157*, B1529−B1536.

[25] Subbaraman, R.; Danilovic, N.; Lopes, P. P.; Tripkovic, D.; Strmcnik, D.; Stamenkovic, V. R.; Markovic, N. M. *J. Phys. Chem. C* **2012**, *116*, 22231−22237.

[26] Zheng, J.; Sheng, W.; Zhuang, Z.; Xu, B.; Yan, Y., *Sci. Adv.* **2016**, *2*, e1501602.

[27] Durst, J.; Siebel, A.; Hasché, F.; Herranz, J.; Gasteiger, H. A. Energy Environ. Sci. 2014, 7, 2255−2260.

[28] Rheinländer, P. J.; Herranz, J.; Durst, J.; Gasteiger, H. A. *J. Electrochem. Soc.* **2014**, *161*, F1448−F1457.

[29] Lu, S.; Zhuang, Z. *J. Am. Chem. Soc*. **2017**, *139*, 5156−5163.

[30] Wang, Y.; Wang, G.; Li, G.; Huang, B.; Pan, J.; Liu, Q.; Han, J.; Xiao, L.; Lu, J.; Zhuang, L. *Energy Environ. Sci.* **2015**, *8*, 177−181.

[31] Stamenkovic, V. R.; Strmcnik, D.; Lopes, P. P.; Markovic, N. M. *Nat. Mater.* **2017**, *16*, 57–69.

[32] Strmcnik, D.; Uchimura, M.; Wang, C.; Subbaraman, R.; Danilovic, N.; van der Vliet, D.; Paulikas, A. P.; Stamenkovic, V. R.; Markovic, N. M. *Nat. Chem.* **2013**, *5*, 300–306.

[33] Koper, M. T. M. *Nat. Chem.* **2013**, *5*, 255–256.

[34] Subbaraman, R.; Tripkovic, D.; Strmcnik, D.; Chang, K.-C.; Uchimura, M.;

Paulikas, A. P.; Stamenkovic, V.; Markovic, N. M. *Science*, **2011**, *334*, 1256–1260.

[35] Subbaraman, R.; Tripkovic, D.; Chang, K.-C.; Strmcnik, D.; Paulikas, A. P.; Hirunsit, P.; Chan, M.; Greely, J.; Stamenkovic, V.; Markovic, N. M. *Nat. Mater.* **2012**, *11*, 550–557.

[36] Danilovic, N.; Subbaraman, R.; Strmcnik, D.; Chang, K.-C.; Paulikas, A. P.; Stamenkovic, V.; Markovic, N. M. *Angew, Chem. Int. Ed.* **2012**, *51*, 12495–12498.

[37] Wang, L.; Lin, C.; Huang, D.; Chen, J.; Jiang, L.; Wang, M.; Chi, L.; Shi, L.; Jin, J. *ACS Catal.* **2015**, *5*, 3801–3806.

[38] Yin, H.; Zhao, S.; Zhao, K.; Muqsit, A.; Tang, H.; Chang, L.; Zhao, H.; Gao, Y.; Tang, Z. *Nat. Commun.* **2015**, *6*. 6430.

[39] Lee, D. J.; Yu, S.-H.; Lee, H. S.; Jin, A.; Lee, J.; Lee, J. E.; Sung, Y.-E.; Hyeon, T. *J. Mater. Chem. A* **2017**, *5*, 8744–8751.

# 국문초록

수계 전기 촉매 반응은 일반적으로 전해질, 외부 회로, 양극 및 음극을 포함하는 전기 화학 장치에서 일어난다. 전류의 흐름에 따라 다음과 같이 두 종류의 장치로 나눠질 수 있다. (i) 자발적 산화 환원 반응에 의해 화학 에너지를 전기 에너지로 변환하는 고분자 전해질 막 연료 전지 및 (ii) 연료 생산을 위해 전기 에너지를 화학 에너지로 변환하는 물 전기 분해 장치이다. 산성 및 염기성 전해질에서의 수소 산화 및 발생, 산소 환원 및 발생 그리고 일산화탄소의 산화반응은 위 두 가지 유형의 전기 화학 장치에서 가장 중요한 반응이라고 할 수 있다. 이 논문에서는 이러한 전기 촉매 반응에 대한 백금 나노 촉매, 금속 (옥시) 수산화물 및 금속 산화물 (수화물)의 역할을 조사 하였다.

주로 백금 합금 촉매가 쓰이는 고분자 전해질 막 연료 전지 용 촉매의 개발에서, 주요 쟁점은 귀금속의 활성을 높이는 것과 동시에 그 사용량을 줄이는 것이다. 또한, 비 백금 계 촉매의 개발 및 백금 계 촉매의 활성 향상은 물 전기 분해 장치의 전극 촉매에 대한 주요한 연구 목적이라고 할 수 있다. 이에 따라 본 연구에서는 첨단 백금 나노 촉매가 금속 산화물 (수화물) 또는 금속 (옥시) 산화물과 혼합되어 일산화탄소 산화 및 수소 발생에서, 보다 향상된 활성을 호산소 효과를 통해 유도하고 향상된 산소 발생을 위해 금속 산화물 (수화물) 또는 금속 (옥시) 수산화물을 전극 물질로 사용하였다. 이러한 촉매 시스템의 전기 화학적 및 물리 화학적 관찰 결과, 백금 표면의 전자적 변화가 없는 호산소 효과가 산성 및 염기성 전해질에서의 전기 화학 반응에 중요한 영향을 미친다는 것을 확인하였다. 또한, 수계 전해질과 촉매 시스템 사이의

상호 작용은 호산소 효과를 촉진한다는 관찰을 통해, 그 결과 이 연구는 일반적으로 백금 합금 시스템에서 발생하는 호산소 효과를 이해하는 데에 도움이 될 수 있었다.

1장에서는 전기 촉매에 대한 기초, 고분자 전해질 막 연료 전지 및 물 전기 분해 장치 등에 대한 소개를 다루었다. 전기 촉매 반응 및 전류 흐름 방향에 따른 두 종류의 전기 화학 장치의 반응 속도론을 간략히 소개하고, 고분자 전해질 막 연료 전지의 전기 화학 반응, 백금 합금 촉매의 기초 및 기존에 보고 된 호산소 효과에 대한 연구를 소개하였다. 마지막으로, 물 전기 분해 장치에서의 전기 촉매 반응에 대한 소개를 진행하였고, 전기화학적 수소 발생에서 호산소 효과를 통해 가능한 개선점이 간략하게 논의되었다.

2장에서는 산성 전해질에서 백금 나노 촉매와 수화된 루테늄 산화물 사이의 호산소 효과에 대한 확장 된 개념이 논의되었다. 무시할 만한 정도의 직접 접합부를 가진 백금 나노 촉매와 수화된 루테늄 산화물 사이의 전기 촉매적 일산화탄소 산화 메커니즘 및 호산소 효과를 조사하기 위해, 혼합 된 촉매의 간단한 모델 시스템이 도입되었다. 이 접근법으로부터, 백금 나노 입자의 결정성 및 전자 구조가 바뀌지 않았고 그로 인해 전기 화학적 환경에서 호산소 효과만을 관찰 할 수 있었다. 또한, 전기 화학적 측정에서 현저히 향상된 일산화탄소 산화를 관찰하였고, 실제 연료 전지 작동 조건에서도 혼합 된 촉매 시스템의 일산화탄소 산화가 촉진되었다는 것을 단위전지 실험을 통해 확인하였다.

3장에서는 앞서 밝힌 혼합 된 촉매 시스템의 타당성을 바탕으로, 다양한 온도에서의 열처리 방법을 이용하여 산성 전해질에서 다양한 산소 발생 활성을 갖는 루테늄 및 이리듐 산화물 (수화물) 촉매를 얻을 수 있었다. 수화된 산화물 촉매 사이의 물리 화학적 비교를 통해, 산성 전

해질에서의 산소발생 활성에 대한 새로운 기술어가 있다는 것을 확인하였다. 또한, 혼합 된 촉매 시스템을 산성 산소발생에서 상이한 활성을 갖는 산화물 및 수화물을 카본에 담지된 백금 촉매를 균일하게 블렌딩함으로써 제조하였다. 이 혼합 촉매의 일산화탄소 산화 반응을 토대로, 산화물 및 수화물 촉매의 산소발생 활성과 혼합 촉매의 일산화탄소 산화 성능 사이의 선형 상관관계를 산성 전해질에서 확인하였다. 이러한 관찰로부터 물 분자의 사슬에서 산소-수소와 또 다른 수소 결합 사이의 교환에 의한 장거리 물 활성화가 제안되었다.

4장에서는 염기성 전해질에서의 호산소 효과에 대한 연구를 수행 하였다. 일산화탄소 산화, 산소 발생 및 수소 발생에 대한 전기 화학적 관찰과 물리 화학적 특성 분석을 통해, 백금 나노 입자와 다양한 물 분해 촉매 사이에 전해질을 통한 장거리 호산소 상호 작용이 존재하는 것을 혼합 촉매 시스템에서 확인하였다. 또한, 금속-산소 상호 작용 정도가 호산소 효과에 미치는 영향에 대한 심층적인 논의가 수행되었다.

**주요어:** 전기 촉매 반응, 고분자 전해질 막 연료 전지, 물 전기 분해, 호산소 효과

**학번:** 2011-22925